AD-A167 419 FIELDS IN THE FOCAL REGION OF PARABOLOID AND OFFSET PARABOLOID REFLECTORS..(U) AEROSPACE CORP EL SEGUNDO CA ELECTRONICS RESEARCH LAB R H OTT ET AL. 31 MAR 86 1/1

UNCLASSIFIED TR-0086(6925-05)-4 SD-TR-86-16 F/G 9/5 NL

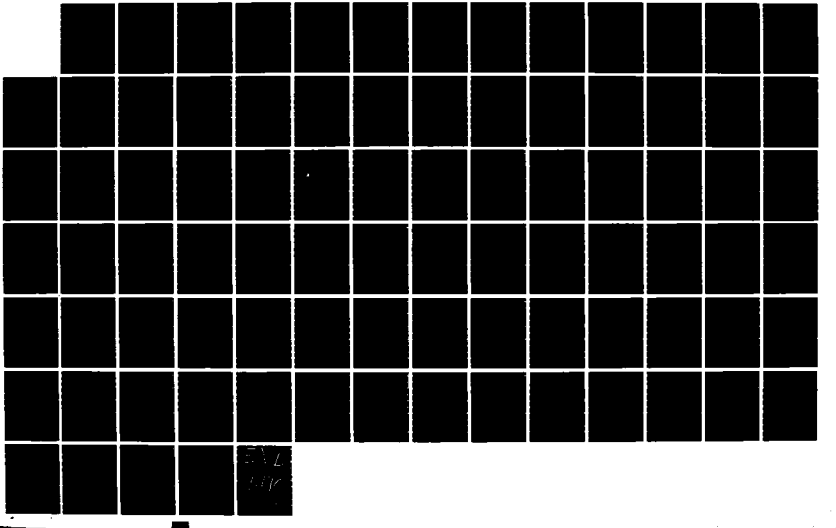

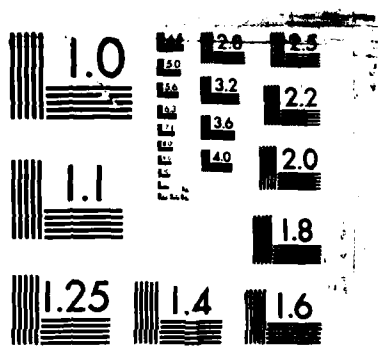

REPORT SD-TR-86-16

Fields in the Focal Region of Paraboloid and Offset Paraboloid Reflectors

R. H. OTT and R. B. DYBDAL
Electronics Research Laboratory
Laboratory Operations
The Aerospace Corporation
El Segundo, CA 90245

31 March 1986

Prepared for

SPACE DIVISION
AIR FORCE SYSTEMS COMMAND
Los Angeles Air Force Station
P.O. Box 92960, Worldway Postal Center
Los Angeles, CA 90009-2960

This report was submitted by The Aerospace Corporation, El Segundo, CA 90245, under Contract No. F04701-85-C-0086 with the Space Division, P.O. Box 92960, Worldway Postal Center, Los Angeles, CA 90009-2960. It was reviewed and approved for The Aerospace Corporation by M. J. Daugherty, Director, Electronics Research Laboratory.

Lt Wesley R. Dotts, SD/CGX was the project officer for the Mission-Oriented Investigation and Experimentation (MOIE) Program.

This report has been reviewed by the Public Affairs Office (PAS) and is releasable to the National Technical Information Service (NTIS). At NTIS, it will be available to the general public, including foreign nationals.

This technical report has been reviewed and is approved for publication. Publication of this report does not constitute Air Force approval of the report's findings or conclusions. It is published only for the exchange and stimulation of ideas.

Wesley R. Dotts

WESLEY R. DOTTS, Lt, USAF
MOIE Project Officer
SD/CGX

Joseph Hess

JOSEPH HESS, GM-15
Director, AFSTC West Coast Office
AFSTC/WCO OL-AB

UNCLASSIFIED

SECURITY CLASSIFICATION OF THIS PAGE (When Data Entered)

REPORT DOCUMENTATION PAGE		READ INSTRUCTIONS BEFORE COMPLETING FORM
1. REPORT NUMBER SD-TR-86-16	2. GOVT ACCESSION NO. AD-A167419	3. RECIPIENT'S CATALOG NUMBER
4. TITLE (and Subtitle) FIELDS IN THE FOCAL REGION OF PARABOLOID AND OFFSET PARABOLOID REFLECTORS		5. TYPE OF REPORT & PERIOD COVERED 6. PERFORMING ORG. REPORT NUMBER TR-0086(6925-05)-4
7. AUTHOR(s) R. H. Ott and R. B. Dybdal		8. CONTRACT OR GRANT NUMBER(s) F04701-85-C-0086
9. PERFORMING ORGANIZATION NAME AND ADDRESS The Aerospace Corporation El Segundo, Calif. 90245		10. PROGRAM ELEMENT, PROJECT, TASK AREA & WORK UNIT NUMBERS
11. CONTROLLING OFFICE NAME AND ADDRESS Space Division Los Angeles Air Force Station Los Angeles, Calif. 90009-2960		12. REPORT DATE 31 March 1986 13. NUMBER OF PAGES 84
14. MONITORING AGENCY NAME & ADDRESS(if different from Controlling Office)		15. SECURITY CLASS. (of this report) Unclassified 15a. DECLASSIFICATION/DOWNGRADING SCHEDULE

16. DISTRIBUTION STATEMENT (of this Report)

Approved for public release; distribution unlimited.

17. DISTRIBUTION STATEMENT (of the abstract entered in Block 20, if different from Report)

18. SUPPLEMENTARY NOTES

19. KEY WORDS (Continue on reverse side if necessary and identify by block number)

Physical Optics Currents, Contour Plots for Fields,
Numerical Integration Angle of Scan
Cassegrain Antenna
Offset Paraboloid Antenna,

20. ABSTRACT (Continue on reverse side if necessary and identify by block number)

While much development has been accomplished for reflector antenna technology, a need still exists in evaluating the impacts of design parameters. One such area lies with the design tradeoffs associated with the beam-scanning performance of reflector designs. A surface current integration analysis is derived which is exact to the order of physical optics. This analysis is applied to both circular and offset reflectors for on-axis and off-axis illumination for parameters which span the cases for which both substantial and minimal —

DD FORM 1473 (FACSIMILE)

UNCLASSIFIED

SECURITY CLASSIFICATION OF THIS PAGE (When Data Entered)

19. KEY WORDS *(Continued)*

20. ABSTRACT *(Continued)*

degradation with beam scan occur. The output of the analysis is cast in the form of contour plots defining the field structure in the focal region of the reflector. The results of the analyses compare favorably with data previously obtained for specialized parameters.

CONTENTS

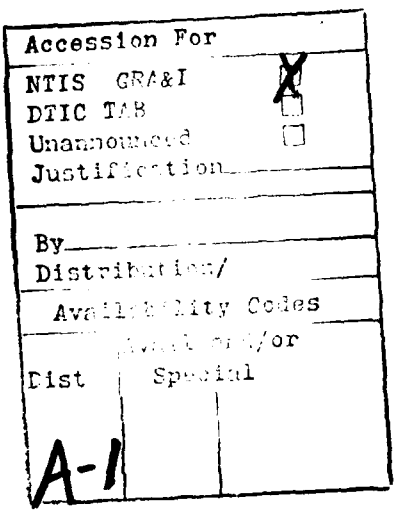

TABLES

FIGURES

FIGURES (Continued)

FIGURES (Continued)

FIGURES (Continued)

FIGURES (Continued)

I. INTRODUCTION

Paraboloidal and offset paraboloidal antennas employ lateral displacements of the feed to achieve beam-scanning capability. Some features of beam scanning are discussed in the literature (References 1 to 7). However, the simple but important problem of determination of the optimum feed location and orientation for a wide range of a/D ratios and several angles-of-scan still needs additional numerical work to examine the tradeoffs inherent in reflector design. Three angles-of-scan, 0°, 5°, and 10°, and a/D ratios of 0.2, 0.3, 0.4, 0.5, 0.6, 0.7, 0.8, 0.9, and 1.0 are considered. Contour plots are shown for the principal component of electric field in the focal regions of the paraboloidal and offset paraboloidal receiving antennas. Such contours illustrate the sensitivity to feed positioning and focusing for a wide range of reflector parameters.

The analysis of the focusing properties of parabolic reflectors is based on surface current integration. Reflector aperture fields are commonly analyzed by either of two methods, aperture integration or surface current integration. While both techniques are applicable for on-axis reflector characteristics, the surface current integration is appropriate for off-axis characteristics as well. The physical reason for this situation lies with the assumption inherent in transferring the fields from the reflector surface to the aperture plane in the aperture integration technique. The transfer implicitly assumes the rays from the reflector surface are parallel, an assumption that becomes increasingly invalid as the field moves off-axis. The consequence of this assumption is that the aperture integration underestimates the phase errors associated with the beam scanning and presents an optimistic picture of reflector performance.

This report develops the necessary analysis for the surface integration in a form that is exact to the order of physical optics; the authors are not aware of a previous derivation of this form. The numerical results are presented in terms of contours in the focal region, so that sensitivity to

defocusing can be illustrated. The numerical results are presented for a wide range of parameters, and the analysis can be applied to a general class of reflector designs.

II. ANALYSIS

The geometry for the paraboloidal reflector and unit vectors used in these analyses involves the spherical, paraboloidal and rectangular coordinate systems given in Figure 1. From Figure 1 and Reference 8, we have the elemental surface area on the paraboloid given by

$$ds = \frac{4\sqrt{2}\ a^2}{(1+\cos\theta)^{5/2}} \sin\theta d\theta d\phi \tag{1}$$

where a = focal length of the parabola. The angle α defines the a/D ratio of the parabola

$$\frac{a}{D} = \frac{1}{4} \cot \frac{\alpha}{2} . \tag{2}$$

The conversion from spherical coordinate unit vectors to rectangular coordinate unit vectors is given by

$$\begin{aligned} \underline{e}_x &= \underline{e}_r \sin\theta \cos\phi + \underline{e}_\theta \cos\theta \cos\phi - \underline{e}_\phi \sin\phi \\ \underline{e}_y &= \underline{e}_r \sin\theta \sin\phi + \underline{e}_\theta \cos\theta \sin\phi + \underline{e}_\phi \cos\phi \\ \underline{e}_z &= \underline{e}_r \cos\theta - \underline{e}_\theta \sin\theta \end{aligned} \tag{3}$$

with

$$\begin{aligned} x &= r\sin\theta\cos\phi \\ y &= r\sin\theta\sin\phi , \\ z &= r\cos\theta \end{aligned} \tag{4}$$

In paraboloidal coordinates, the unit vector $\underline{e}_y$ is

$$\underline{e}_y = \underline{e}_t \cos\frac{\theta}{2} \sin\phi + \underline{e}_n \sin\frac{\theta}{2} \sin\phi - \underline{e}_b \cos\phi \tag{5}$$

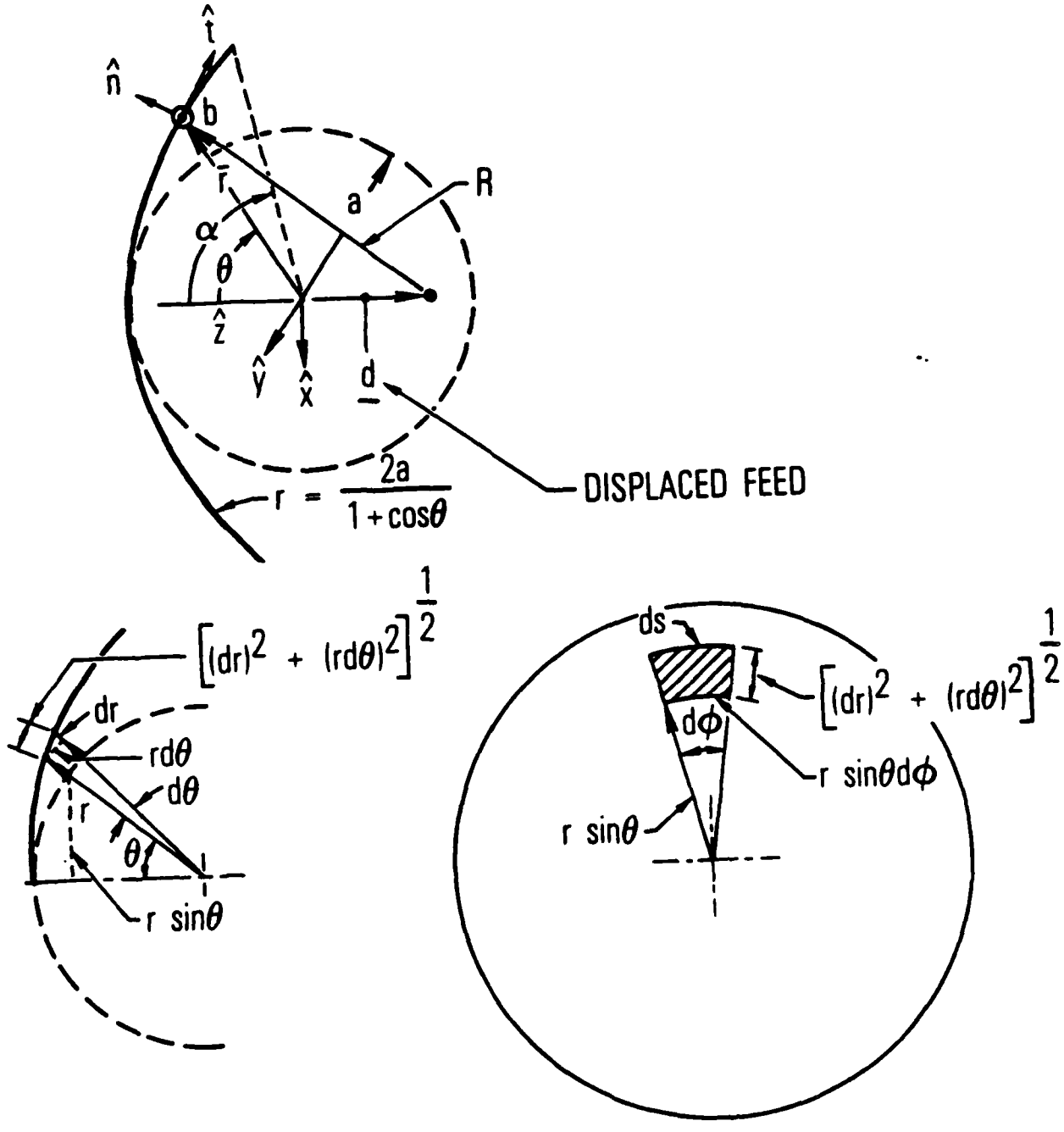

Figure 1. Geometry for a Paraboloidal Reflector

Consider the incident wave from the right along the direction ϕ_o with respect to the z-axis, as shown in Figure 2. Then

$$\underline{E}^i = \underline{e}_x Z_o e^{-ik(z\cos\phi_o + x\sin\phi_o)} (e^{i\omega t})$$

$$\underline{H}^i = \underline{e}_y e^{-ik(z\cos\phi_o + x\sin\phi_o)} (e^{i\omega t}) \tag{6}$$

The equation of the paraboloid is

$$r = \frac{2a}{1+\cos\theta} \tag{7}$$

From Equations (4), (5), (6) and (7) the incident magnetic field in the paraboloidal coordinate system is

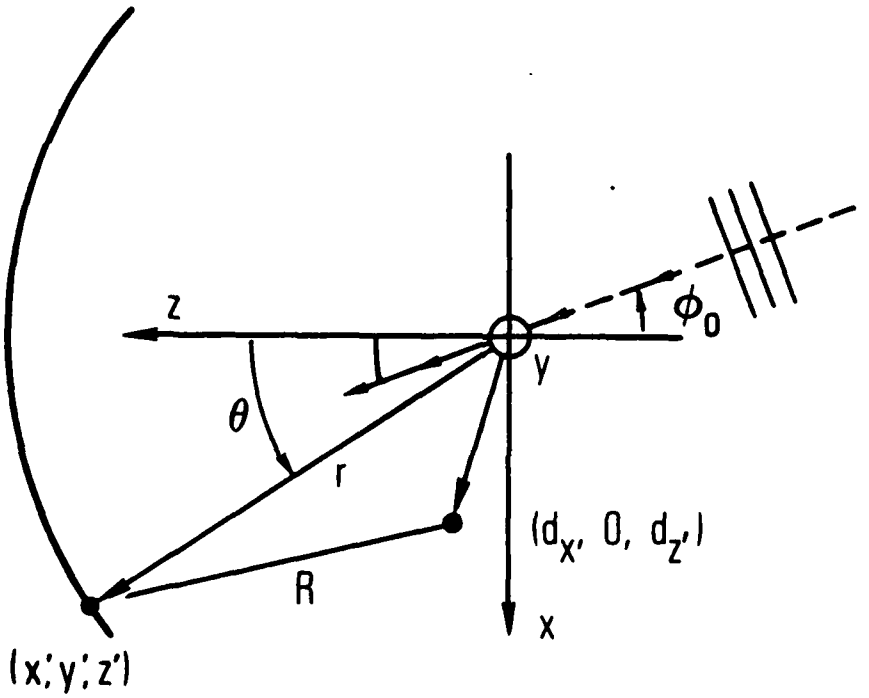

Figure 2. Geometry of Parabola, Incident Wave, Integration Point (x', y', z'), and Observation Point (d_x, o, d_z)

$$\underline{H}^i = e^{-i2ka(\cos\theta\cos\phi_o+\sin\theta\cos\phi\sin\phi_o)/(1+\cos\theta)}$$

$$[\underline{e}_t\cos\tfrac{\theta}{2}\sin\phi \qquad (8)$$

$$+ \underline{e}_n\sin\ \tfrac{\theta}{2}\sin\phi - \underline{e}_b\cos\phi]$$

The physical optics current induced on the parabola is

$$\underline{I}_{p.o.} = 2(\underline{e}_n x \underline{H}^i) \qquad (9)$$

and substituting Equation (8) into (9) gives

$$\underline{I}_{p.o.} = \exp\{-ika(\cos\theta\cos\phi_o+\sin\theta\cos\phi\sin\phi_o)/(1+\cos\theta)\}[-\underline{e}_b\cos\tfrac{\theta}{2}\sin\phi-\underline{e}_t\cos\phi] \qquad (10)$$

The magnetic field scattered by a perfectly conducting surface is

$$\underline{H}^S = \int_S \frac{\partial G}{\partial R}(\underline{e}_R \times \underline{I}_{p.o.})ds' \qquad (11)$$

where the free space Green's function is

$$G(R) = \frac{e^{-ikR}}{4\pi R} \qquad (12)$$

and the distance between the integration point ($\underline{r}'$ in Figure 2) and the observation point [$\underline{r}$ or (d_x',o,d_z') in Figure 2] is

$$R = |\underline{r}' - \underline{r}| \qquad (13)$$

From Equation (12),

$$\frac{\partial G}{\partial R} = ikG(1 + \frac{1}{ikR}) \qquad (14)$$

The distance, R, in Figure 2 between the integration point (x',y',z') and the observation point near the focus (d_x,o,d_z) is

$$R = \sqrt{(x'-d_x)^2 + y'^2 + (z'-d_z)^2} \tag{15}$$

Substituting for x', y', and z' from Equation (4) and for r from Equation (7) into Equation (15),

$$(R/a)^2 = \left[\frac{2\sin\cos\phi}{1+\cos\theta} - \frac{d_x}{a}\right]^2 + \left[\frac{2\sin\theta\sin\phi}{1+\cos\theta}\right]^2 + \left[\frac{2\cos\theta}{1+\cos\theta} - \frac{d_z}{a}\right]^2 \tag{16}$$

The scattered electric field can be calculated using the Maxwell curl equation

$$E = \frac{1}{i\omega\epsilon}\left(\underline{\nabla} \times \underline{H}\right) \tag{17}$$

with the curl operator operating on the unprimed coordinates. From Equations (11) and (17)

$$\underline{E}^S = \frac{1}{i\omega\epsilon} \int_S \underline{\nabla} \times \left\{\frac{\partial G}{\partial R}\left(\underline{e}_R \times \underline{I}_{p.o.}\right)\right\} ds \tag{18}$$

Define the vector $\underline{A}$ as

$$\underline{A} = \underline{e}_R \times \underline{I}_{p.o.} \tag{19}$$

Then

$$\underline{\nabla} \times \left(\frac{\partial G}{\partial R}\underline{A}\right) = \frac{\partial G}{\partial R}\left(\underline{\nabla}\times\underline{A}\right) + \underline{\nabla}\left(\frac{\partial G}{\partial R}\right) \times \underline{A} \tag{20}$$

We have

$$\underline{\nabla}\left(\frac{\partial G}{\partial R}\right) = \underline{e}_R \frac{\partial^2 G}{\partial R^2} \tag{21}$$

$$= \underline{e}_R(-ikG)\left(-ik - \frac{2}{R} + \frac{2i}{kR^2}\right) \tag{22}$$

From Equation (19)

$$\underline{\nabla} \times \underline{A} = \underline{\nabla} \times [\underline{e}_R \times \underline{I}_{p.o.}]$$

$$= (\underline{I}_{p.o.} \cdot \underline{\nabla})\underline{e}_R - \underline{I}_{p.o.} (\underline{\nabla} \cdot \underline{e}_R) - (\underline{e}_R \cdot \underline{\nabla})\underline{I}_{p.o.} + \underline{e}_R (\underline{\nabla} \cdot \underline{I}_{p.o.}) \quad (23)$$

but the last two terms on the right-hand-side of Equation (23) are zero because the $\underline{\nabla}$ operator is operating on the unprimed coordinates and $\underline{I}_{p.o.}$ is a function of the primed coordinates $\underline{r}'$; i.e., $\underline{I}_{p.o.}(\underline{r}')$. Also,

$$\underline{\nabla} \cdot \underline{e}_R = \frac{2}{R} \quad (24)$$

Also, we have

$$(\underline{I}_{p.o.} \cdot \underline{\nabla})\underline{e}_R = I_r \frac{\partial \underline{e}_R}{\partial R} + \frac{I_\theta}{r} \frac{\partial \underline{e}_R}{\partial \theta} + \frac{I_\phi}{r \sin\theta} \frac{\partial \underline{e}_R}{\partial \phi}$$

$$= \frac{1}{R} (\underline{e}_\theta I_\theta + \underline{e}_\phi I_\phi)$$

$$= \frac{1}{R} [\underline{I}_{p.o.} - \underline{e}_R (\underline{e}_R \cdot \underline{I}_{p.o.})] \quad (25)$$

Substituting Equations (24) and (25) into (23) gives

$$\underline{\nabla} \times [\underline{e}_R \times \underline{I}_{p.o.}] = - \frac{1}{R} [\underline{I}_{p.o.} + \underline{e}_R (\underline{e}_R \cdot \underline{I}_{p.o.})] \quad (26)$$

From Equations (26), (22), and (20) we obtain

$$\nabla \times \{\frac{\partial G}{\partial R} (\underline{e}_R \times \underline{I}_{p.o.})\} = - ikG\left(1 + \frac{1}{ikR}\right)\left(\frac{-1}{R}\right)[\underline{I}_{p.o.} + \underline{e}_R (\underline{e}_R \cdot \underline{I}_{p.o.})]$$

$$- ikG \left(-ik - \frac{2}{R} + \frac{2i}{kR^2}\right) \underline{e}_R \times (\underline{e}_R \times \underline{I}_{p.o.})$$

$$= ikG\left(\frac{1}{R} + \frac{1}{ikR^2}\right)\left[\underline{I}_{p.o.} + \underline{e}_R(\underline{e}_R \cdot \underline{I}_{p.o.})\right]$$

$$-ikG\left(-ik - \frac{2}{R} + \frac{2i}{kR^2}\right)\left[-\underline{I}_{p.o.} + \underline{e}_R(\underline{e}_R \cdot \underline{I}_{p.o.})\right]$$

$$= ikG\underline{I}_{p.o.}\left\{\frac{1}{R} + \frac{1}{ikR^2} - ik - \frac{2}{R} + \frac{2i}{kR^2}\right\} \qquad (27)$$

$$+ ikG\,\underline{e}_R(\underline{e}_R \cdot \underline{I}_{p.o.})\left\{\frac{1}{R} + \frac{1}{ikR^2} + ik + \frac{2}{R} - \frac{2i}{kR^2}\right\}$$

$$= ikG\left\{\underline{I}_{p.o.}\left(-ik - \frac{1}{R} + \frac{i}{kR^2}\right)\right.$$

$$\left. + \underline{e}_R(\underline{e}_R \cdot \underline{I}_{p.o.})\left(ik + \frac{3}{R} + \frac{3}{ikR^2}\right)\right\}$$

$$= k^2G\left\{\underline{I}_{p.o.}\left(1 - \frac{i}{kR} - \frac{1}{(kR)^2}\right)\right.$$

$$\left. + \underline{e}_R(\underline{e}_R \cdot \underline{I}_{p.o.})\left(-1 + \frac{3i}{kR} + \frac{3}{(kR)^2}\right)\right\}$$

Substituting Equation (27) into (18) gives for the tangential component at the scattered electric field

$$\underline{E}_t^s = ikZ_o \int_S \underline{I}_{p.o.}\left(1 - \frac{1}{kR} - \frac{1}{(kR)^2}\right)\frac{e^{-ikR}}{4\pi R}\,ds \qquad (28)$$

Substituting Equation (1) for ds into (28) gives

$$\underline{E}_t^s = \frac{-ikZ_o 4\sqrt{2}a}{4\pi}\int_o^{2\pi} d\phi' \int_o^{\alpha} d\theta' \frac{\sin\theta}{(1+\cos\theta)^{5/2}}\,\underline{I}_{p.o.} \cdot$$

$$e^{-i2ka\cos\theta/(1+\cos\theta)}\,\frac{e^{-ikR}}{(R/a)}\left(1 - \frac{i}{kR} - \frac{1}{(kR)^2}\right) \qquad (29)$$

and substituting for $\underline{I}_{p.o.}$ from Equation (9) into (29) gives

$$\underline{E}_t^s = -i240\sqrt{2}\,(ka)\int_o^{2\pi} d\phi' \int_o^{\alpha} d\theta' \frac{\sin\theta(\underline{e}_n \times \underline{H}^i)}{(1+\cos\theta)^{5/2}} \cdot$$

$$\cdot \exp\left\{-ik\left[R + \frac{2a\cos\theta}{1+\cos\theta}\right]\right\}\frac{1}{(R/a)}\left(1 - \frac{i}{kR} - \frac{1}{(kR)^2}\right) \qquad (30)$$

From Equation (10) and Figure 1 (giving the unit vectors on the paraboloid in terms of $\underline{e}_R$, $\underline{e}_\theta$ and $\underline{e}_\phi$)

$$- \underline{e}_b \cos\frac{\theta}{2}\sin\phi - \underline{e}_t \cos\phi = \underline{e}_\phi \cos\frac{\theta}{2}\sin\phi - \left(\underline{e}_R \sin\frac{\theta}{2} + \underline{e}_\theta \cos\frac{\theta}{2}\right)\cos\phi$$

$$= - \underline{e}_R \sin\frac{\theta}{2}\cos\phi - \underline{e}_\theta \cos\frac{\theta}{2}\cos\phi + \underline{e}_\phi \cos\frac{\theta}{2}\sin\phi \qquad (31)$$

The dominant component in Equation (30) is E_θ^s, and in general, the radial component E_r^s will not respond to a practical feed. The component E_ϕ^s represents the cross-polarization.

This analysis has developed the general field expressions for a reflector, which will now be applied to the center-fed circular reflector and an offset-fed reflector. For the center-fed reflector, the principally polarized component is:

$$E_\theta^S(d_z,0,d_z) = i240\sqrt{2}\ ka\ \cos\frac{\theta}{2}\cos\phi \int_0^{2\pi} d\phi' \int_0^{\alpha} d\theta' \frac{\sin\theta'}{(1+\cos\theta')^{5/2}} \frac{1}{(R/a)} \cdot$$

$$\cdot \exp\left\{-ikR\left[1 + \frac{2(a/R)}{1+\cos\theta'}(\cos\theta'\cos\phi_o + \sin\theta'\cos\phi'\sin\phi_o)\right]\right\} \cdot$$

$$\cdot \left(1 - \frac{i}{kR} - \frac{1}{(kR)^2}\right), \qquad (32)$$

with R given in Equation (16).

The geometry and coordinate frames for the offset paraboloidal reflector antenna are shown in Figure 3. Given the angle θ_o between the reflector axis and the feed axis, the half-angle subtended by the reflector at the focus, θ_c, is found from

$$\frac{a}{D/2} = \frac{1}{4}\frac{(\cos\theta_o + \cos\theta_c)}{\sin\theta_c} \qquad (33)$$

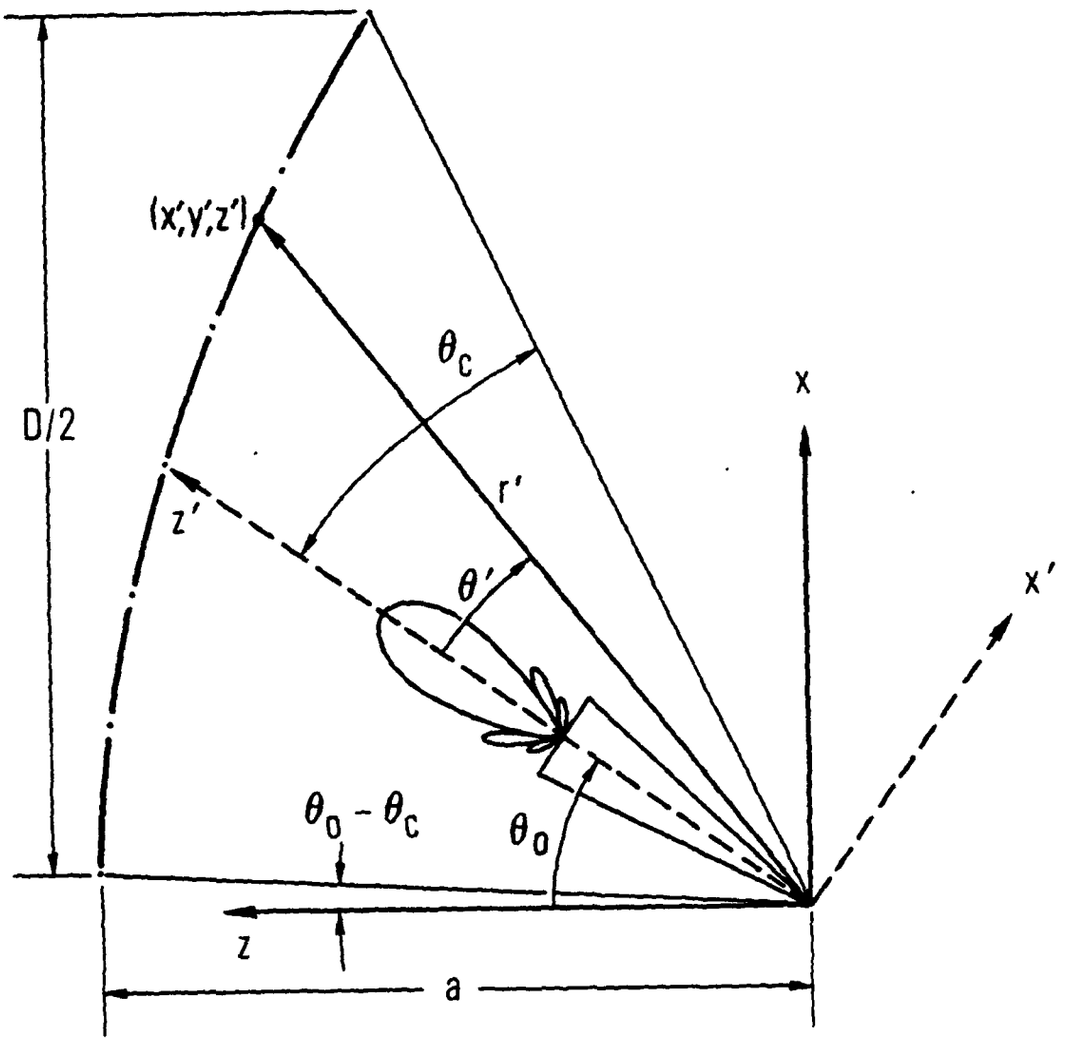

Figure 3. Geometry for Offset Paraboloidal Reflector and Feed

The transformation from the xyz coordinate frame in Figure 3 to the x'y'z' coordinate frame is determined from the condition

$$\underline{e}_r = \underline{e}_{r'} \tag{34}$$

with

$$\underline{e}_{r'} = \underline{e}_{x'}\sin\theta'\cos\phi' + \underline{e}_{y'}\sin\theta'\sin\phi' + \underline{e}_{z'}\cos\theta' \tag{35}$$

and

$$\underline{e}_r = \underline{e}_x\sin\theta\cos\phi + \underline{e}_y\sin\theta\sin\phi + \underline{e}_z\cos\theta \tag{36}$$

Now the rotation of frame xyz to x'y'z' is defined by

$$\begin{aligned} \underline{e}_{x'} &= \underline{e}_x \cos\theta_o - \underline{e}_z\sin\theta_o \\ \underline{e}_{y'} &= \underline{e}_y \\ \underline{e}_{z'} &= \underline{e}_x\sin\theta_o + \underline{e}_z \cos\theta_o \end{aligned} \tag{37}$$

Substituting Equation (37) into (35) and then substituting (35) and (36) into (34) gives

$$\begin{aligned} \sin\theta\cos\phi &= \cos\theta_o \sin\theta'\cos\phi' + \sin\theta_o\cos\theta' \\ \sin\theta\sin\phi &= \sin\theta'\sin\phi' \\ \cos\theta &= \cos\theta_o\cos\theta' - \sin\theta_o\sin\theta'\cos\phi' \end{aligned} \tag{38}$$

and substituting the last of Equation (38) into Equation (7) gives the equation defining the surface of the offset paraboloid

$$r = \frac{2a}{1+\cos\theta_o\cos\theta' - \sin\theta_o\sin\theta'\cos\phi'} \tag{39}$$

For an incident plane wave along the direction $(\theta_o - \phi_o)$ with respect to the positive z'-axis, as shown in Figure 4, gives for the principal component of scattered electric field

$$E_\theta^s (d_{x'},o,d_{z'}) = i240\sqrt{2}\,(ka)\cos\frac{\theta}{2}\cos\phi \int_o^{2\pi} d\phi' \int_o^{\theta_c} d\theta' \frac{\sin\theta'}{(1+\cos\theta')^{5/2}} \frac{e^{-ikR}}{(R/a)} \cdot$$

$$\cdot \left(1 - \frac{i}{kR} - \frac{1}{(kR)^2}\right) e^{-ik\left(z'\cos(\theta_o-\phi_o) - x'\sin(\theta_o-\phi_o)\right)} \qquad (40)$$

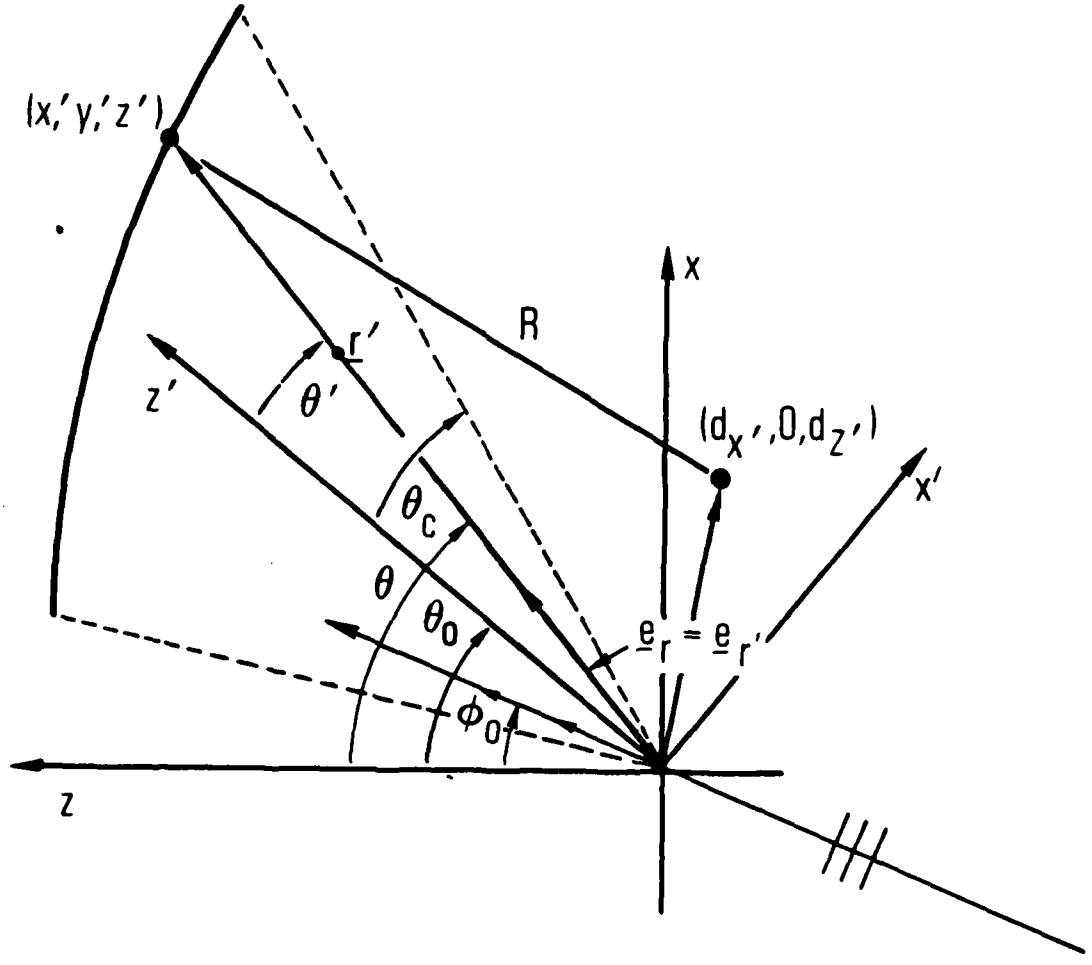

Figure 4. Incident Wave Making an Angle of θ_o with Respect to the z-Axis

III. NUMERICAL RESULTS

Numerical results based on the preceding analysis are now presented in the form of contour plots. Some common features of the contour plots are:

1) The contour values represent

$$10 \log_{10} |E_\theta|^2 ,$$

where E_θ is in volts/m assuming 1 amp/m incident magnetic field.

2) The range or maximum size of the window is 0.14 for d_z/a and 0.056 for d_x/a. The origin for d_z/a and d_x/a is adjusted to show the shift in the contours for angles of incidence other than boresight. For example, if the incident field is 5° to the right of the positive x-axis, the set of contours are shifted along the positive x-axis by tan 5°.

3) The location of the maximum along the z-direction, or the reflector axis z remains relatively far from the Petzval surface of classical optics. The maximum field values are indicated and constant amplitude contours in 3 dB increments are given in each figure.

4) All contours were computed with the assumption that the feed pattern is that of a short dipole, i.e., cos θ amplitude variation in the E-plane and uniform amplitude variation in the H-plane. This choice was made to allow comparison with previously published results.

The two-dimensional integrations in Equations (32) and (40) were evaluated using a two-dimensional trapezoidal rule with about 2 points per wavelength. This number of integration points yielded about 6 significant figure accuracy.

The numerical results were computed in the following way. The focal distance was fixed, namely, ka = 100 and the a/D ratio was varied from 0.2 to 1.0. The corresponding aperture diameters varied from $250/\pi$ to $50/\pi$ wavelengths. This variation in parameters spans conditions for which substantial loss in performance with beam scan exists, a/D = 0.2, to cases in which almost

no scan loss is present, a/D = 1. If the antenna efficiency is assumed to remain constant at 55% as well as a constant beamwidth factor of 70, the on-axis gain and beamwidth values would range between 45.4 and 31.4 dB. In all cases, the feed pattern remained constant, and the illumination efficiency varies with changes in a/D. This choice of parameters illustrates the range of situations which arise in diverse applications. Table I summarizes the cases presented in the subsequent figures.

In Figs. 5 to 13,* contour plots of the θ-component for the scattered electric field in Equation (32) for the case of the paraboloidal reflector are shown versus normalized displacement d_x/a and d_z/a from the focus. As a check on the derivations and numerical analysis, comparisons were made with the results of Rusch and Ludwig [7] for the case ka = 92.5, a/D = 0.433 and ϕ_o = 0°, 8° and 16°. The results compared as well as one can read contour plots approximately 2" × 2" in a journal publication.

In Figures 14 to 22, the angle of incidence, ϕ_o, is 5° from the axis of the paraboloid. When the angle of incidence arrives from a direction to the right of the focus, the amplitude contours shift to the left of the focus, as shown. The amount of shift for 5° incidence is about

$$\text{max. on x-axis} = (a/\lambda) \tan 5° \tilde{=} 1.392\ \lambda \qquad (41)$$

The ratio of the result in Equation (41) and the actual maximum is referred to as the beam derivation factor (Lo, [9]). Table II compares the computed beam deviation factor with the measured beam deviation factors tabulated by Lo. The agreement with measured results is good; for smaller values of a/D, the computed beam deviation factor is smaller than Lo's results because less amplitude taper is used in the analysis than in the measurements.

The maximum intensity points for 5° incidence are about 2.2 dB below the original maximum intensity for axial incidence corresponding to scan loss.

*Figure 5 through 59 are presented at the end of this section.

Table I. Data Tabulation

Circular Reflector	Figure Numbers
On-Axis	5-13
5° Scan	14-22
10° Scan	23-31
Offset Reflector	
On-Axis	32-40
5° Scan	41-49
10° Scan	50-58

Table II. Comparison of Calculated and Measured Beam Deviation Factors (ϕ_o = 5°)

$\frac{a}{D}$	Computed Beam Deviation Factor	Measured Beam Deviation Factor*
0.3	0.744	0.8
0.4	0.825	0.85
0.5	0.875	0.89
0.6	0.892	0.91
0.7	0.930	0.93
0.8	0.960	0.95

* Lo, 1960

Reciprocity permits the contours in Figures 14 to 22 to be interpreted in terms of an infinitesimal dipole feed 5° to the right of the focus yielding the magnitude of the field observed at a distant point. Also, we note in Figures 17 to 22 that the maximum field is displaced toward the reflector from about $z = 0.08\ \lambda$ for $a/D = 0.5$ to about $z = 1\ \lambda$ for $a/D = 1.0$. This can be interpreted as phase loss being overcome by a decrease in spillover and becomes less pronounced for the deeper reflectors (i.e., $a/D < 0.4$). Similar results are observed in Reference 7.

In Figures 23 to 31, the angle of incidence, ϕ_o, is 10° from the axis of the paraboloid. In this case, the geometrical optics maximum occurs at

$$\text{max. on x-axis } (\lambda) = (a/\lambda) \tan 10° \cong 2.806\ \lambda \tag{42}$$

The beam deviation factors for this angle of incidence are similar to those given in Table II.

The contours also provide the opportunity to compare lateral defocusing characteristics based on other analyses. The original work done by Ruze (Reference 3) was based on aperture integration techniques, which are limited to small scan angles for the reasons discussed in the Introduction. In his analysis, Ruze defined a parameter

$$X = \frac{N_B}{(a/D)^2 + 0.02} \tag{43}$$

where N_B is the number of beamwidths scanned from the parabolic axis. Ruze went on to determine the scan loss in terms of the parameter X, as indicated in Figure 6 of Reference 3. While the scan loss depends on amplitude taper, the losses out to about 5 dB can be computed from

$$L, (dB) = 0.002\ X^2 \tag{44}$$

for a typical parabola. Comparison of the scan loss for this equation and the contour values at their peak levels yields the results in Table III.

Table III. Scan Loss Comparison

a/D	5° Scan Contours	5° Scan Ruze	10° Scan Contours	10° Scan Ruze
0.4	0.8	0.5	2.9	2.0
0.4*	0.8	0.6*	2.9	2.2*
0.5	0.8	0.14	1.6	0.6
0.6	0.1	0.05	0.5	0.2
0.7	0.1	0	0.2	0.08
0.8	0	0	0.1	0
0.9	0	0	0	0
1.0	0	0	0.1	0

*From Reference 6

The additional entries in Table III are from subsequent work by Imbriale, Ingerson, and Wong (Reference 6). Their analysis is also based on a surface current formulation, and their results are expressed in terms of differences relative to those by Ruze. In their formulation, however, the phase in the integrand has been approximated. Their values are shown by the asterisk in Table III. Their results are also presented for $a/D = 0.4$.

A final check on the analysis was made by examining the axial defocusing characteristics. A previous treatment of this problem has been made by Ingerson and Rusch (Reference 1). Again, a parabola with an $a/D = 0.4$ was used, and values for feed illumination with a $\cos^n(\theta)$ variation were computed. This analysis also approximates the phase in the integrand. A comparison of their results and those obtained in this analysis is presented in Figure 59 (from Reference 6). The deviations for increased defocusing are attributed to the phase approximation.

In Figures 32 to 40, the fields in the focal region of an offset paraboloid are shown for the case of axial incidence, and $\phi_o = 0°$. For a given a/D ratio and θ_o, θ_c is calculated from Equation (33). The criterion for selecting θ_o was to provide approximately 1 wavelength clearance for the feed at the lower edge of the offset paraboloid defined by the angle $\theta_o - \theta_c$ in Figure 3. Since $ka = 100$, $a/\lambda \cong 15.915$ and $\theta_o - \theta_c$ was selected so that

$$a(\theta_o - \theta_c) = 15.915\ \lambda \quad (\theta_o - \theta_c) > \lambda \tag{45}$$

with $\theta_o - \theta_c$ in radians. Equation (45) implies $\theta_o - \theta_c$ larger than 3 to 4 degrees. It should be noted that θ_o was selected as small as possible to satisfy Equation (45) since the cross polarization increases with θ_o (Reference 10). For example, in Figure 32 we see for $a/D = 0.2$, and $\theta_o = 53°$ that from Equation (33), $\theta_c = 50.507$ and $a(\theta_o - \theta_c) = 0.67\ \lambda$. The most significant difference in the fields in the focal region of a conventional paraboloid from those in the focal region of an offset paraboloid is that the 3 dB contour extends out a greater distance from the focus for the offset paraboloid than the conventional paraboloid. That is, if we compare Figures 5 and 23, the 3-dB contour along the z-axis in Figure 5 occurs at $d_z/a \cong .04$, while in Figure 23 the 3-dB contour intersects the z-axis at

$d_z/a = 0.8$. Also, the 3-dB contour intersects the x-axis in Figure 5 at about $d_x/a \cong 0.014$, while in Figure 23 the 3-dB axis intersects the x-axis at $d_x/a \cong 0.021$.

The most significant feature of the contour plots for the case of the offset paraboloid is the broad maxima, especially for the larger a/D ratios, as shown for example in Figures 36-40, 44-49 and 52-58. This situation results in the lack of sensitivity to feed placement for offset designs.

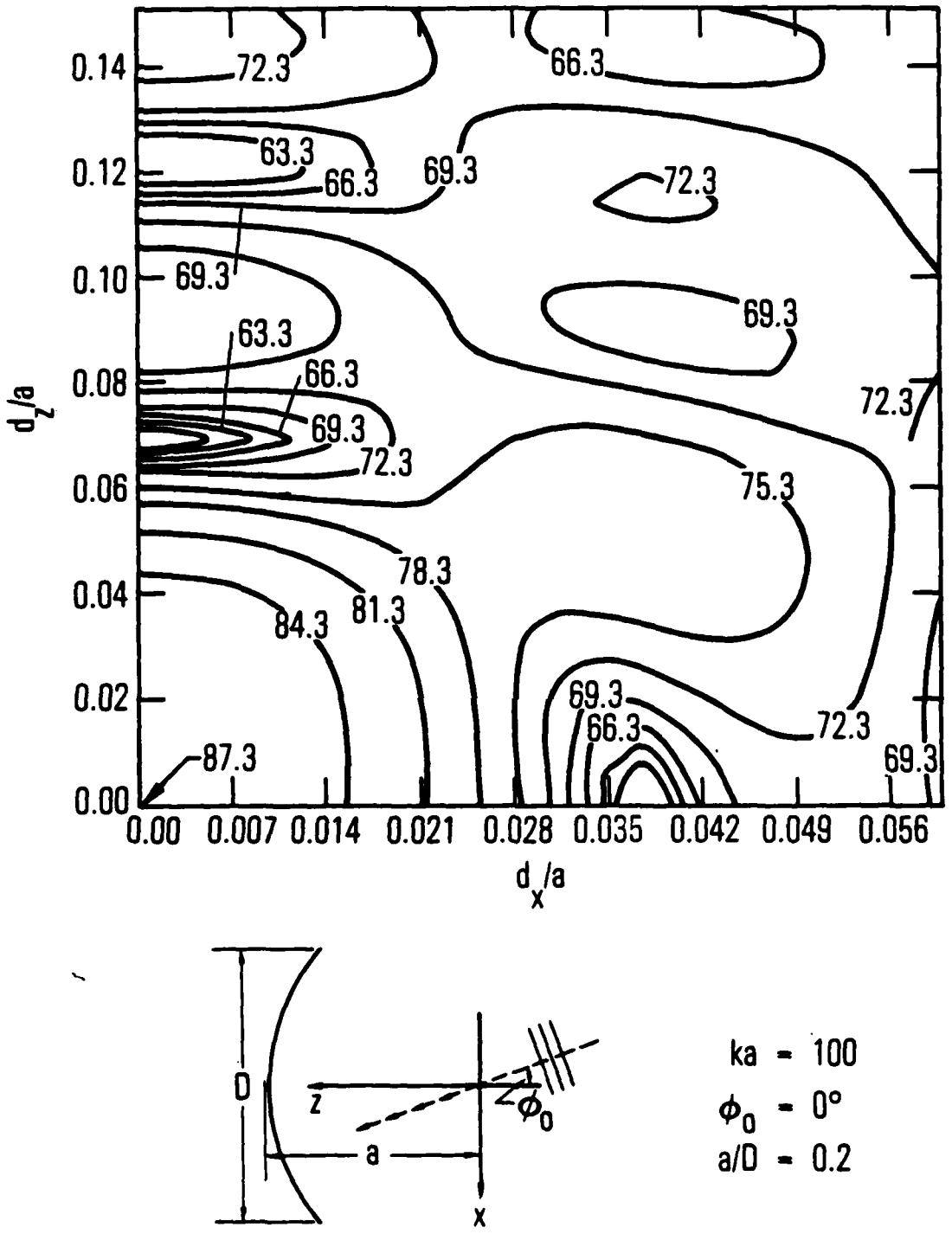

Figure 5. Contour Plot of Total Field in Focal Region of Paraboloid ka = 100, ϕ_o = 0°, a/D = 0.2

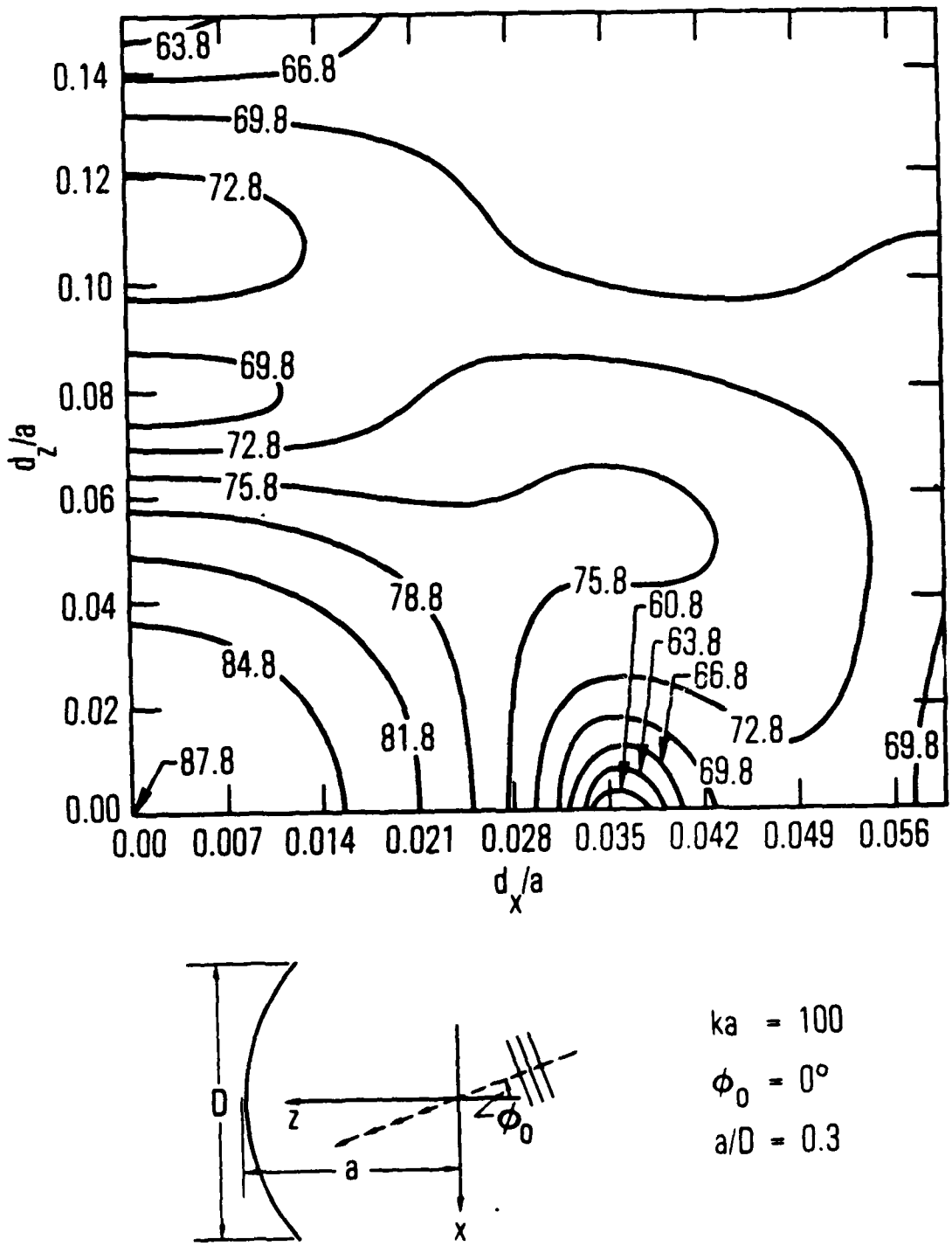

Figure 6. Contour Plot of Total Field in Focal Region of Paraboloid ka = 100, ϕ_o = 0°, a/D = 0.3

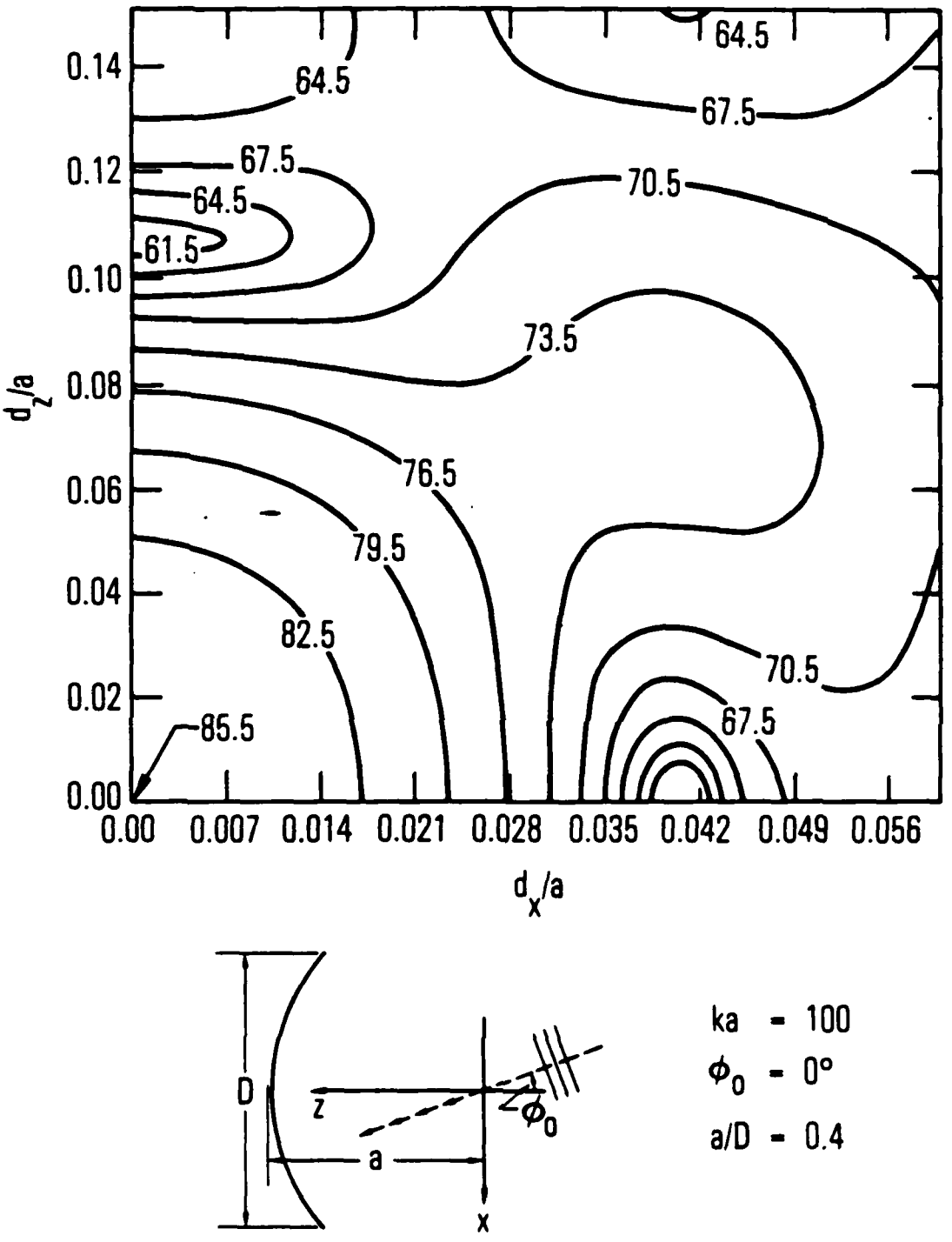

Figure 7. Contour Plot of Total Field in Focal Region of Paraboloid ka = 100, ϕ_o = 0°, a/D = 0.4

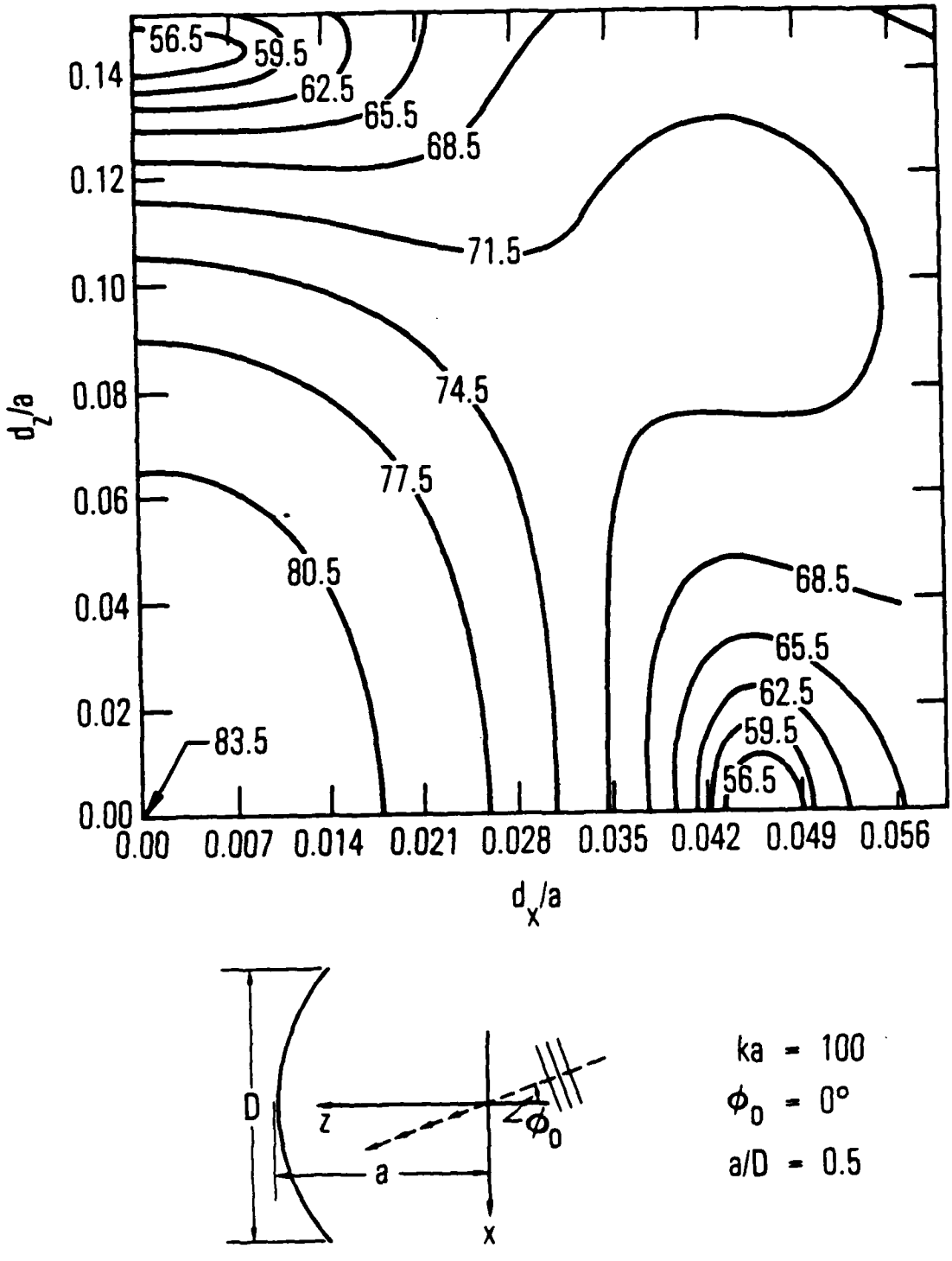

Figure 8. Contour Plot of Total Field in Focal Region of Paraboloid ka = 100, ϕ_o = 0°, a/D = 0.5

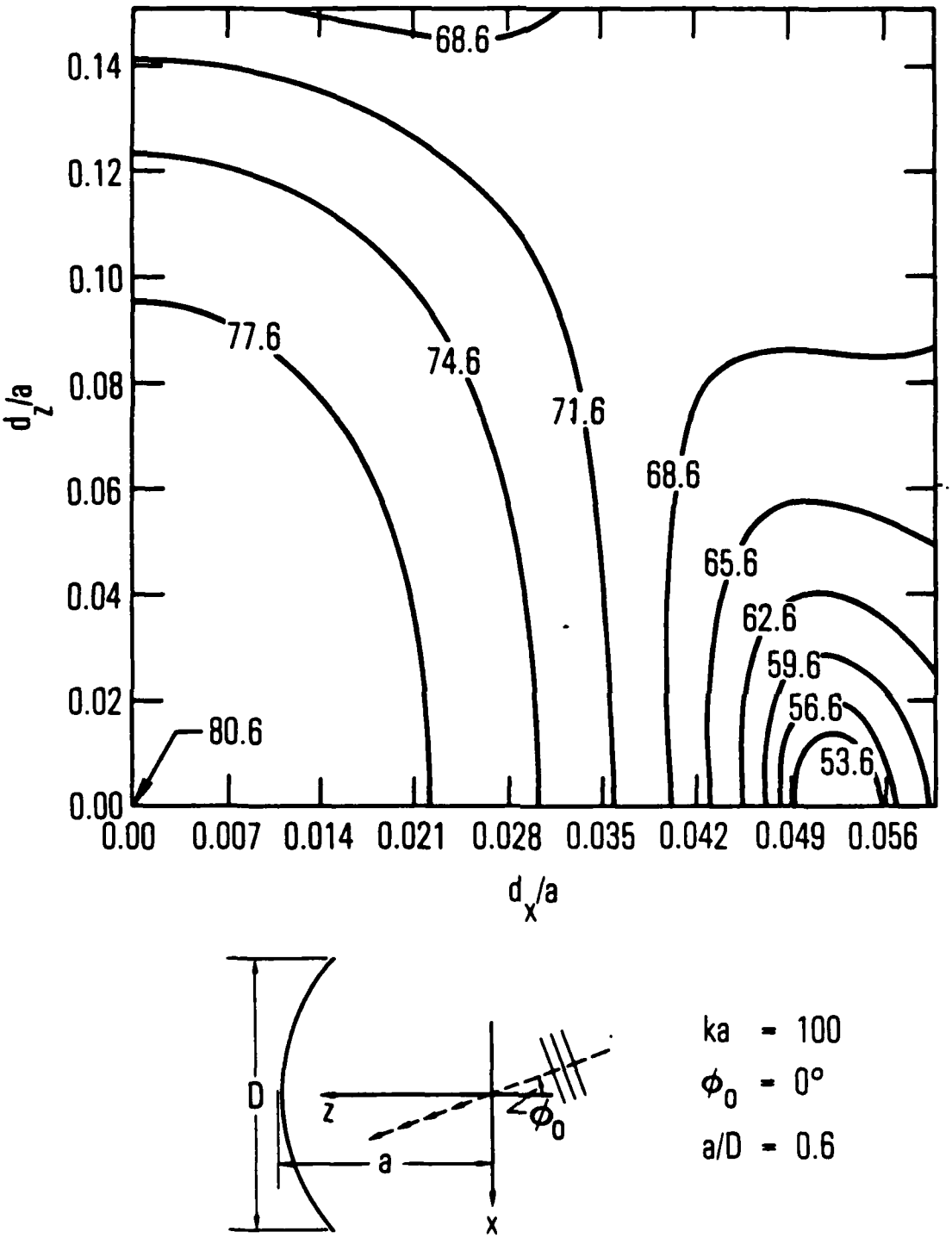

Figure 9. Contour Plot of Total Field in Focal Region of Paraboloid ka = 100, ϕ_0 = 0°, a/D = 0.6

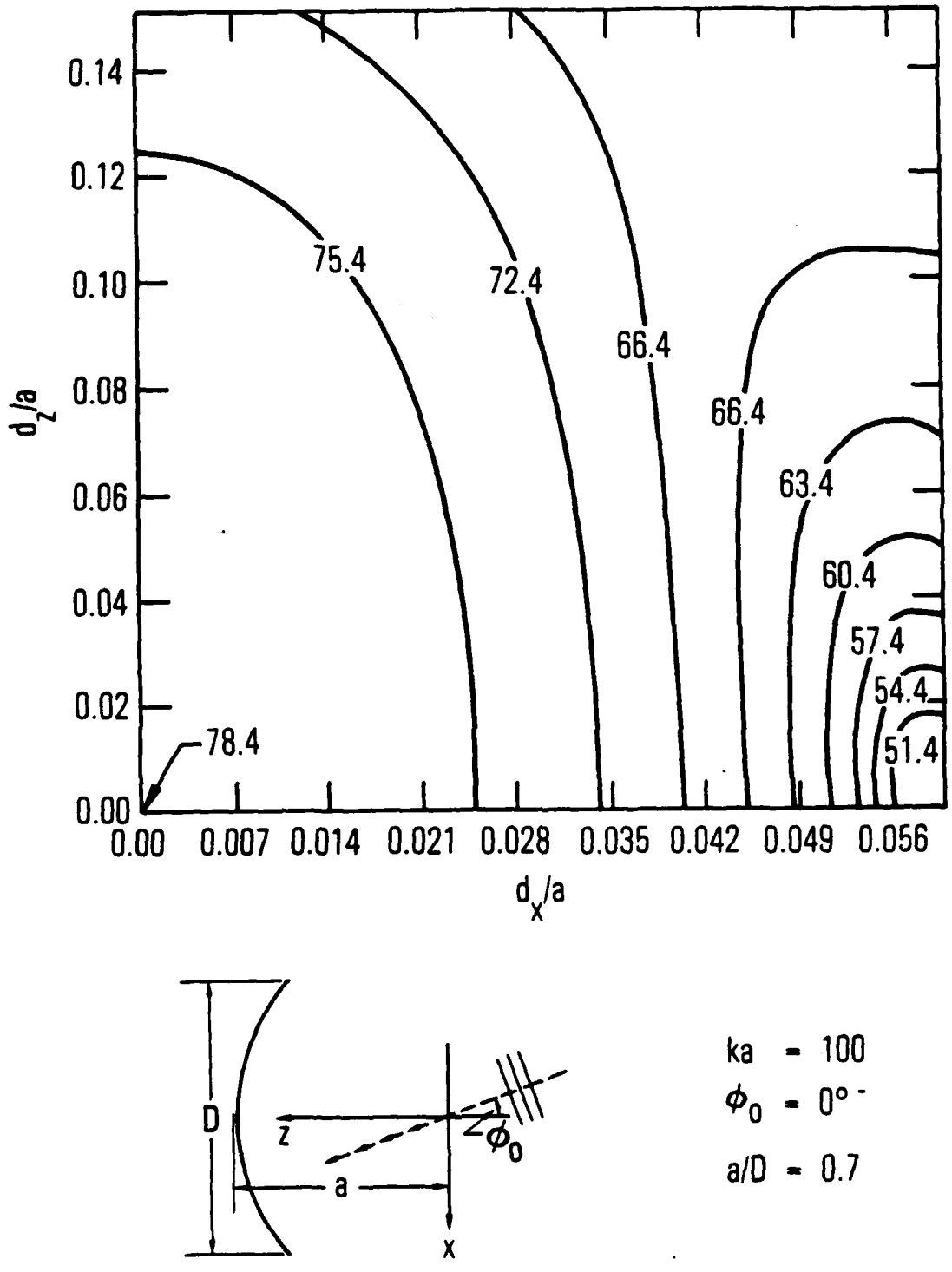

Figure 10. Contour Plot of Total Field in Focal Region of Paraboloid ka = 100, ϕ_o = 0°, a/D = 0.7

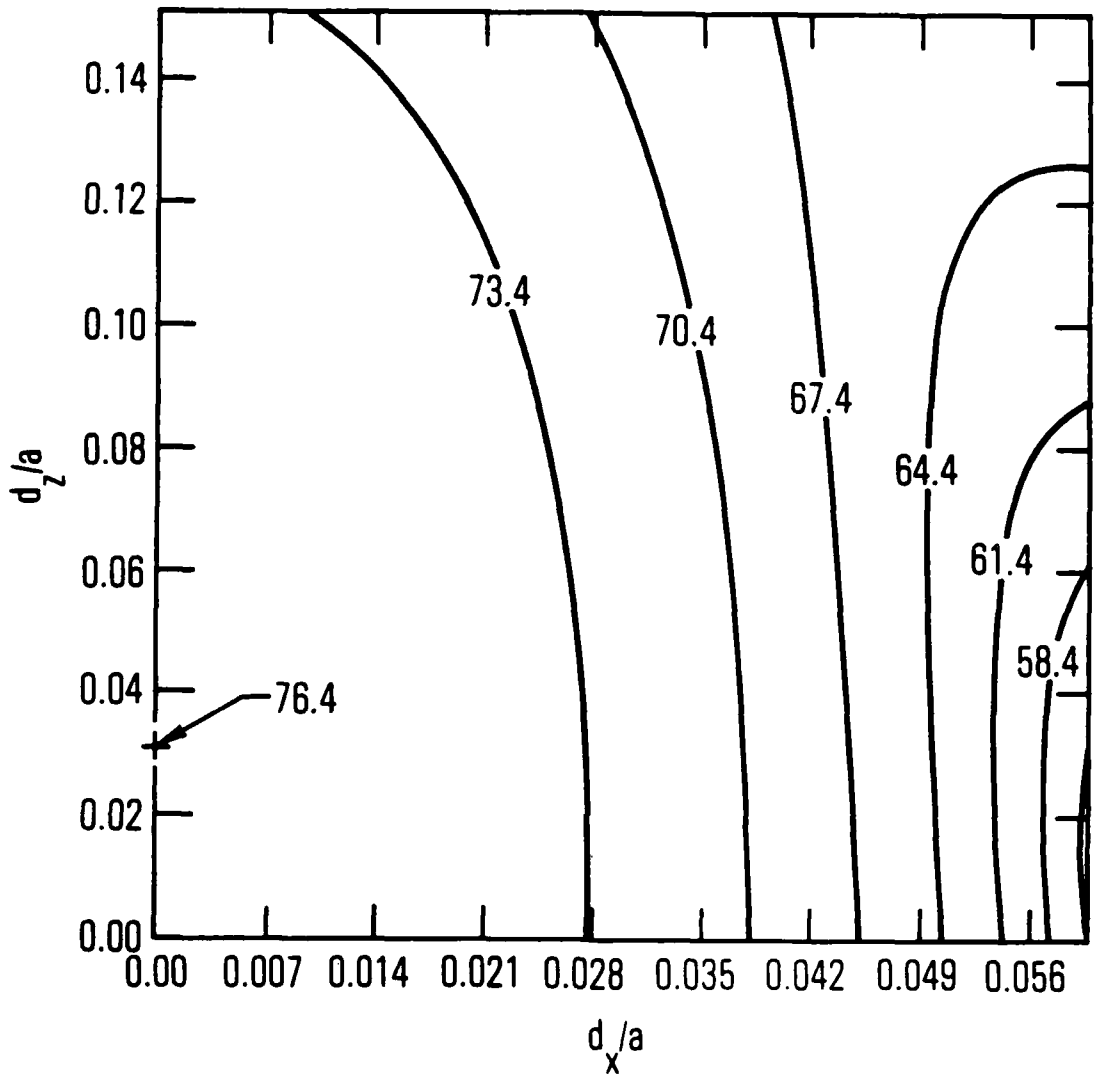

Figure 11. Contour Plot of Total Field in Focal Region of Paraboloid ka = 100, ϕ_0 = 0°, a/D = 0.8

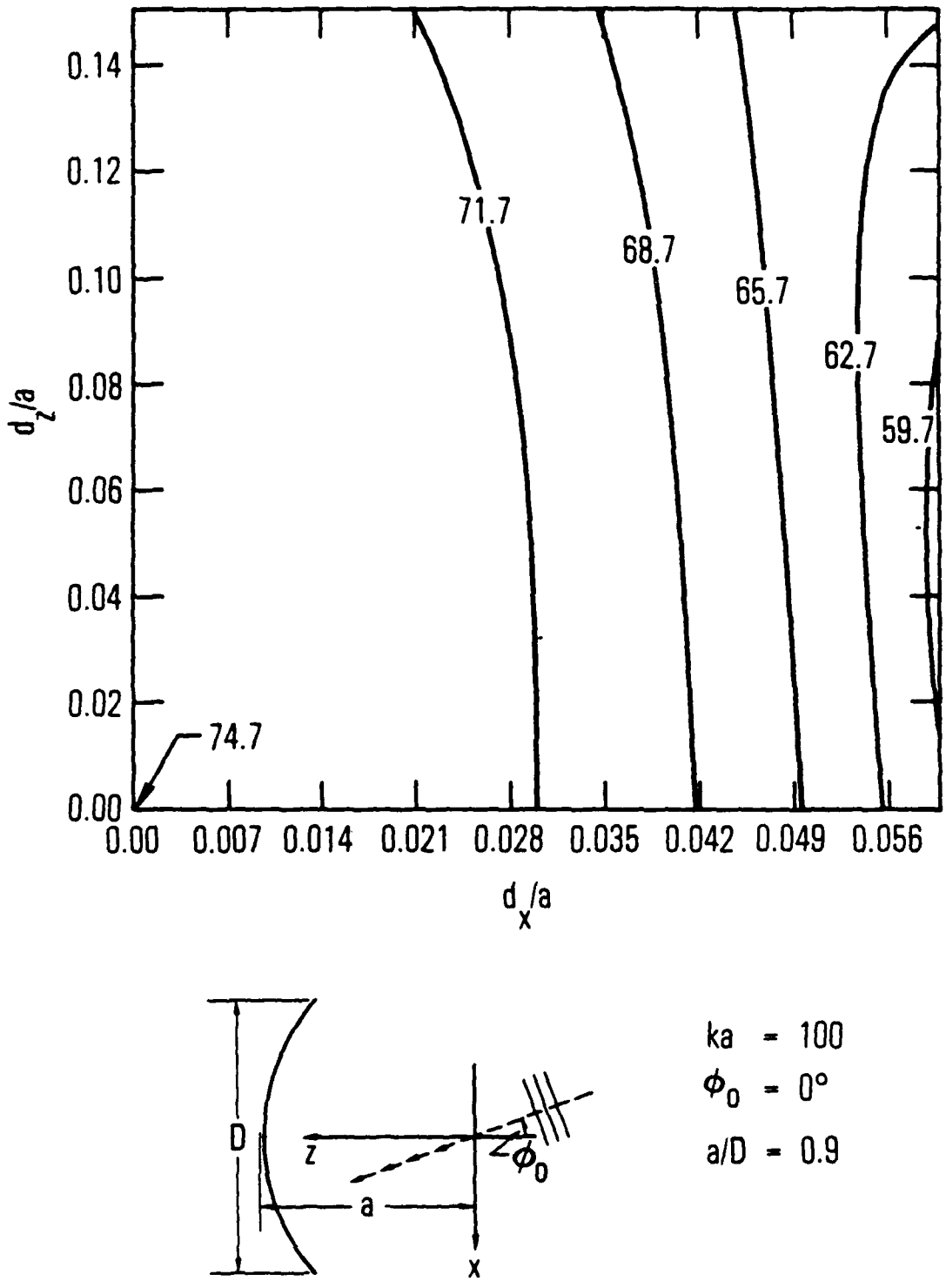

Figure 12. Contour Plot of Total Field in Focal Region of Paraboloid ka = 100, ϕ_0 = 0°, a/D = 0.9

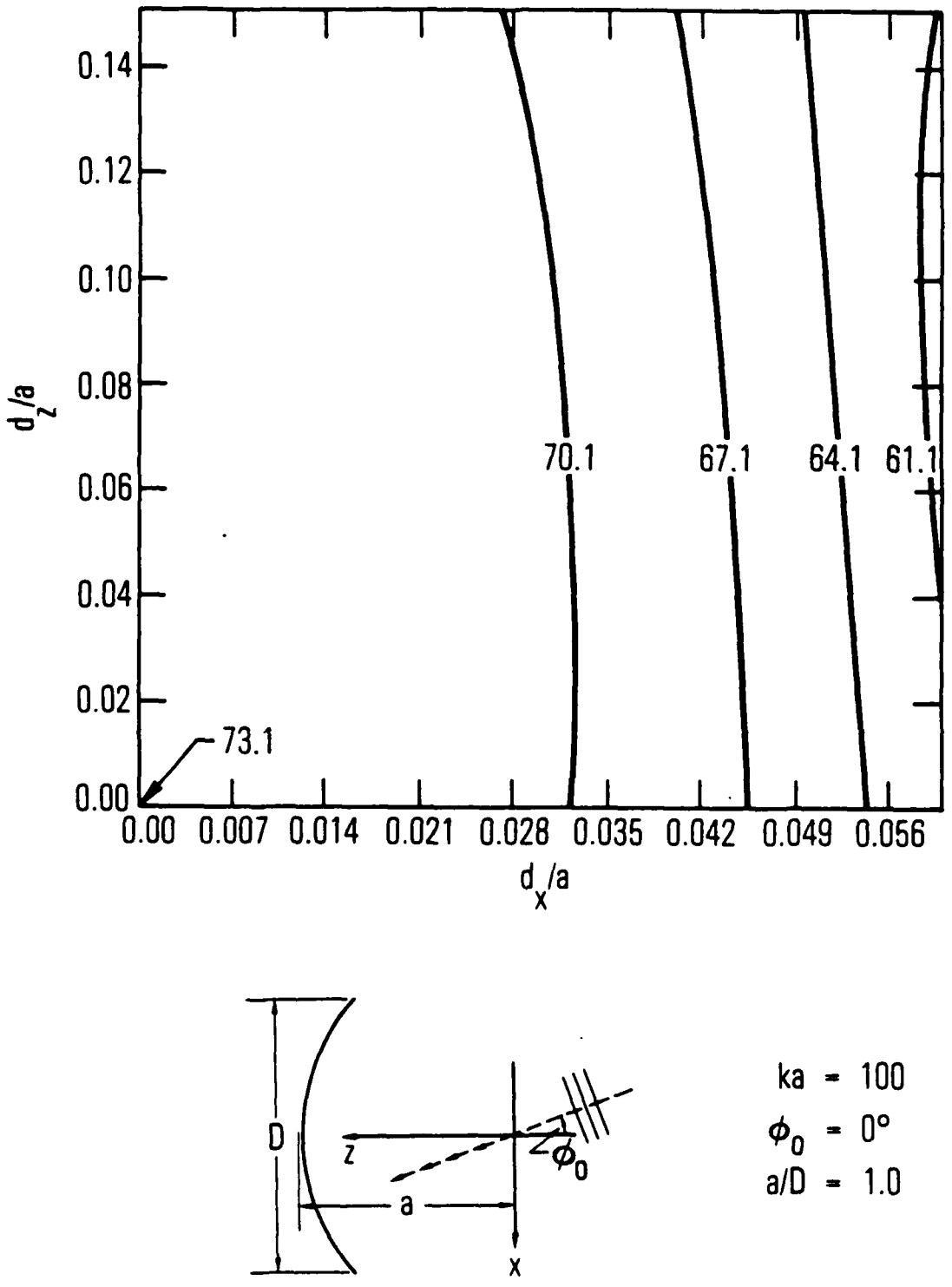

Figure 13. Contour Plot of Total Field in Focal Region of Paraboloid ka = 100, ϕ_o = 0°, a/D = 1.0

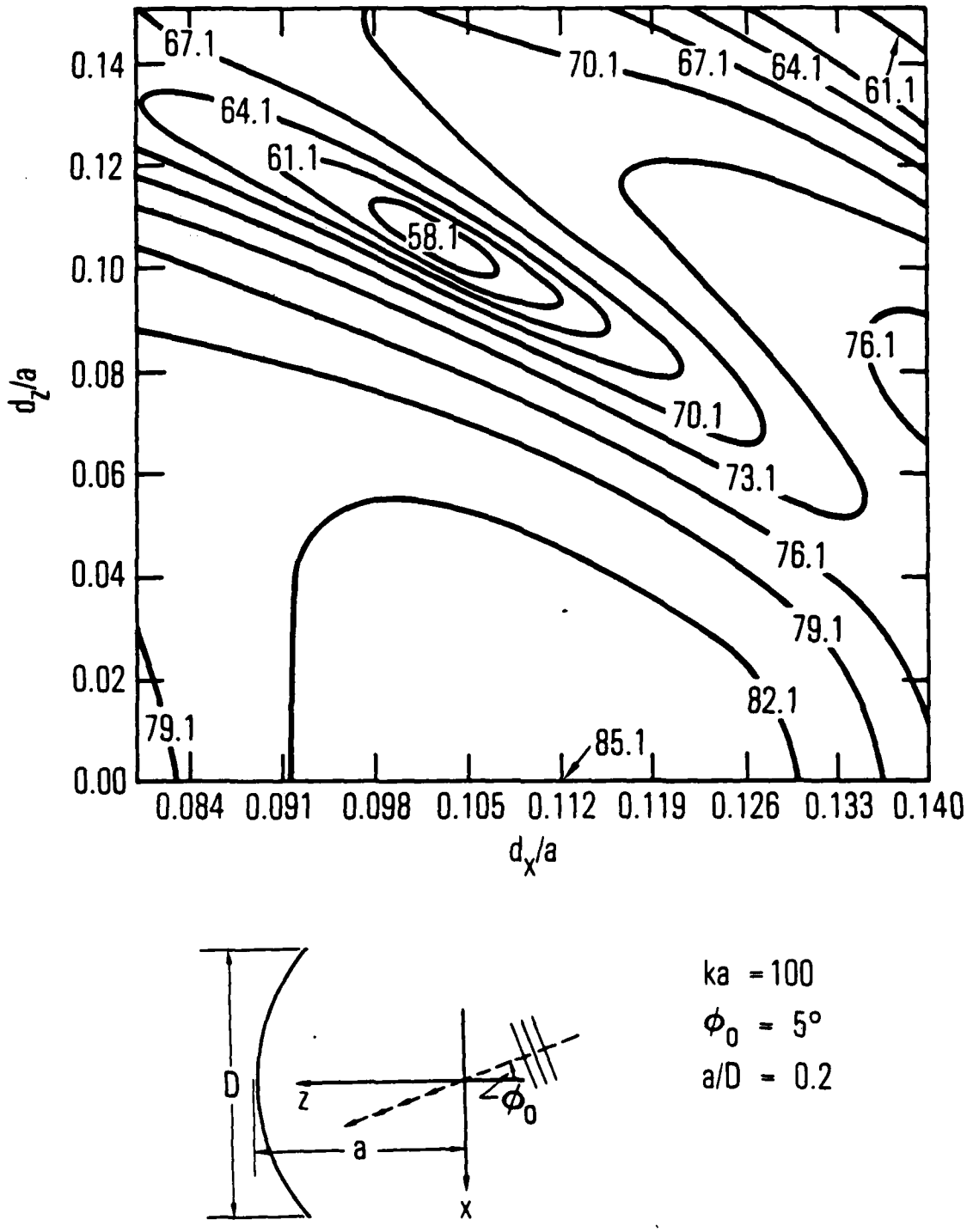

Figure 14. Contour Plot of Total Field in Focal Region of Paraboloid ka = 100, ϕ_0 = 5°, a/D = 0.2

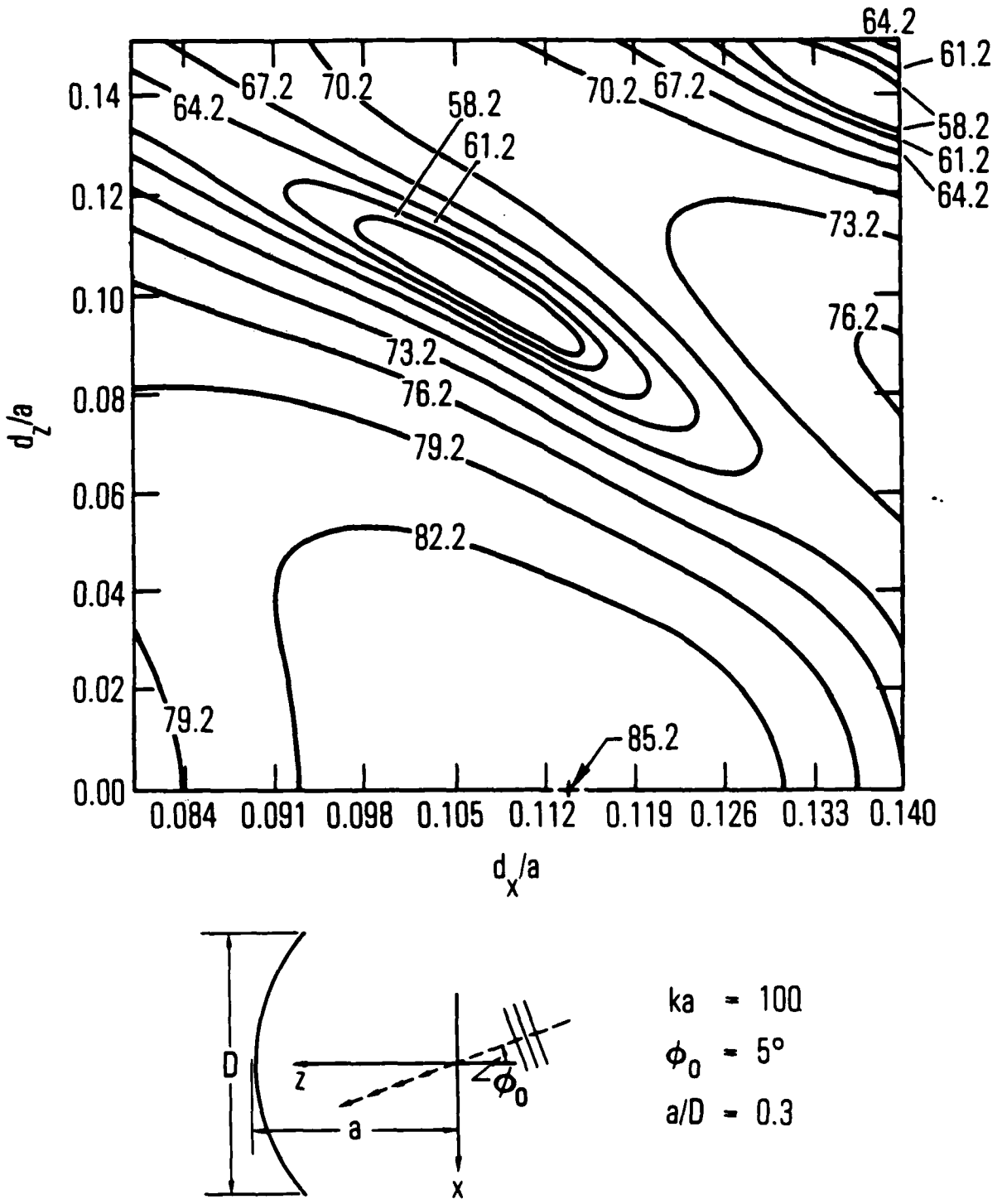

Figure 15. Contour Plot of Total Field in Focal Region of Paraboloid ka = 100, ϕ_0 = 5°, a/D = 0.3

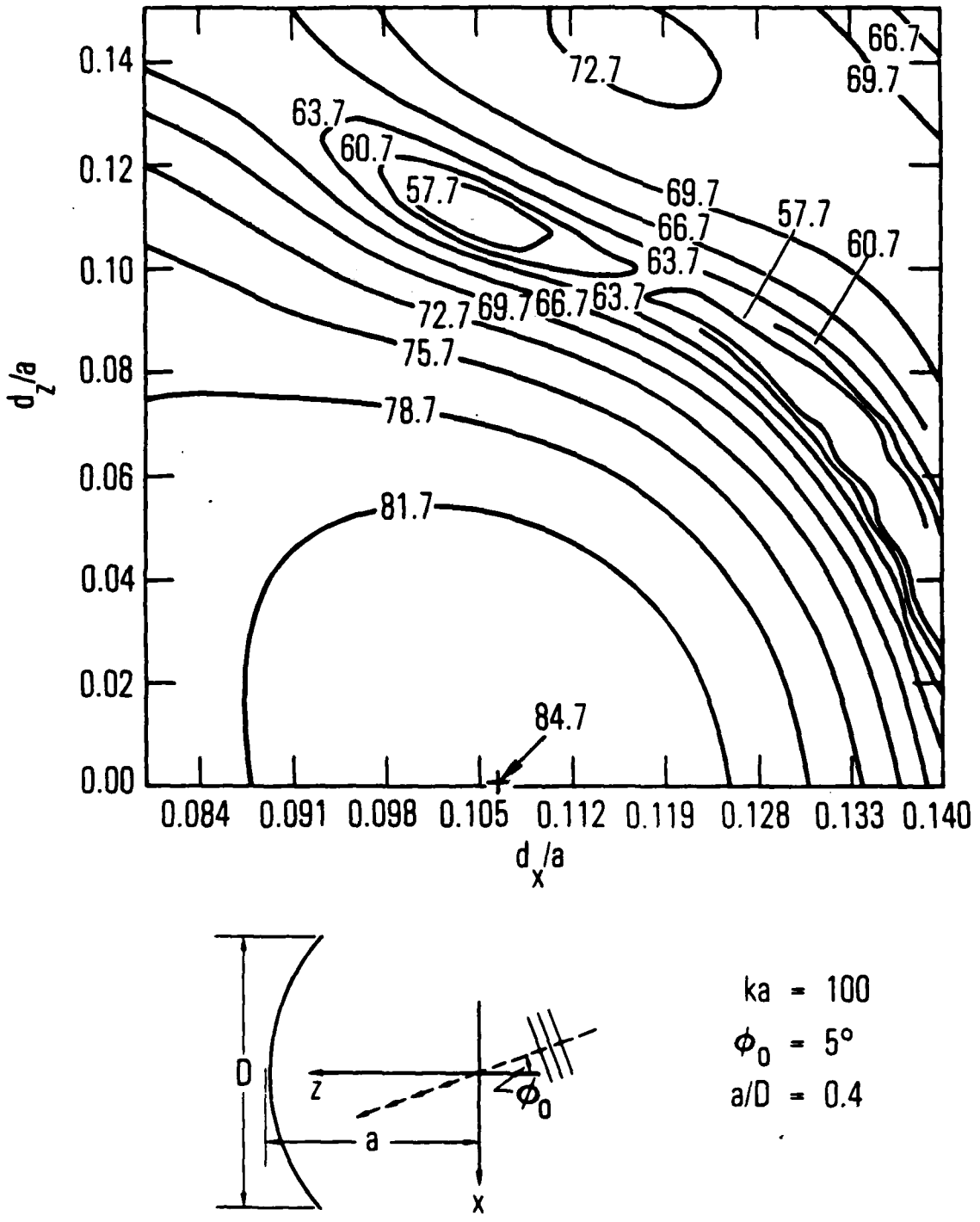

Figure 16. Contour Plot of Total Field in Focal Region of Paraboloid ka = 100, ϕ_o = 5°, a/D = 0.4

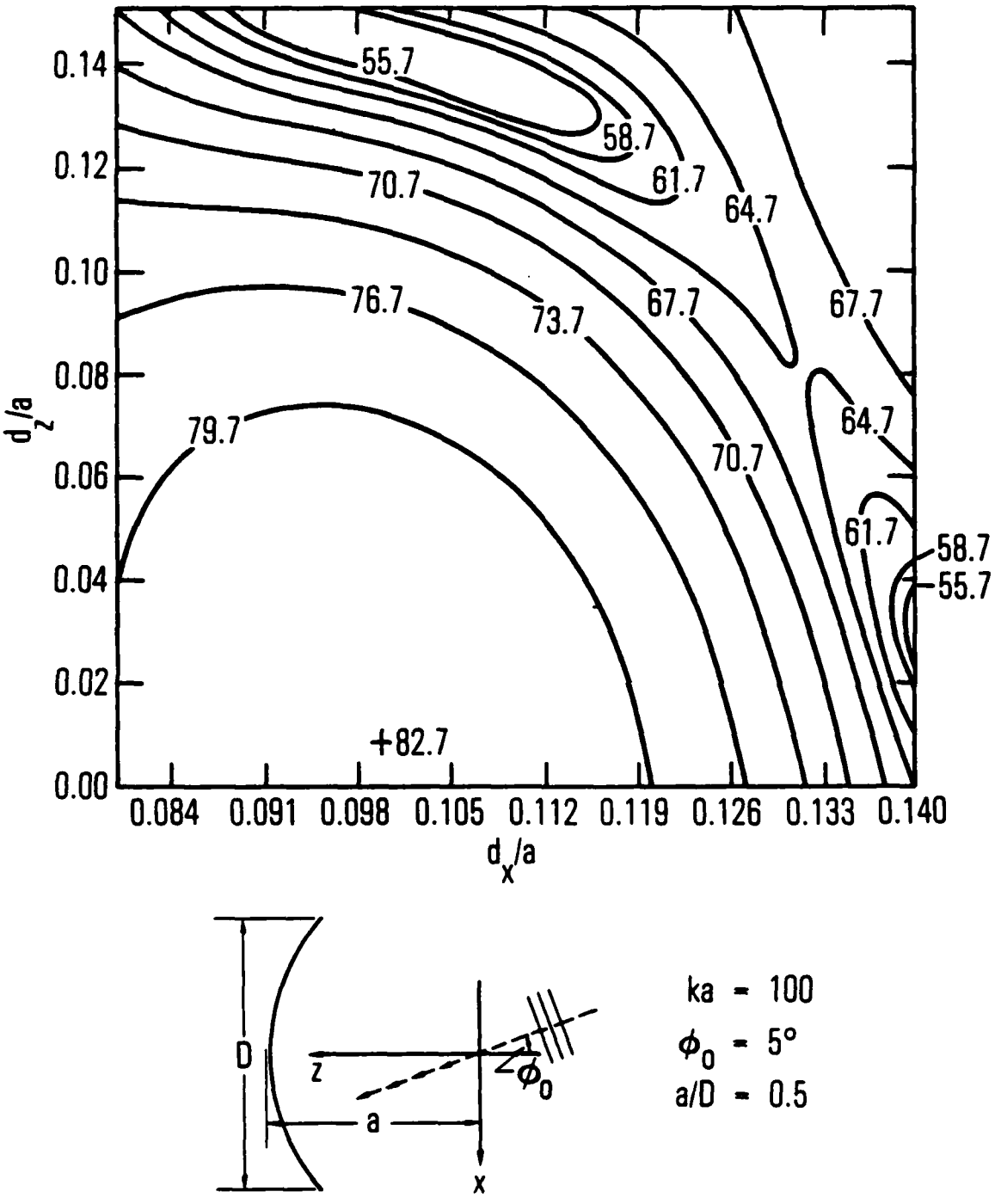

Figure 17. Contour Plot of Total Field in Focal Region of Paraboloid ka = 100, ϕ_0 = 5°, a/D = 0.5

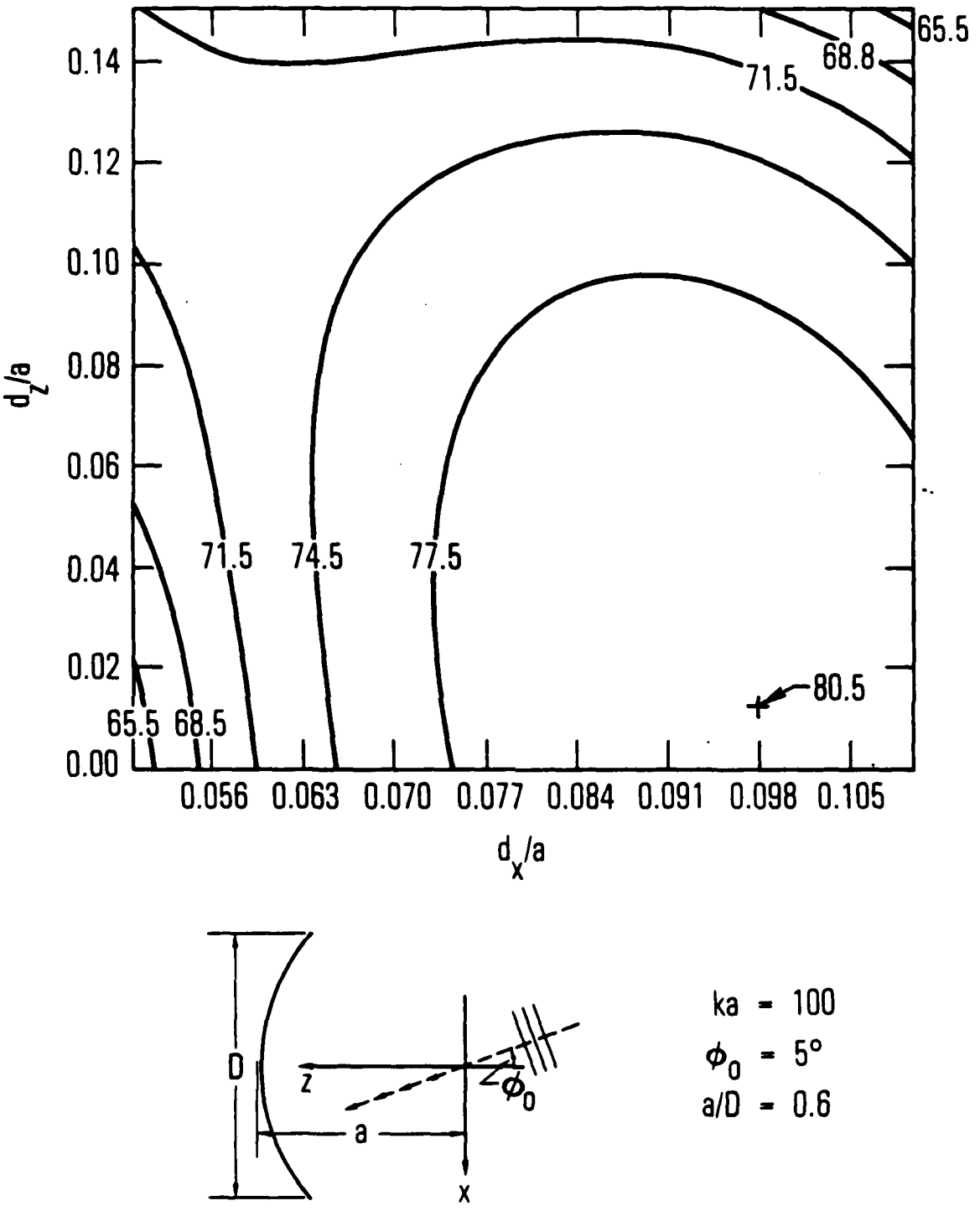

Figure 18. Contour Plot of Total Field in Focal Region of Paraboloid ka = 100, ϕ_o = 5°, a/D = 0.6

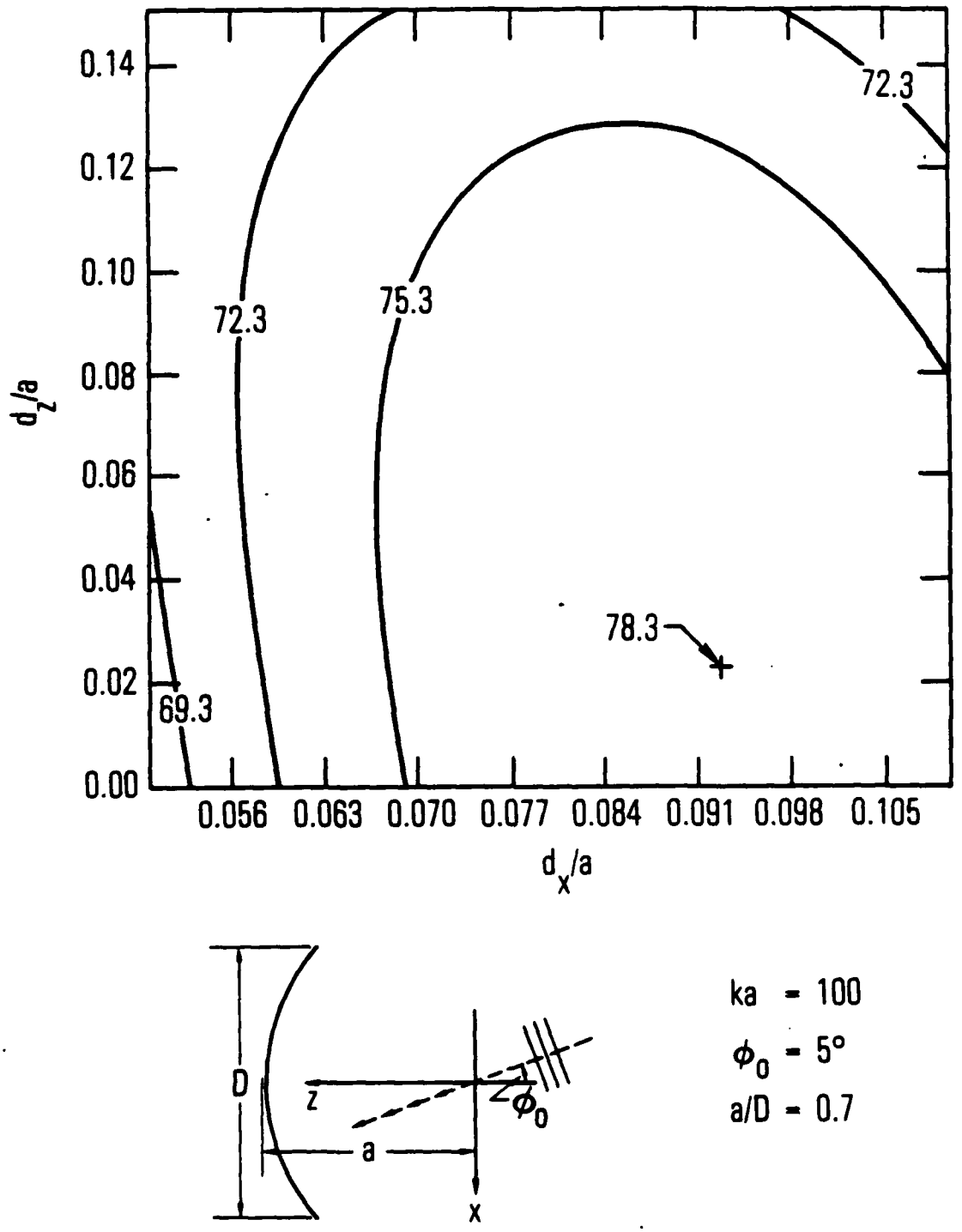

Figure 19. Contour Plot of Total Field in Focal Region of Paraboloid ka = 100, ϕ_0 = 5°, a/D = 0.7

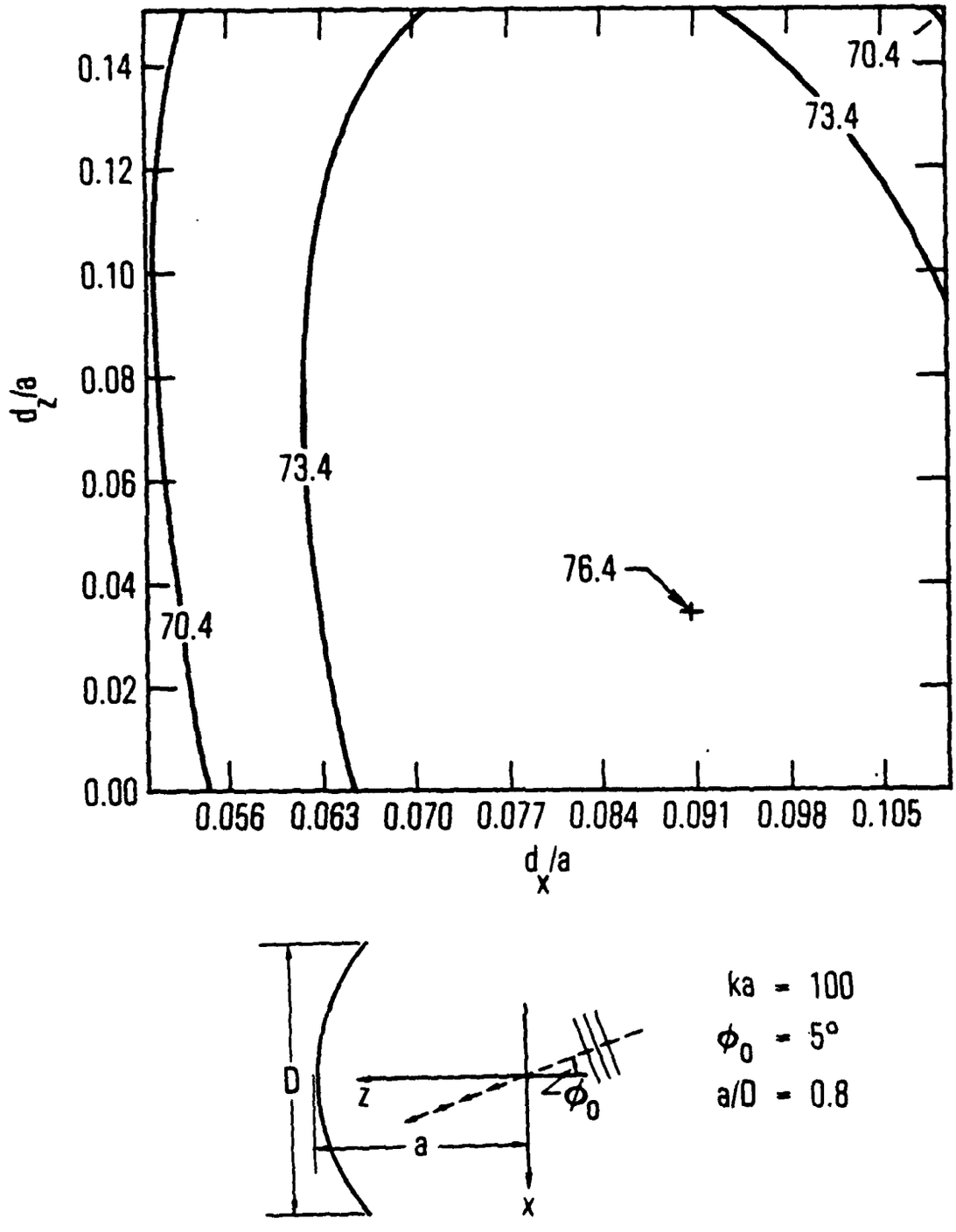

Figure 20. Contour Plot of Total Field in Focal Region of Paraboloid ka = 100, ϕ_0 = 5°, a/D = 0.8

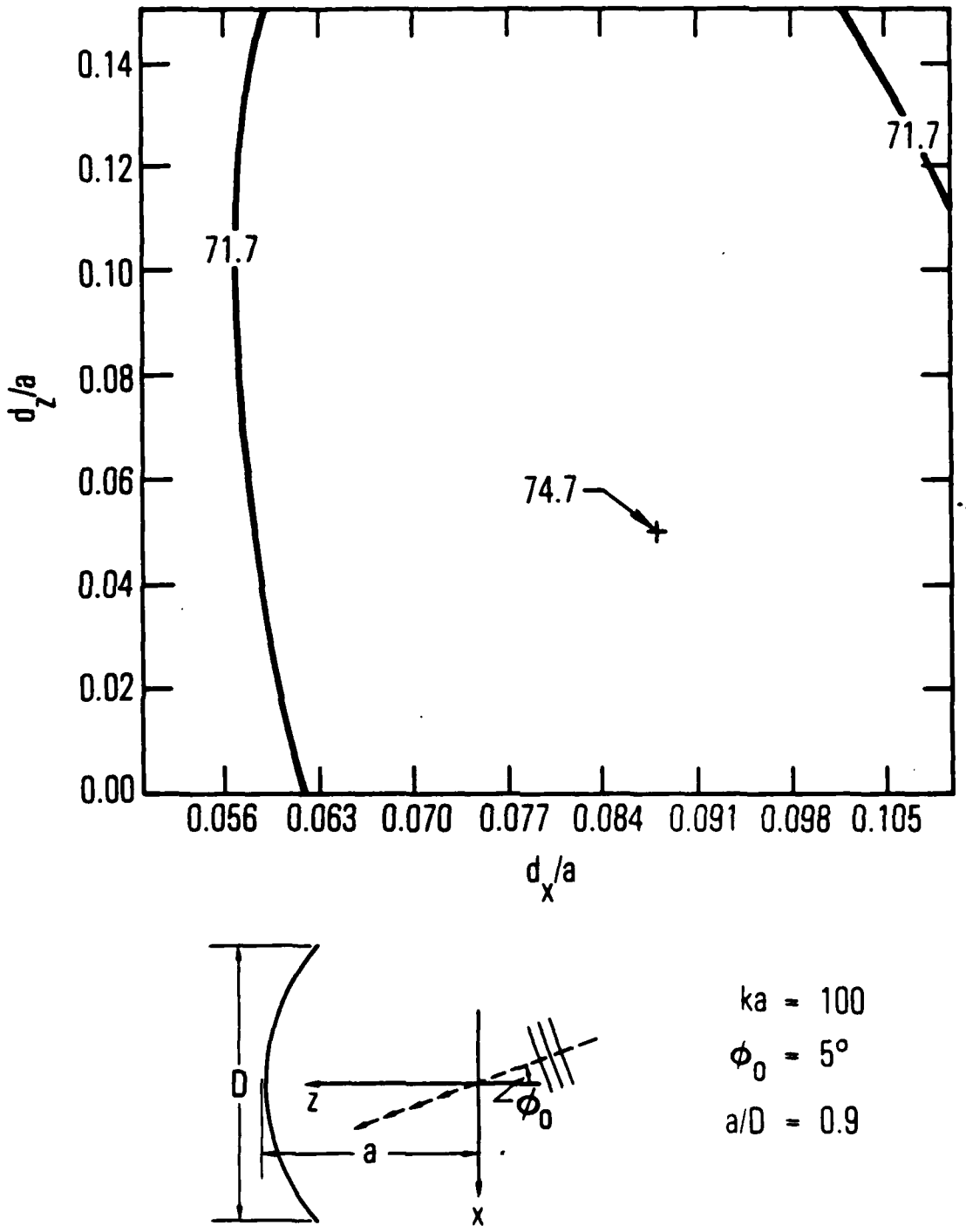

Figure 21. Contour Plot of Total Field in Focal Region of Paraboloid ka = 100, ϕ_0 = 5°, a/D = 0.9

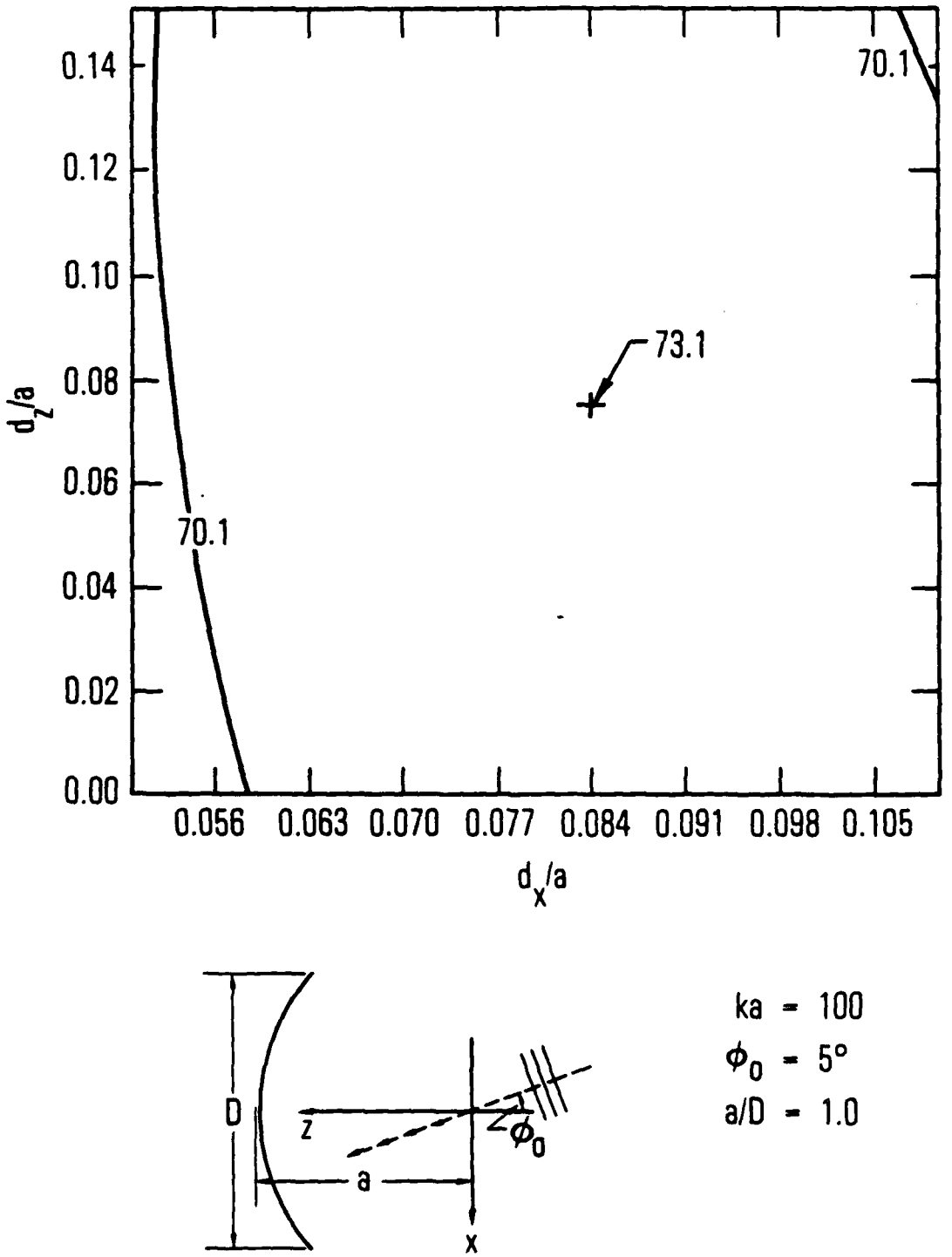

Figure 22. Contour Plot of Focal Field in Focal Region of Paraboloid ka = 100, ϕ_0 = 5°, a/D = 1.0

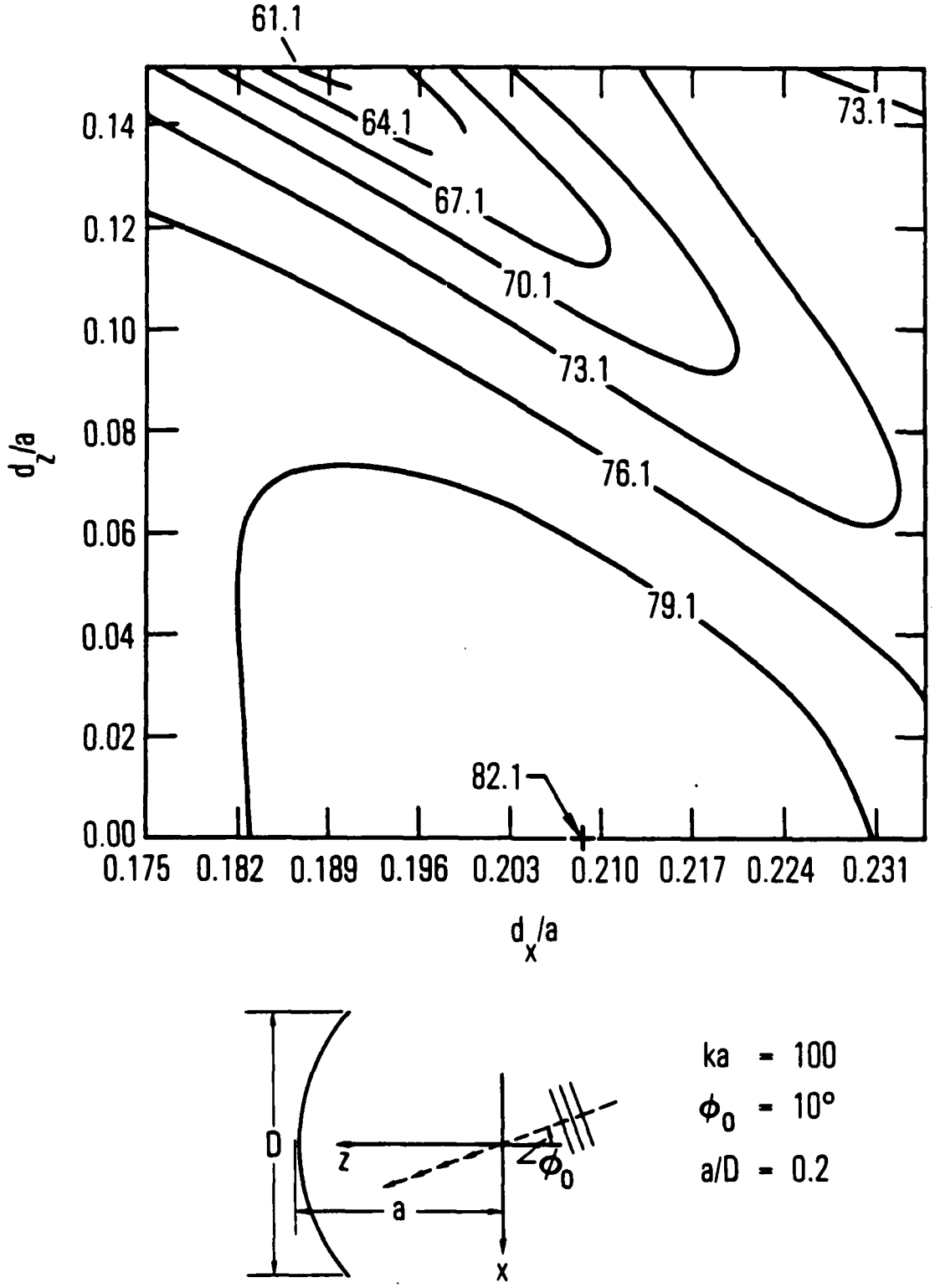

Figure 23. Contour Plot of Total Field in Focal Region of Paraboloid ka = 100, ϕ_o = 10°, a/D = 0.2

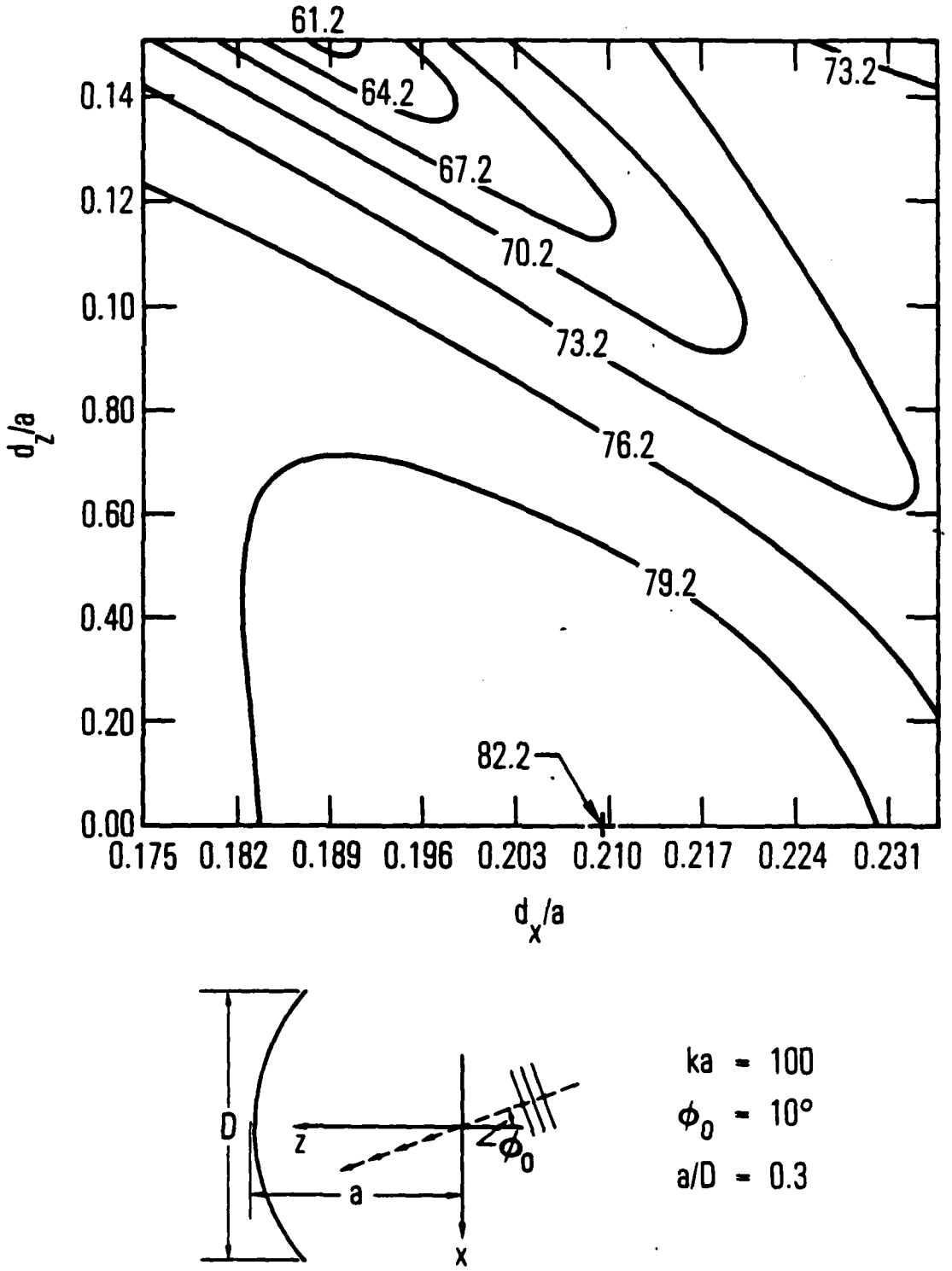

Figure 24. Contour Plot of Total Field in Focal Region of Paraboloid ka = 100, ϕ_0 = 10°, a/D = 0.3

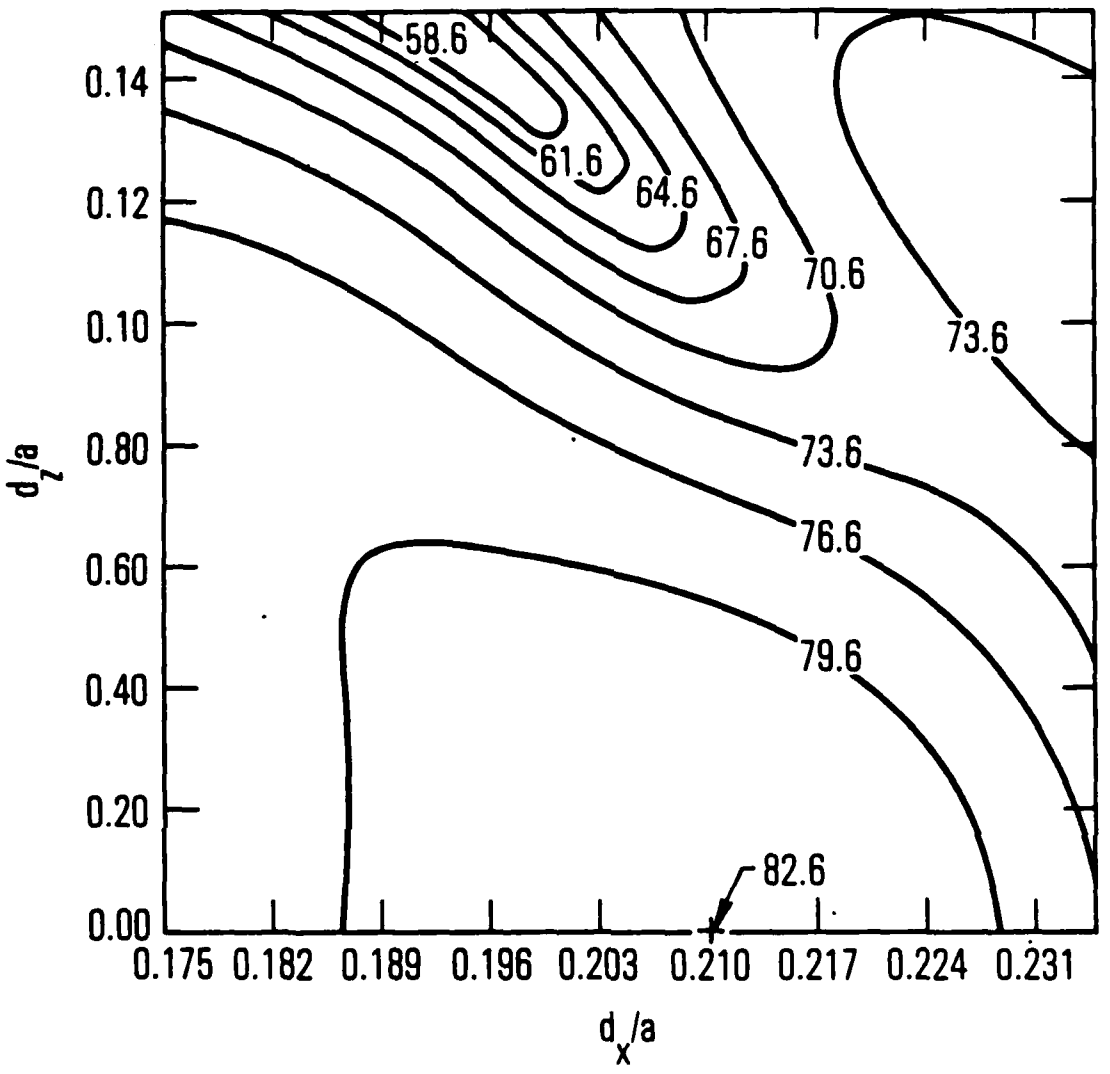

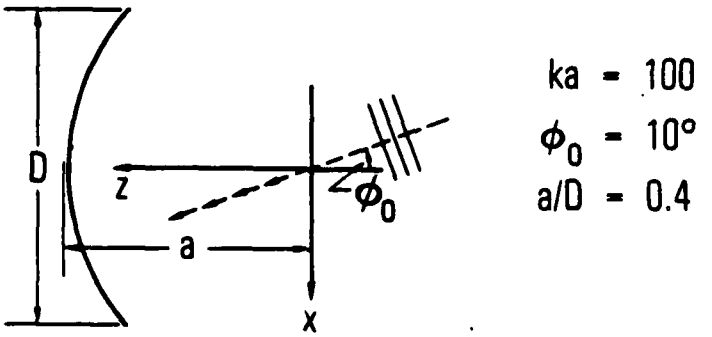

Figure 25. Contour Plot of Total Field in Focal Region of Paraboloid ka = 100, ϕ_o = 10°, a/D = 0.4

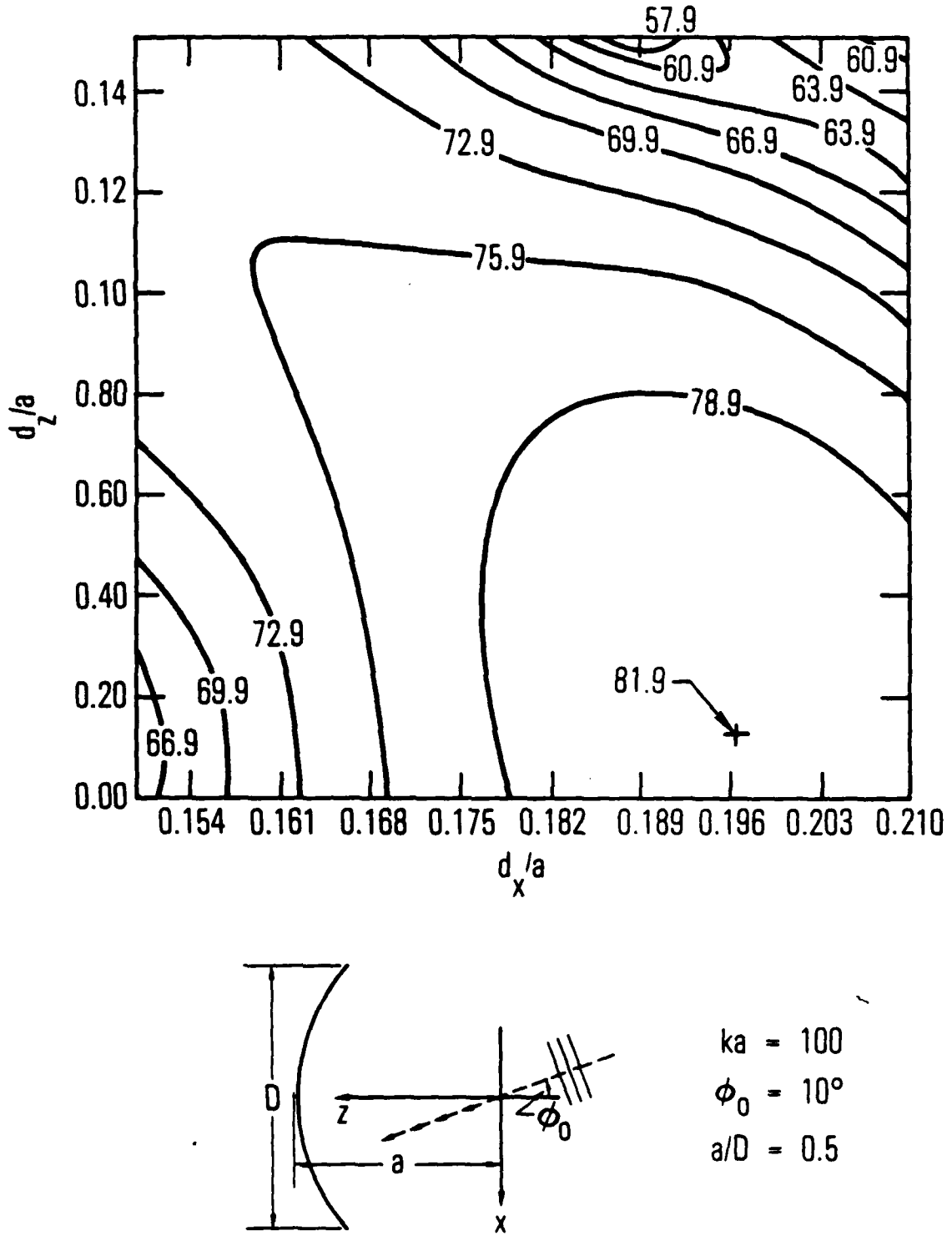

Figure 26. Contour Plot of Total Field in Focal Region of Paraboloid ka = 100, ϕ_0 = 10°, a/D = 0.5

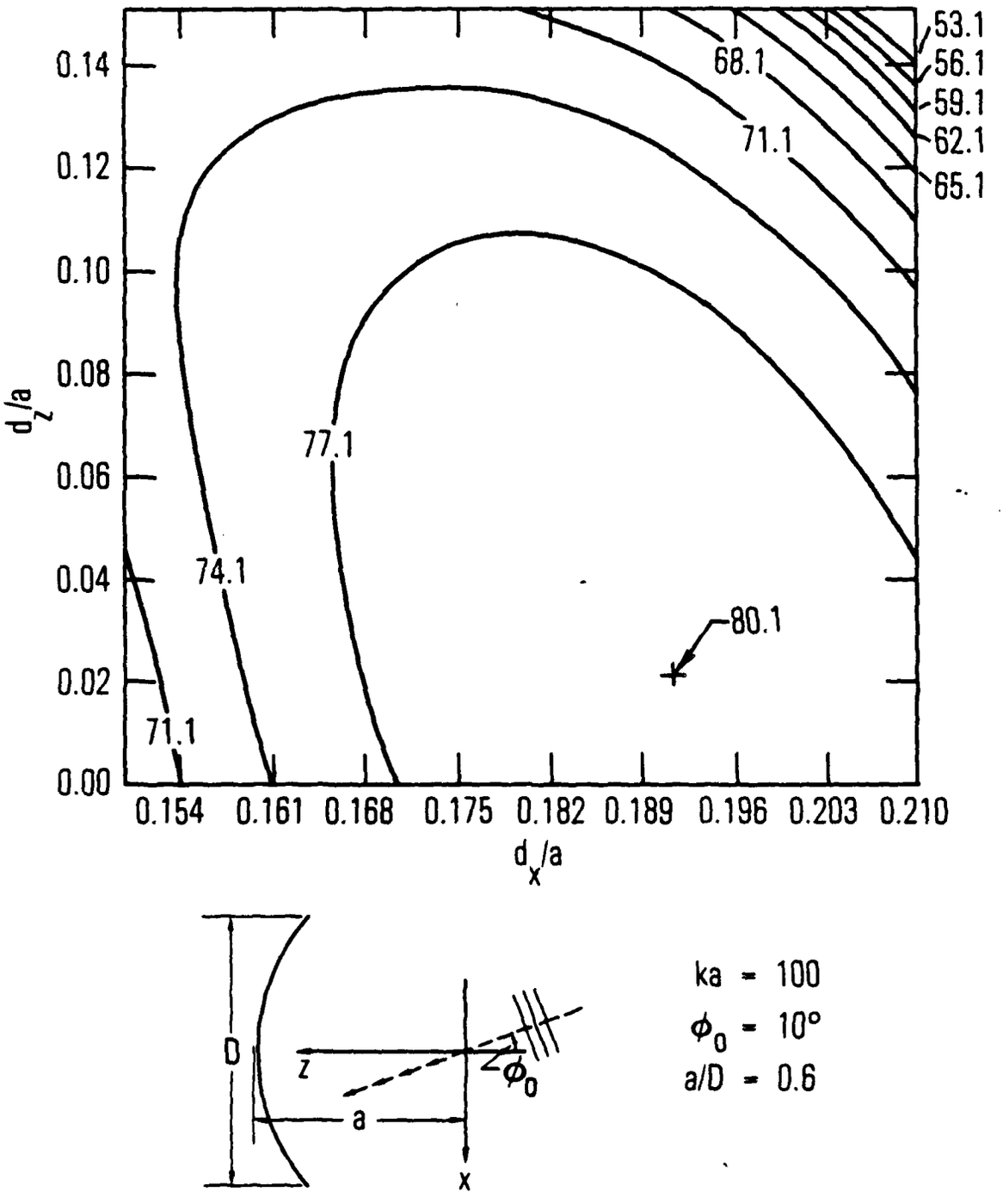

Figure 27. Contour Plot of Total Field in Focal Region of Paraboloid ka = 100, ϕ_o = 10°, a/D = 0.6

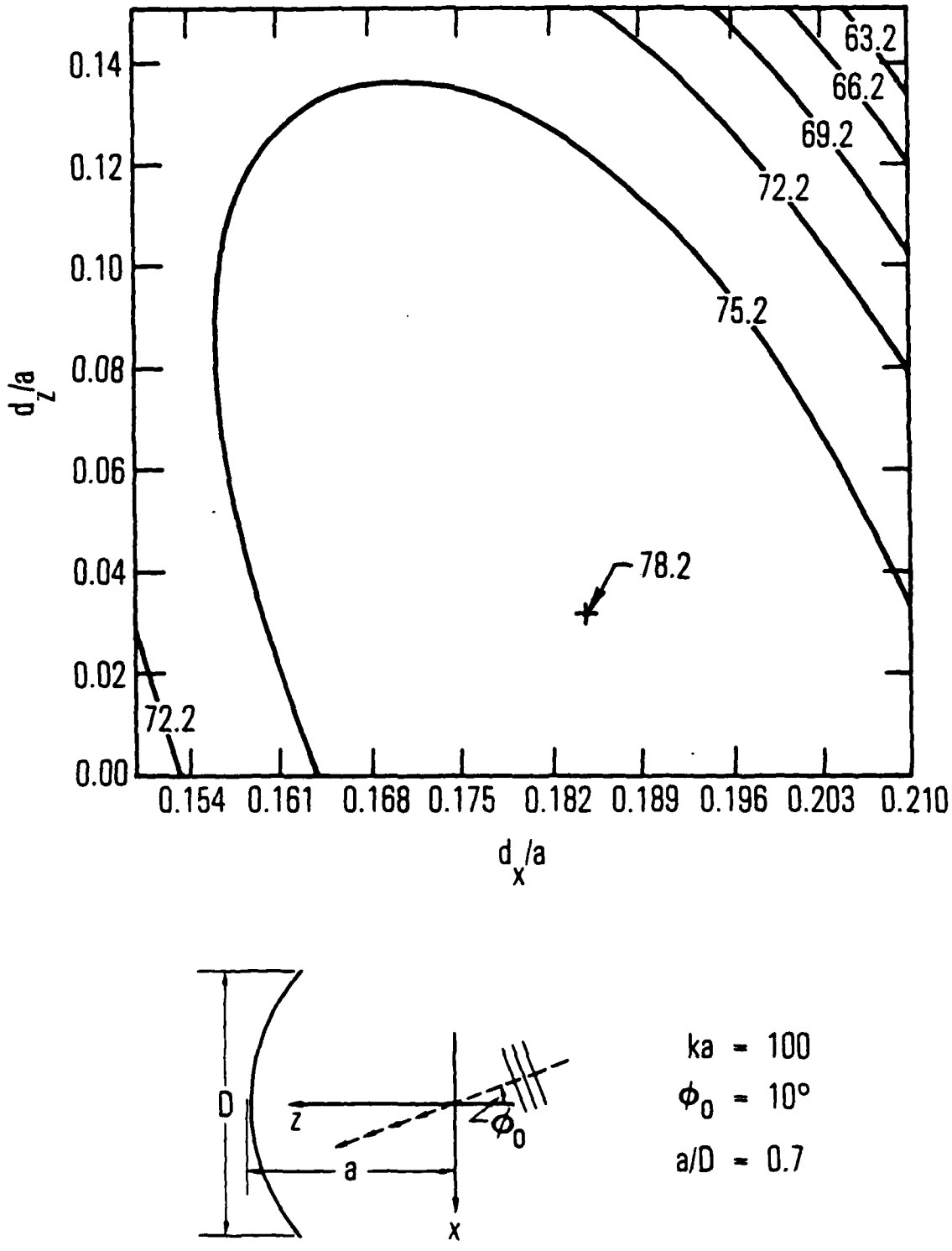

Figure 28. Contour Plot of Total Field in Focal Region of Paraboloid ka = 100, ϕ_o = 10°, a/D = 0.7

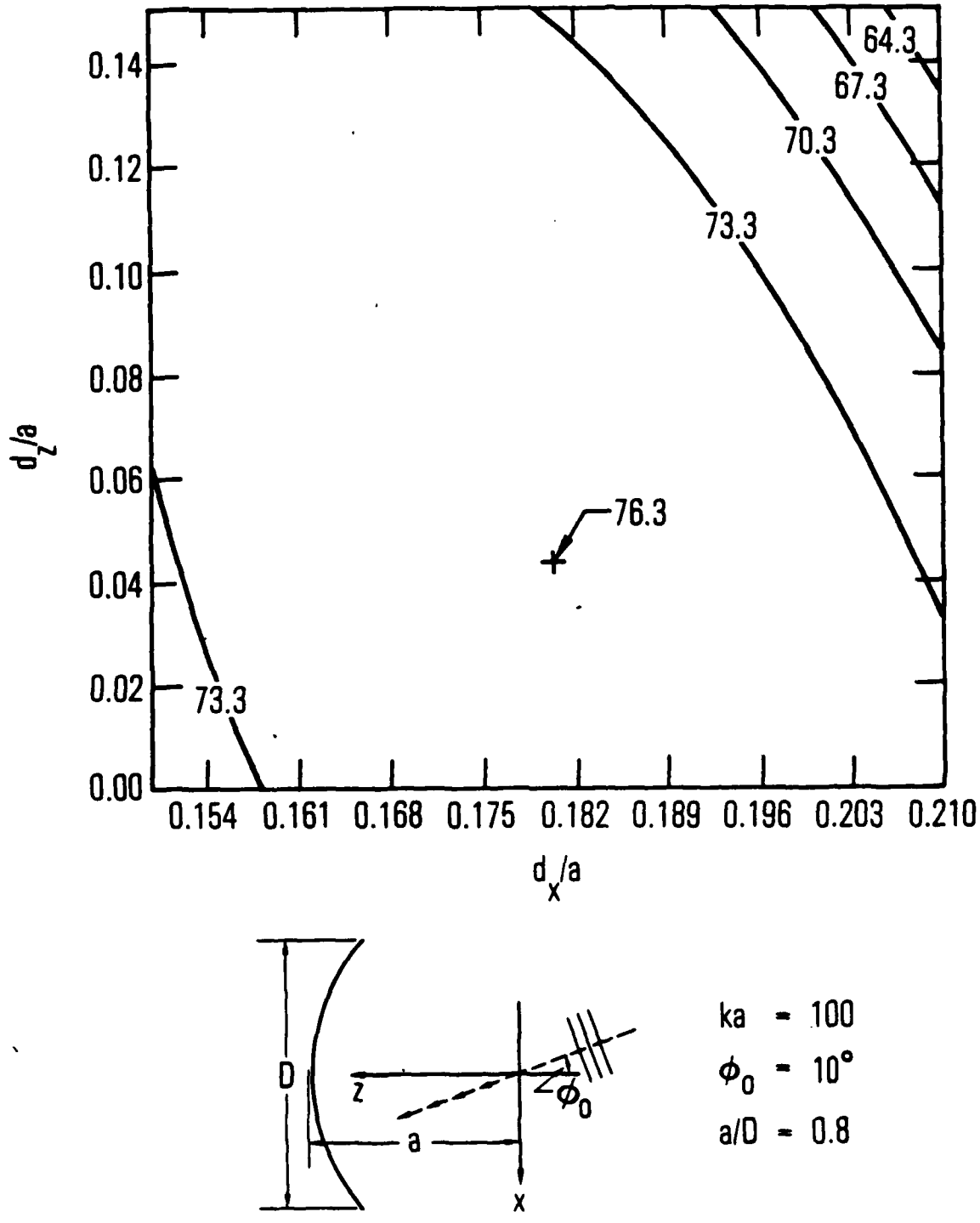

Figure 29. Contour Plot of Total Field in Focal Region of Paraboloid ka = 100, ϕ_o = 10°, a/D = 0.8

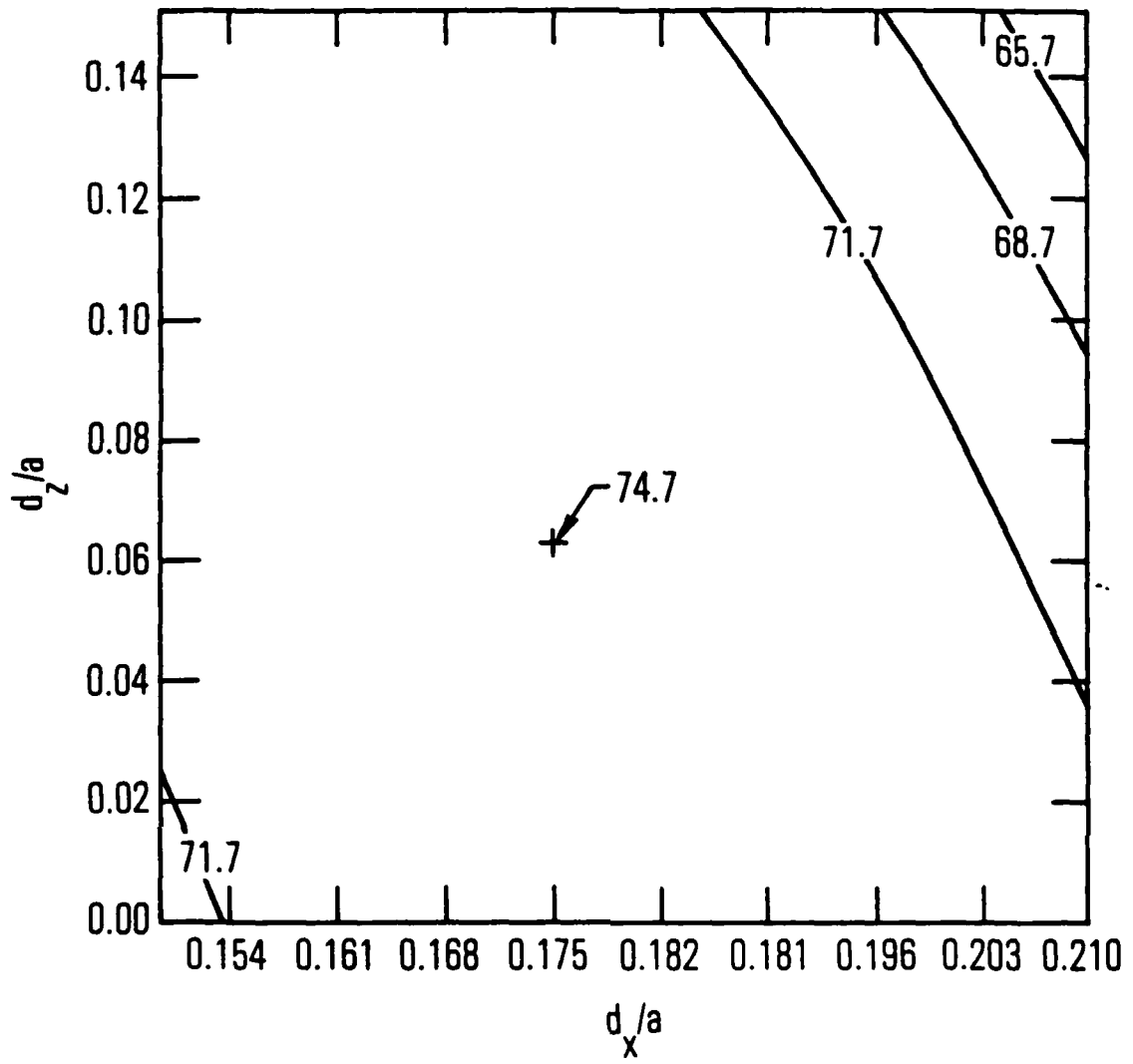

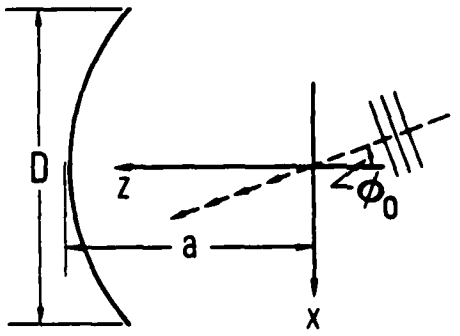

ka = 100
ϕ_0 = 10°
a/D = 0.9

Figure 30. Contour Plot of Total Field in Focal Region of Paraboloid ka = 100, ϕ_0 = 10°, a/D = 0.9

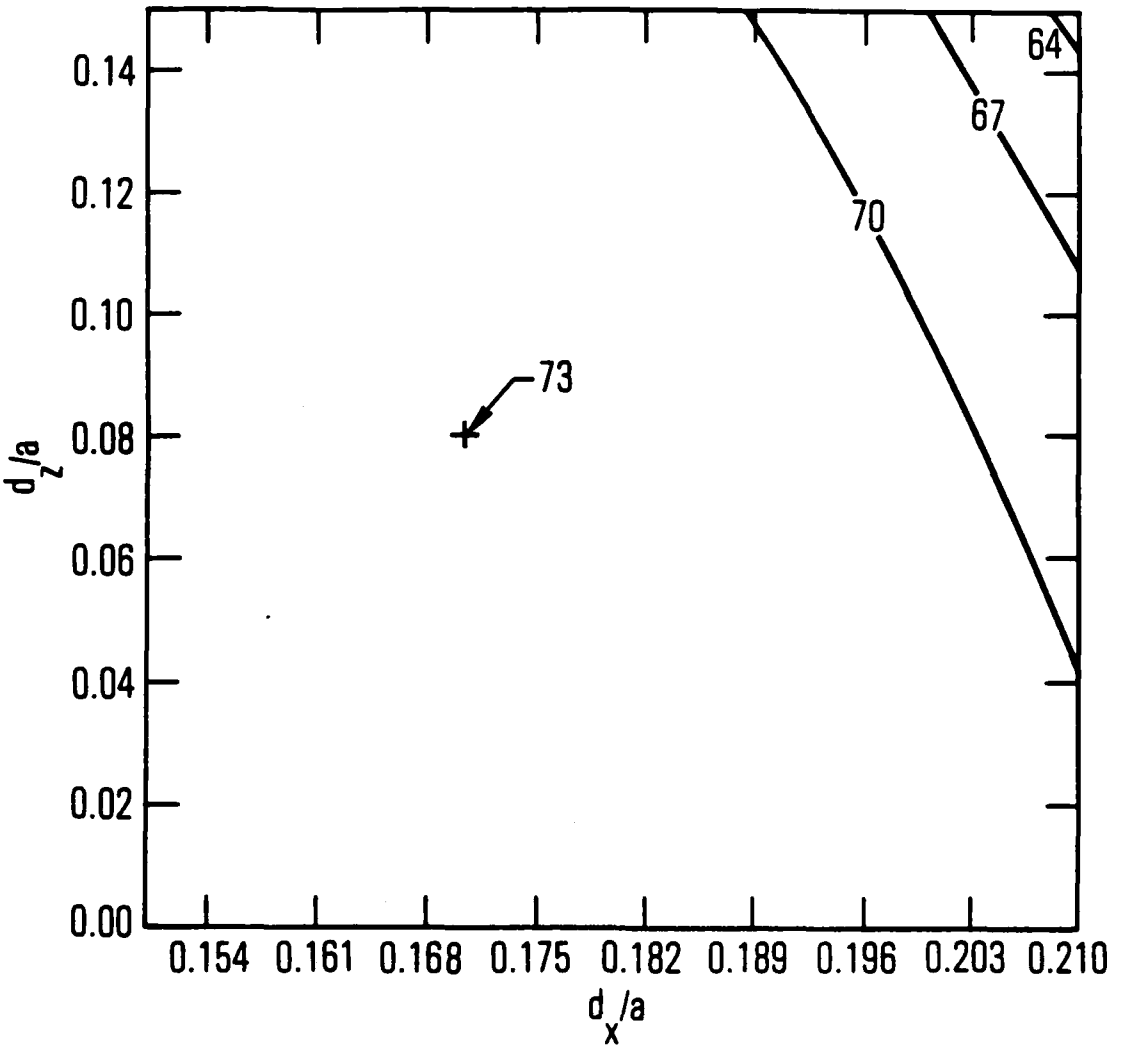

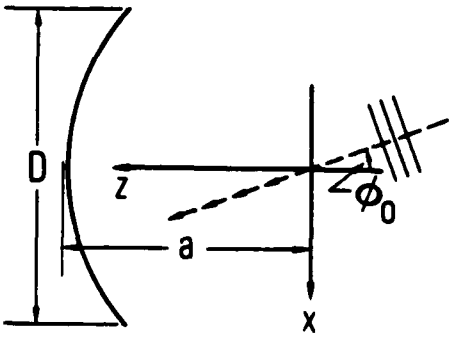

ka = 100
ϕ_0 = 10°
a/D = 1.0

Figure 31. Contour Plot of Total Field in Focal Region of Paraboloid ka = 100, ϕ_o = 10°, a/D = 1.0

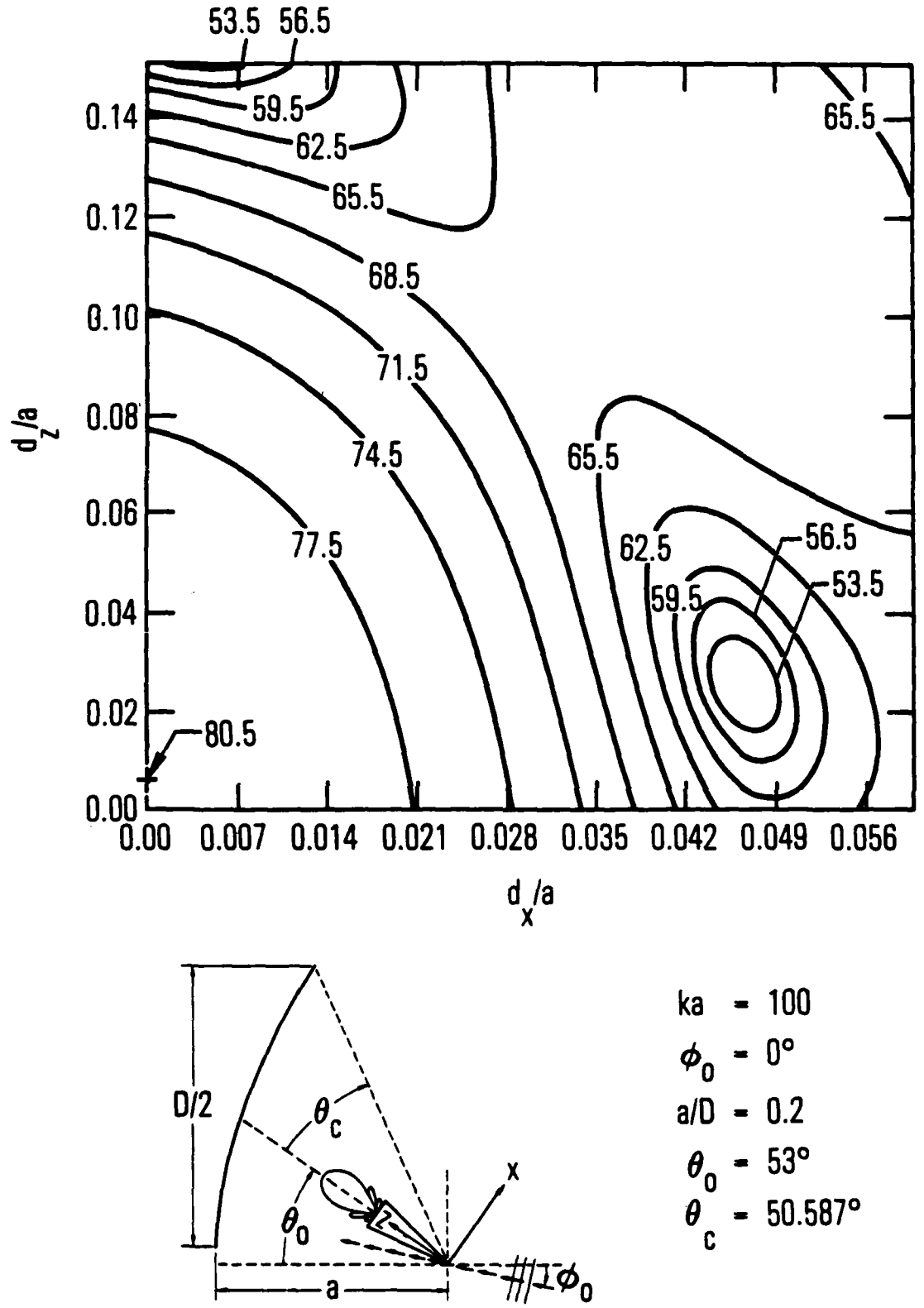

Figure 32. Contour Plot of Total Field in Focal Region of Offset Paraboloid ka = 100, ϕ_o = 0°, a/D = 0.2, θ_o = 53°, θ_c = 50.587°

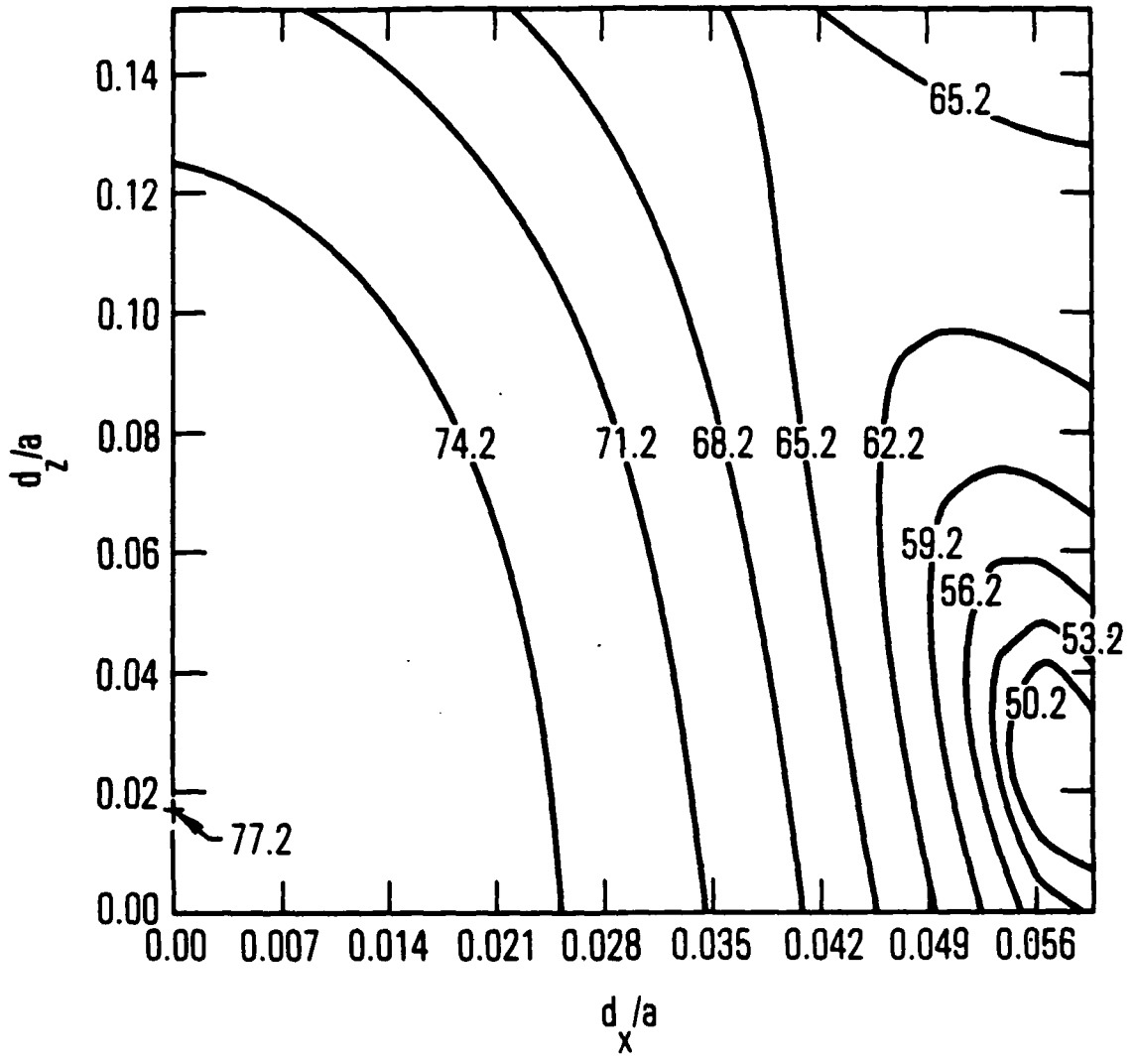

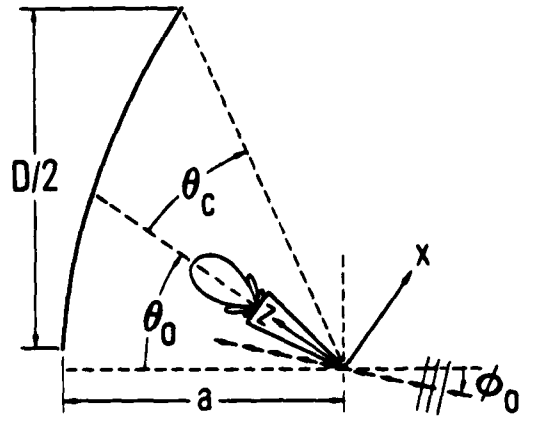

ka = 100
ϕ_0 = 0°
a/D = 0.3
θ_0 = 42
θ_c = 39.206

Figure 33. Contour Plot of Total Field in Focal Region of Offset Paraboloid ka = 100, ϕ_o = 0°, a/D = 0.3, θ_o = 42°, θ_c = 39.206°

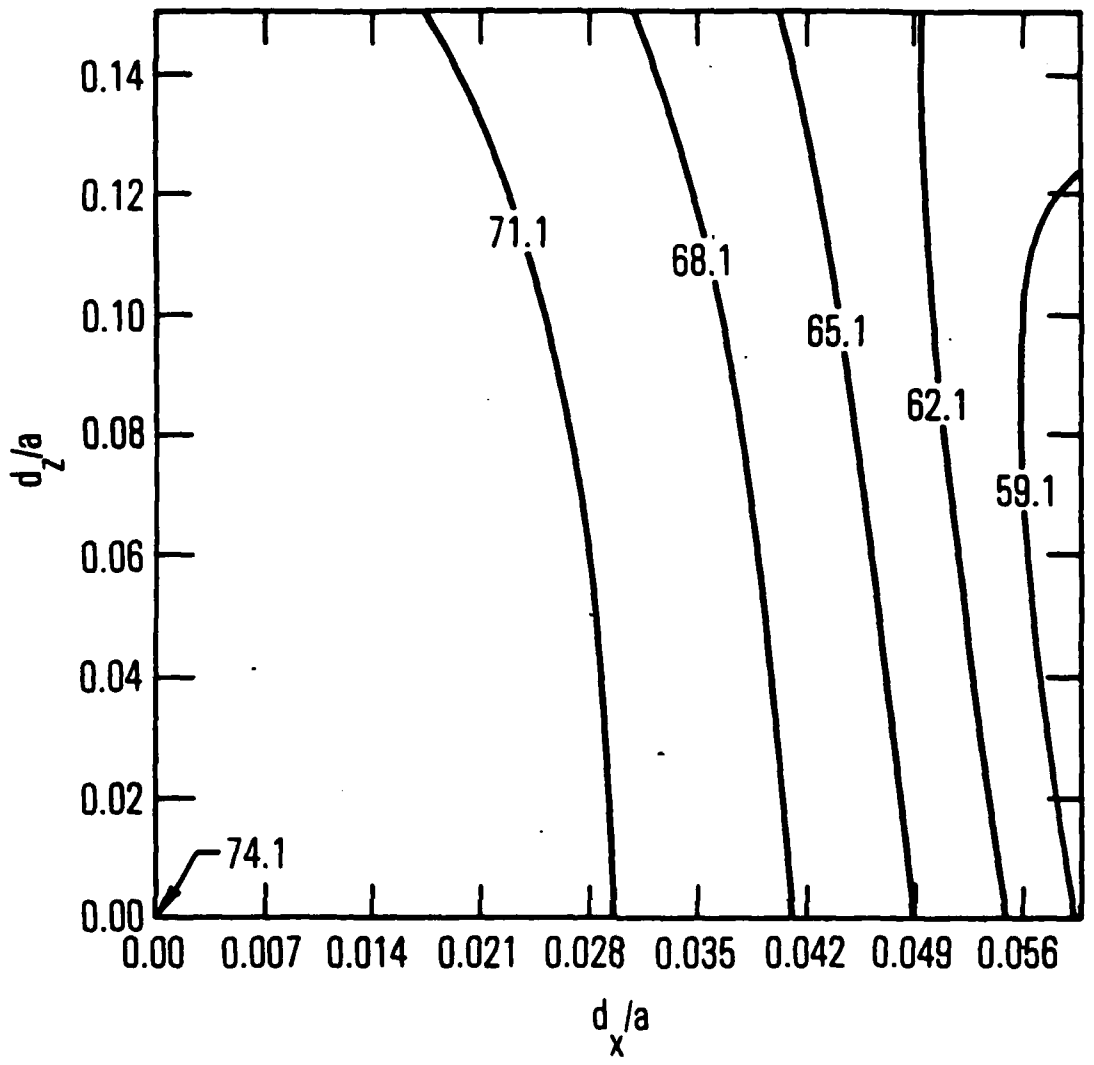

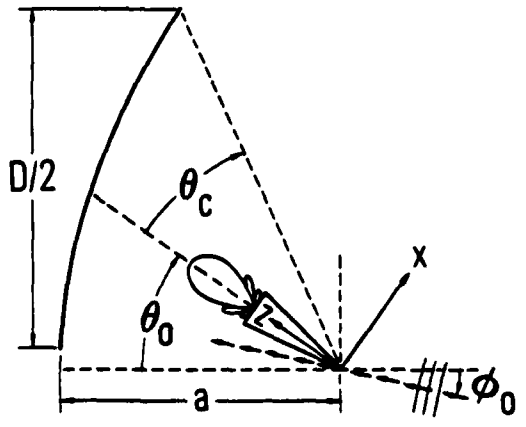

ka = 100
ϕ_0 = 0°
a/D = 0.4
θ_0 = 35.
θ_c = 31.465

Figure 34. Contour Plot of Total Field in Focal Region of Offset Paraboloid ka = 100, ϕ_o = 0°, a/D = 0.4, θ_o = 35°, θ_c = 31.465°

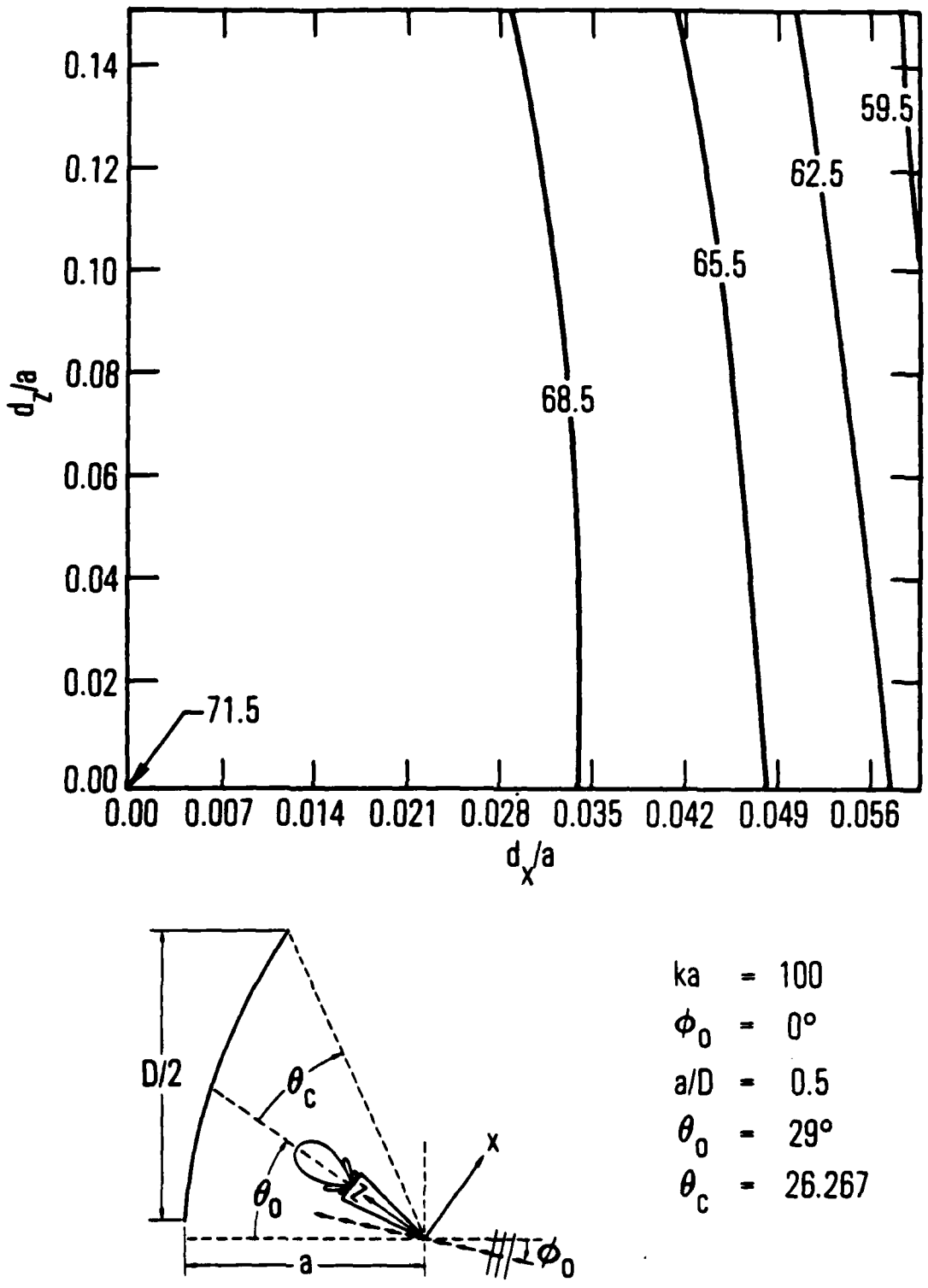

Figure 35. Contour Plot of Total Field in Focal Region of Offset Paraboloid ka = 100, ϕ_o = 0°, a/D = 0.5, θ_o = 29°, θ_c = 26.267°

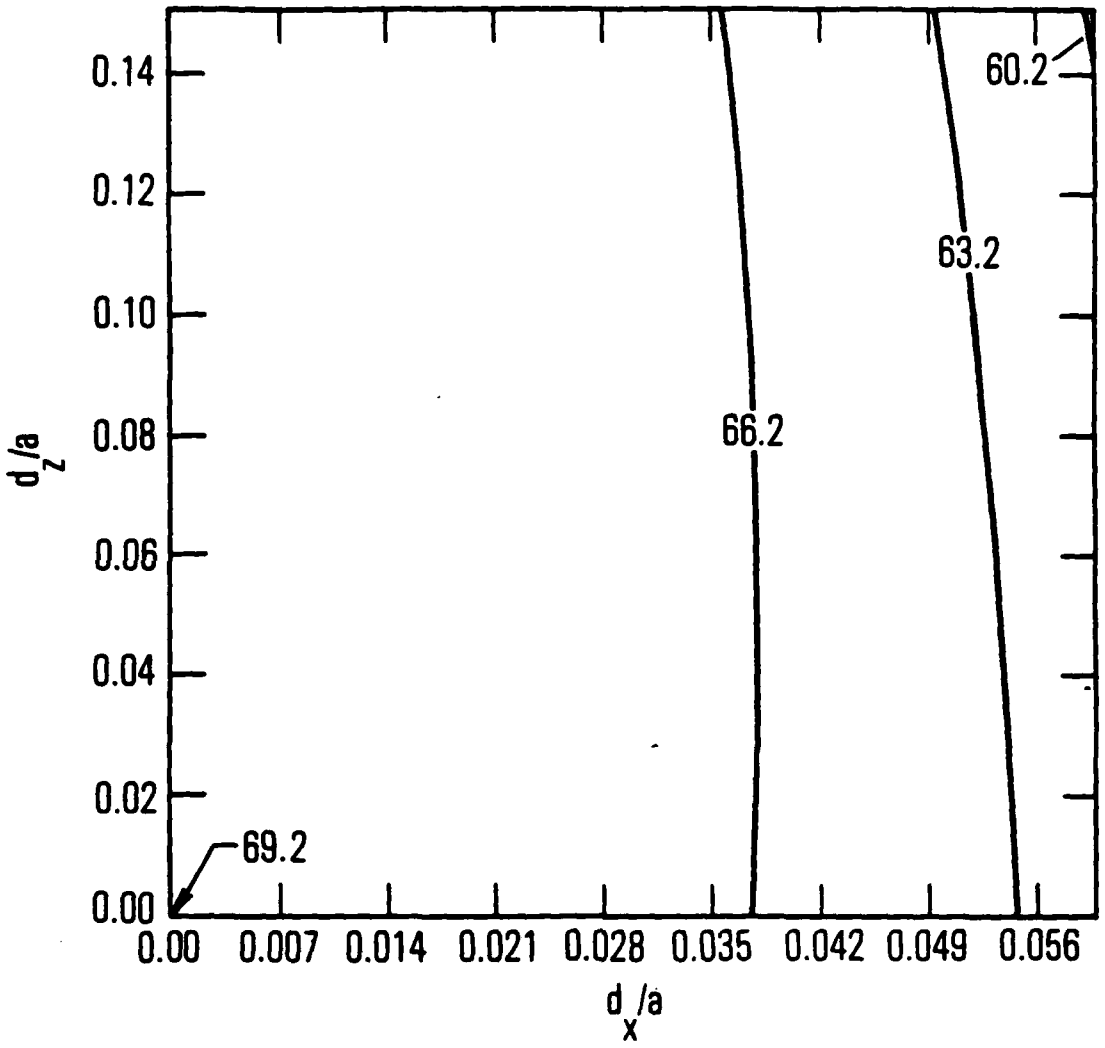

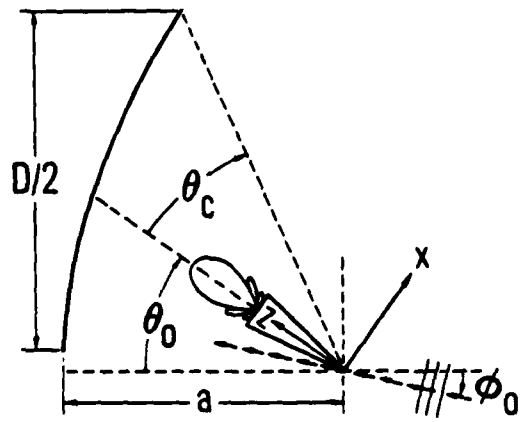

ka = 100
ϕ_0 = 0°
a/D = 0.6
θ_0 = 25.5°
θ_c = 22.357

Figure 36. Contour Plot of Total Field in Focal Region of Offset Paraboloid ka = 100, ϕ_o = 0°, a/D = 0.6, θ_o = 25.5°, θ_c = 22.357°

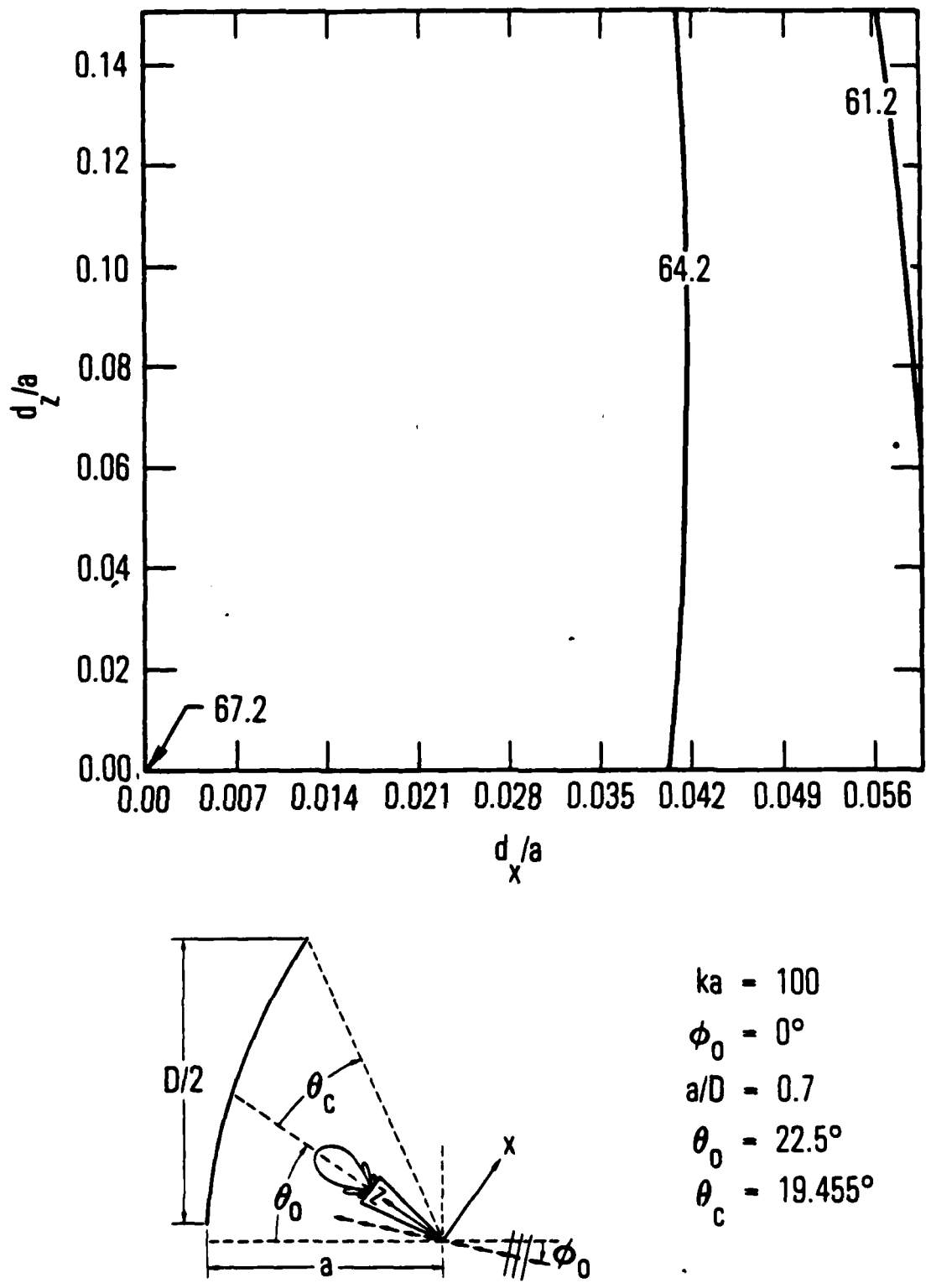

Figure 37. Contour Plot of Total Field in Focal Region of Offset Paraboloid ka = 100, ϕ_o = 0°, a/D = 0.7, θ_o = 22.5°, θ_c = 19.455°

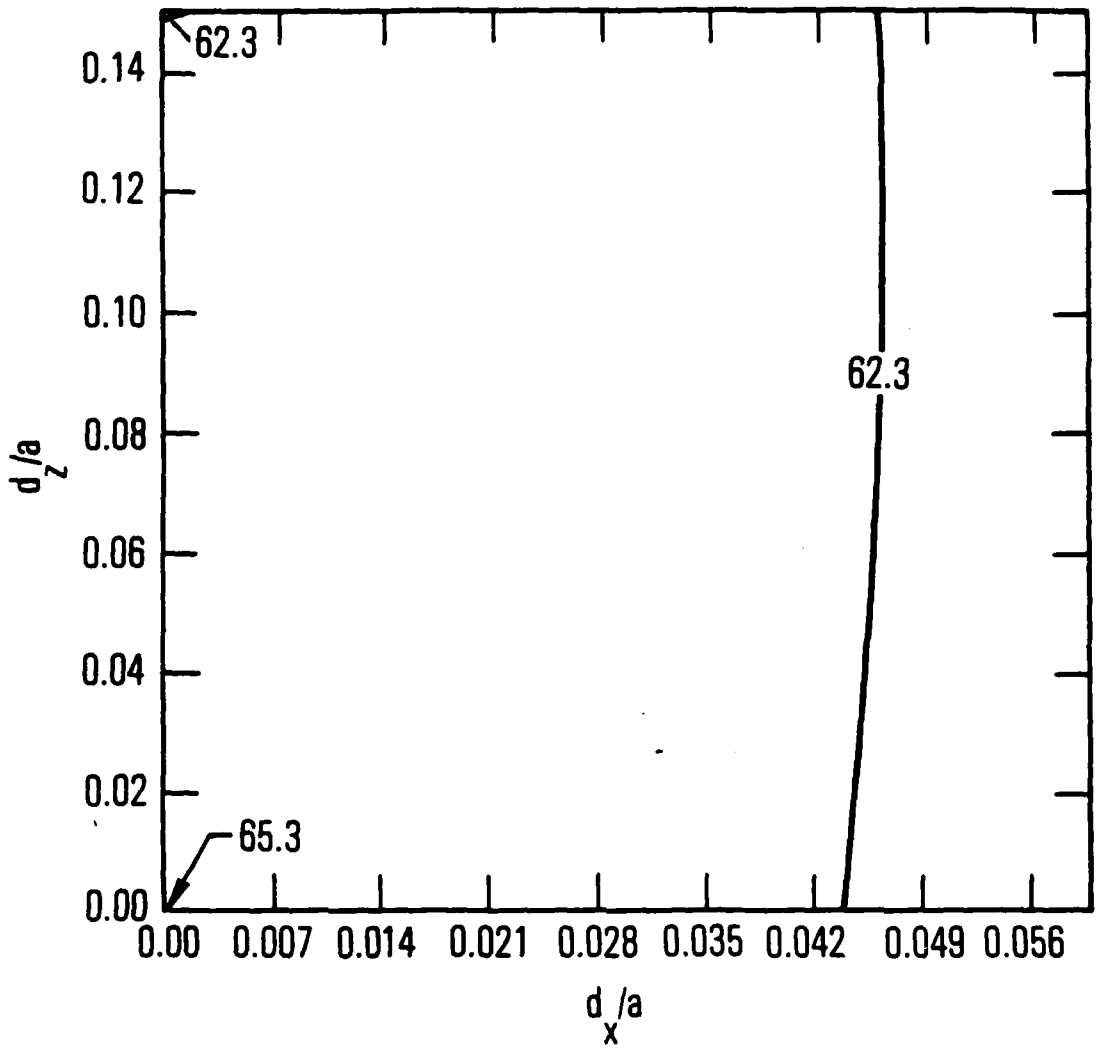

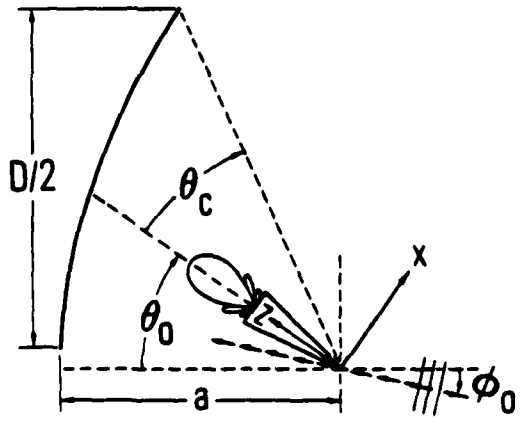

ka = 100
ϕ_0 = 0°
a/D = 0.8
θ_0 = 20.2°
θ_c = 17.197°

Figure 38. Contour Plot of Total Field in Focal Region of Offset Paraboloid ka = 100, ϕ_o = 0°, a/D = 0.8, θ_o = 20.2°, θ_c = 17.197°

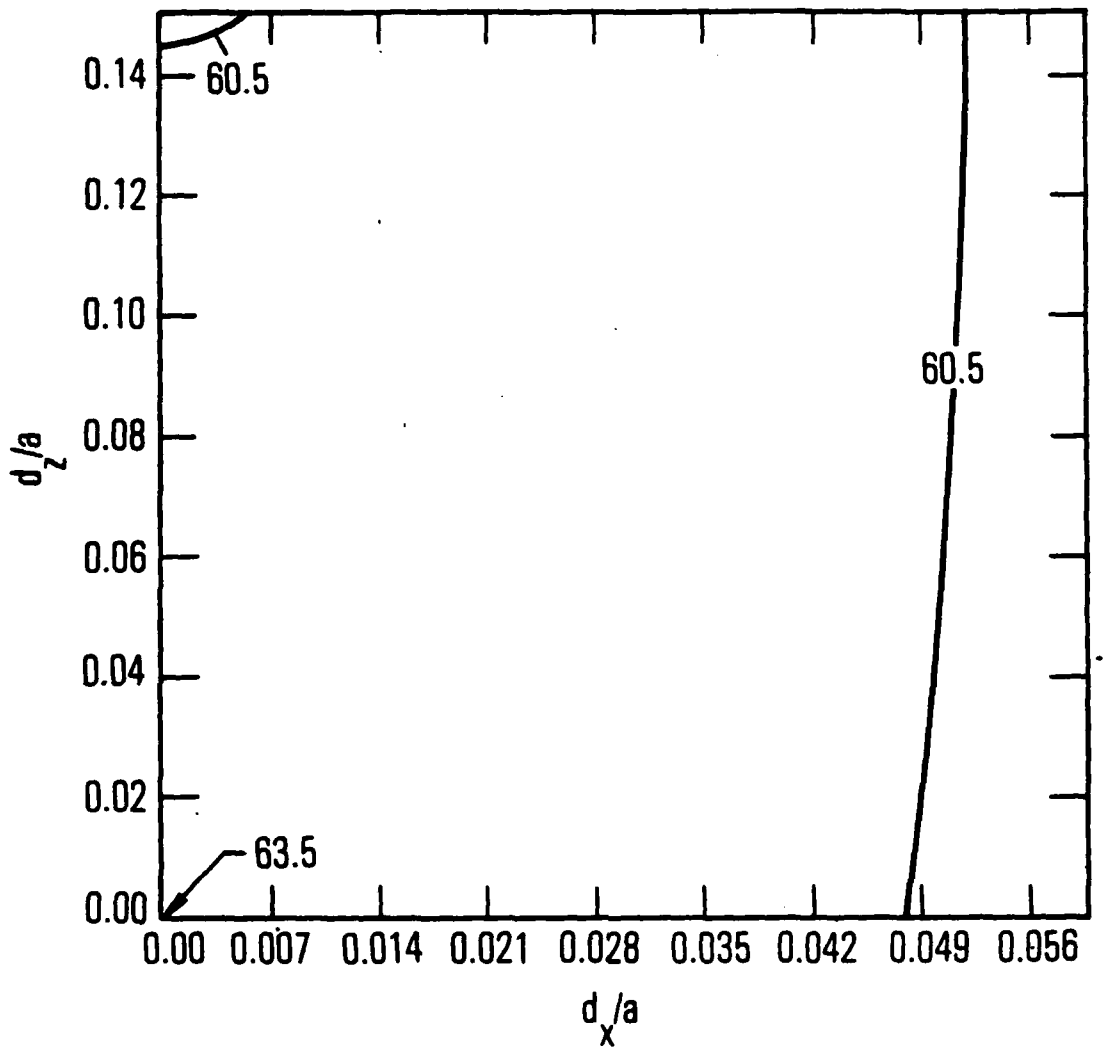

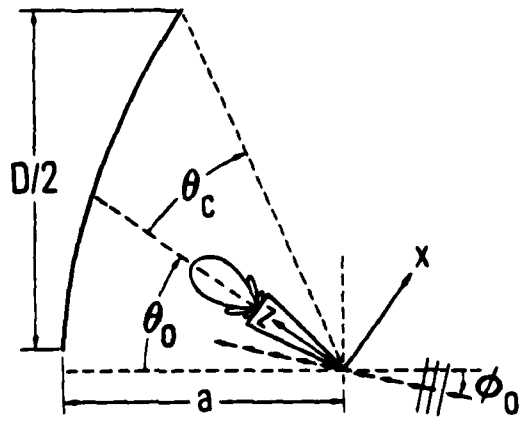

ka = 100
ϕ_0 = 0°
a/D = 0.9
θ_0 = 18.5°
θ_c = 15.389°

Figure 39. Contour Plot of Total Field in Focal Region of Offset Paraboloid ka = 100, ϕ_o = 0°, a/D = 0.9, θ_o = 18.5°, θ_c = 15.389°

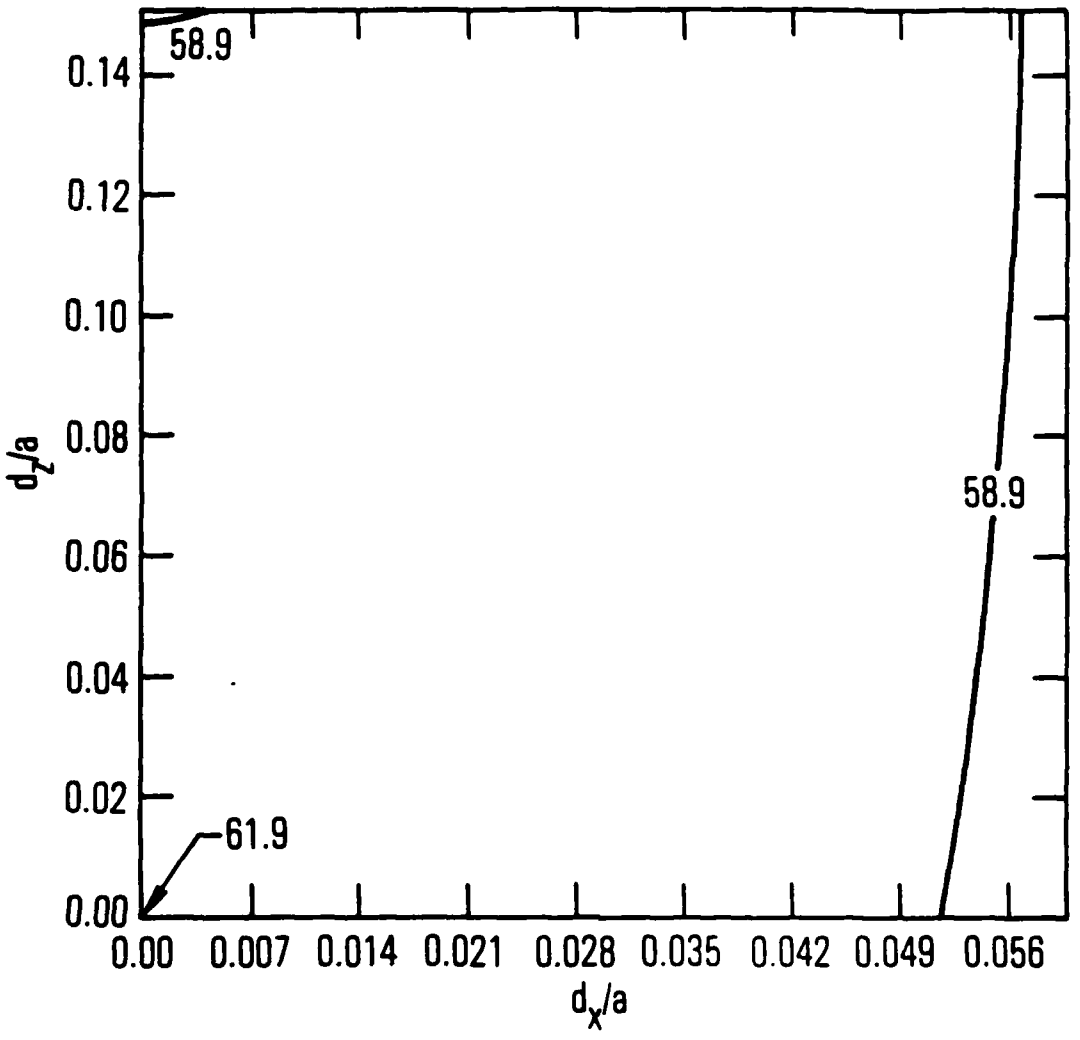

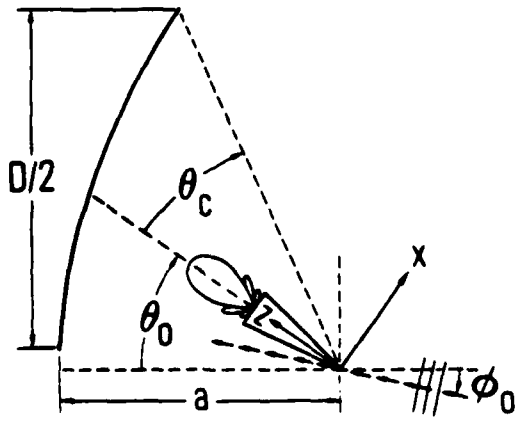

ka = 100
ϕ_0 = 0°
a/D = 1.0
θ_0 = 17°
θ_c = 13.924°

Figure 40. Contour Plot of Total Field in Focal Region of Offset Paraboloid ka = 100, ϕ_0 = 0°, a/D = 1.0, θ_0 = 17°, θ_c = 13.924°

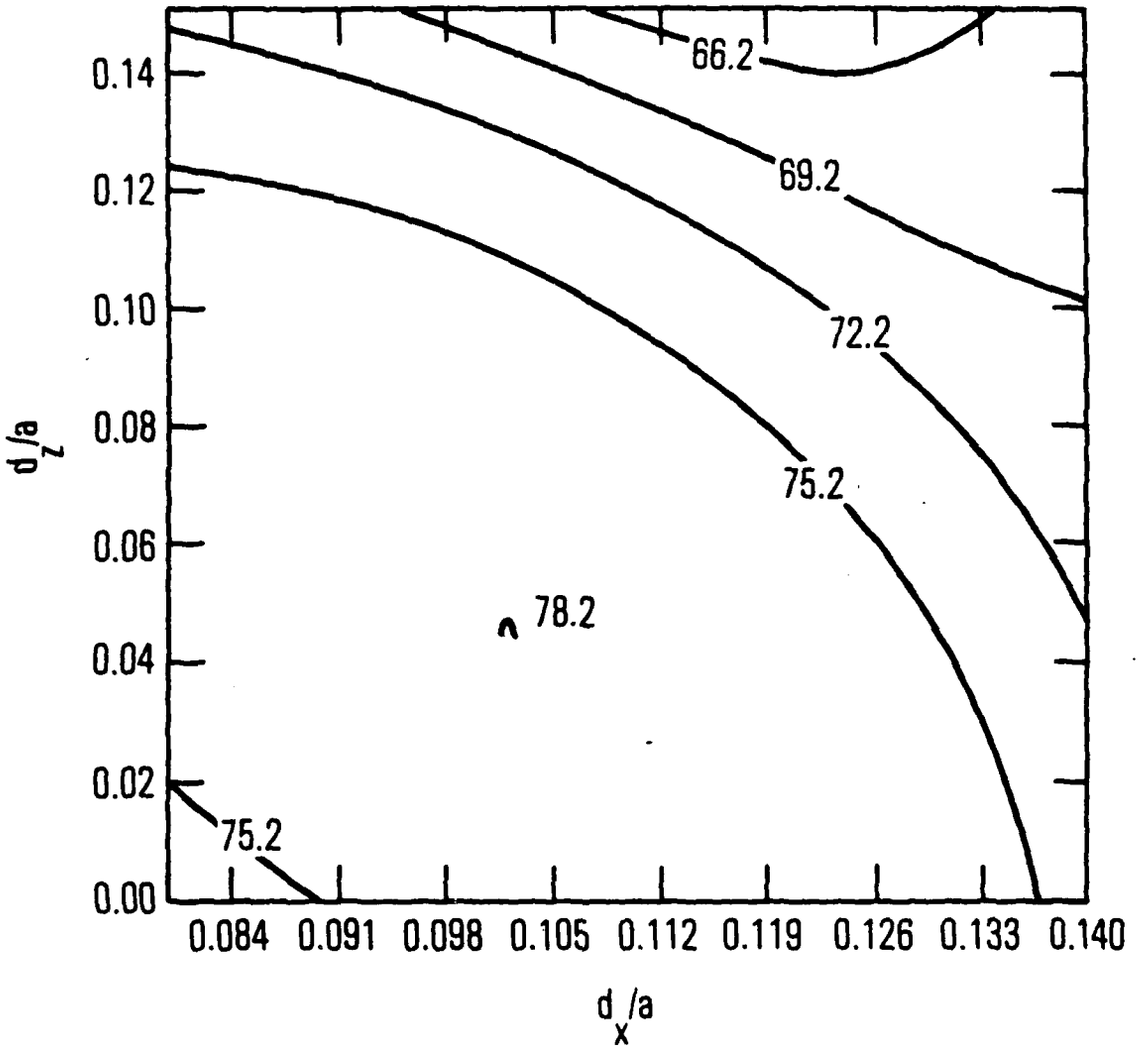

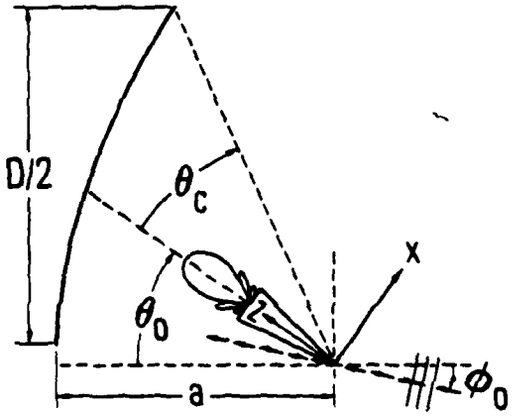

ka = 100
ϕ_0 = 5°
a/D = 0.2
θ_0 = 53°
θ_c = 50.587°

Figure 41. Contour Plot of Total Field in Focal Region of Offset Paraboloid ka = 100, ϕ_o = 5°, a/D = 0.2, θ_o = 53°, θ_c = 50.587°

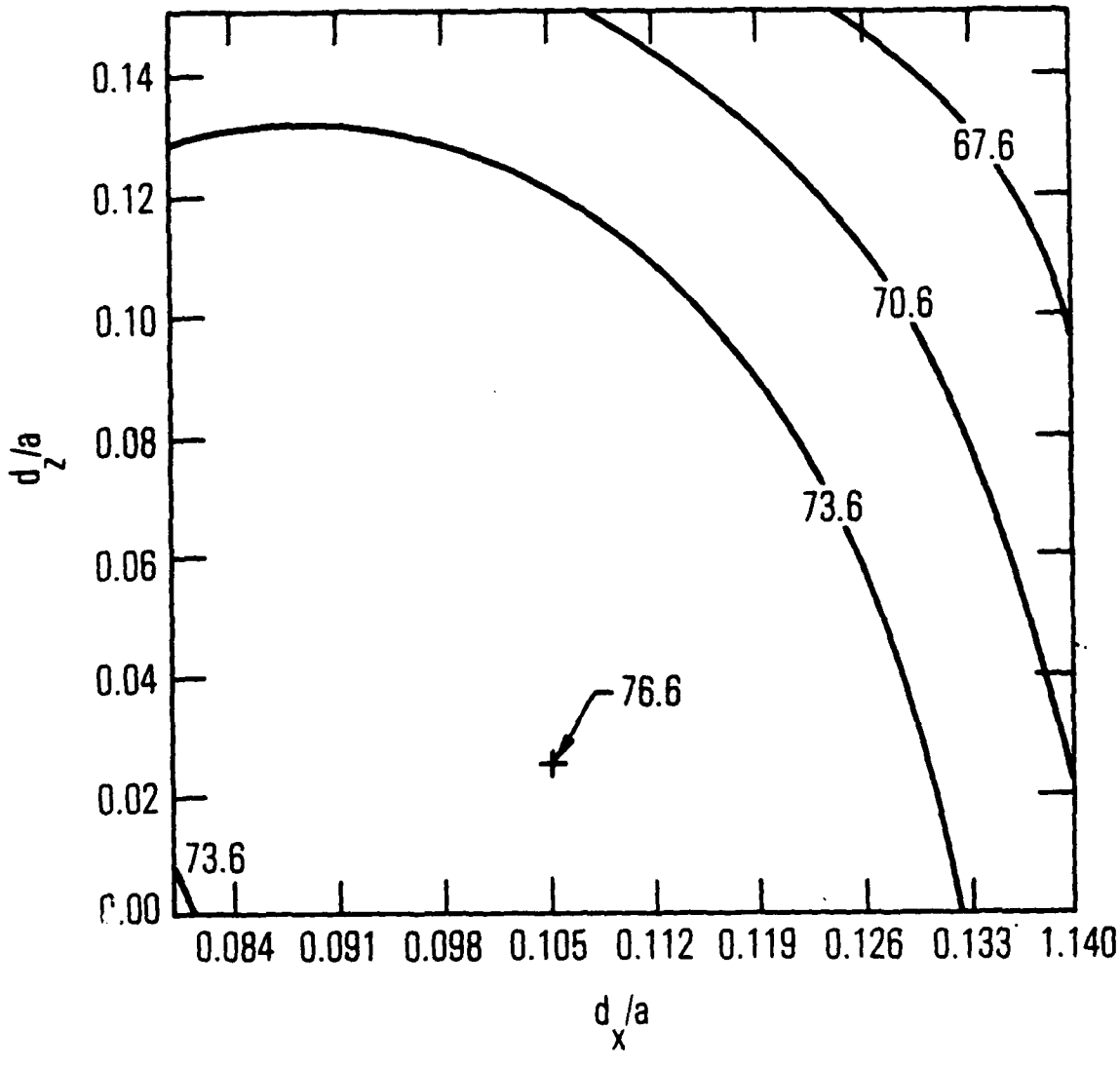

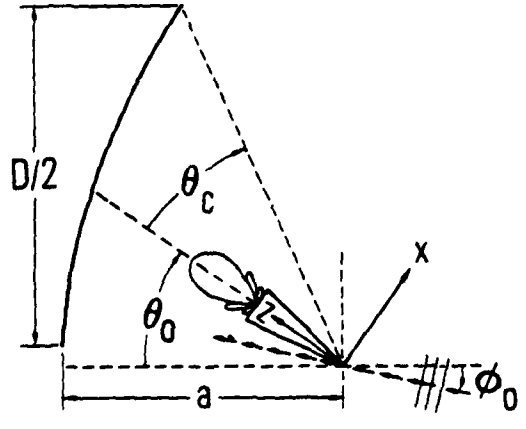

ka = 100
ϕ_0 = 5°
a/D = 0.3
θ_0 = 42
θ_c = 39.206

Figure 42. Contour Plot of Total Field in Focal Region of Offset Paraboloid ka = 100, ϕ_0 = 5°, a/D = 0.3, θ_0 = 42°, θ_c = 39.206°

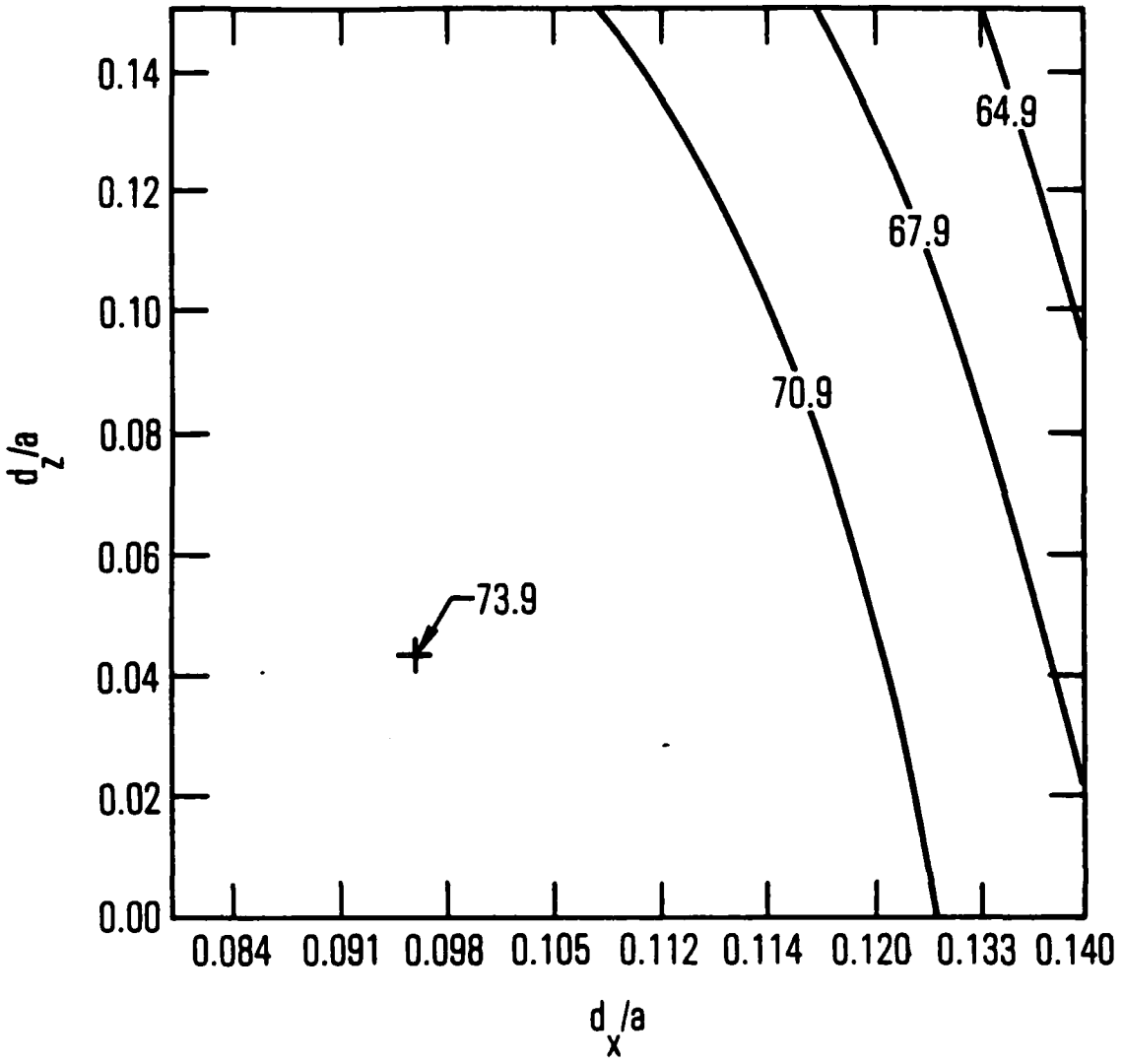

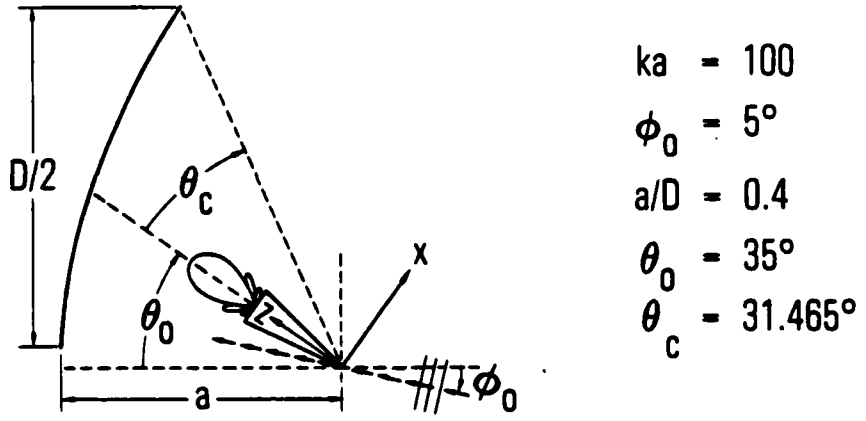

Figure 43. Contour Plot of Total Field in Focal Region of Offset Paraboloid ka = 100, ϕ_o = 5°, a/D = 0.4, θ_o = 35°, θ_c = 31.465°

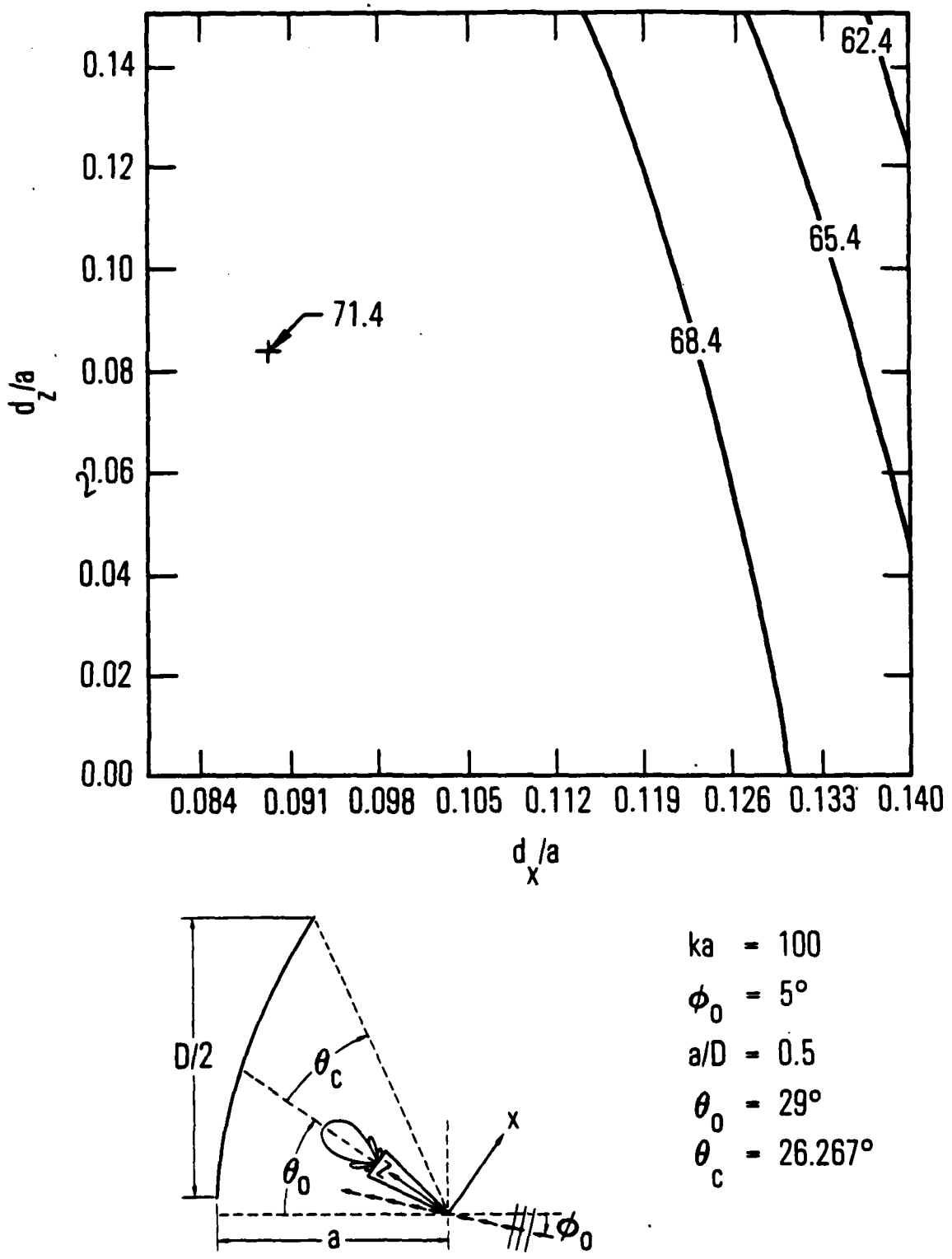

Figure 44. Contour Plot of Total Field in Focal Region of Offset Paraboloid ka = 100, ϕ_o = 5°, a/D = 0.5, θ_o = 29° θ_c = 26.267°

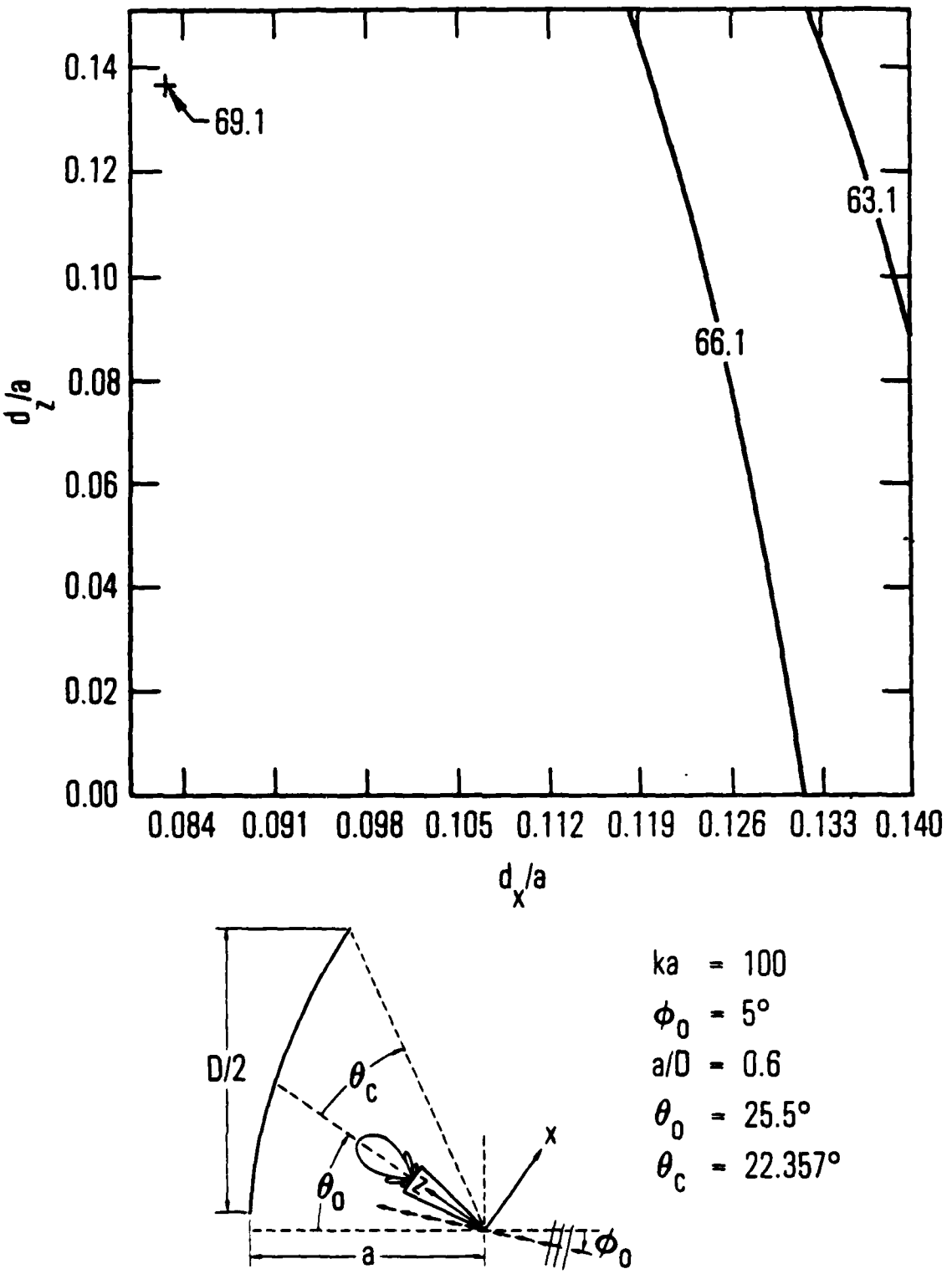

Figure 45. Contour Plot of Total Field in Focal Region of Offset Paraboloid ka = 100, a/D = 0.6, θ_o = 25.5°, θ_c = 22.357°

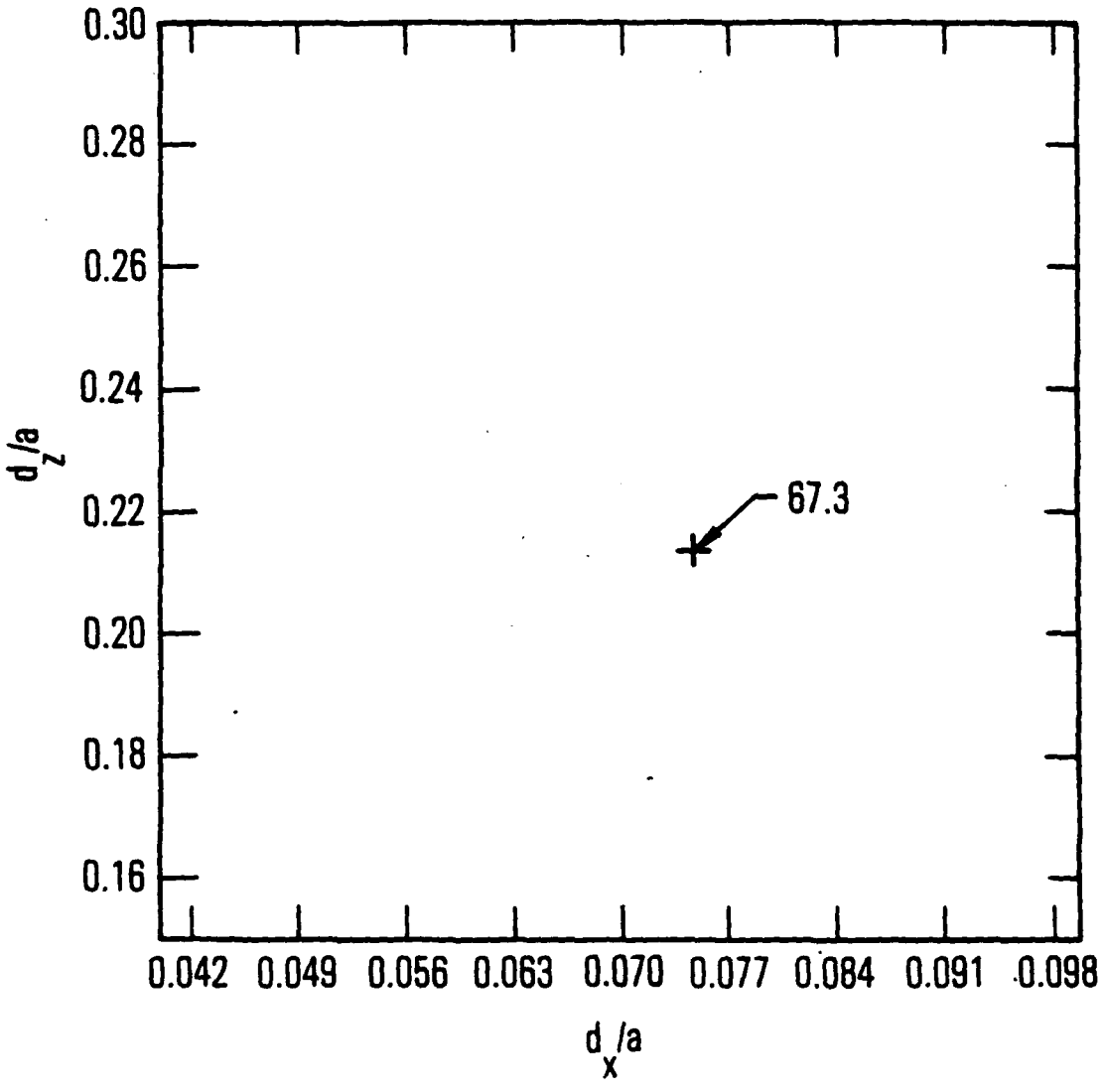

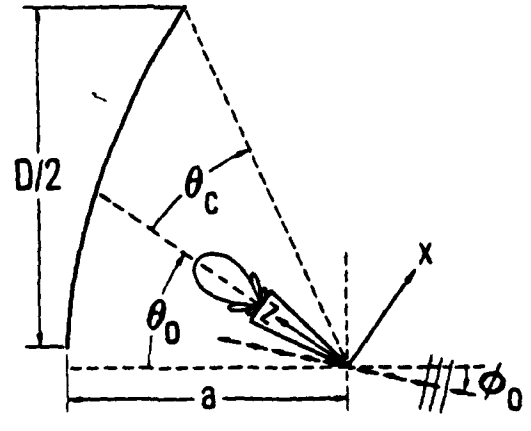

ka = 100
ϕ_0 = 5°
a/D = 0.7
θ_0 = 22.5
θ_c = 19.455

Figure 46. Contour Plot of Total Field in Focal Region of Offset Paraboloid ka = 100, ϕ_o = 5°, a/D = 0.7, θ_o = 22.5°, θ_c = 19.455°

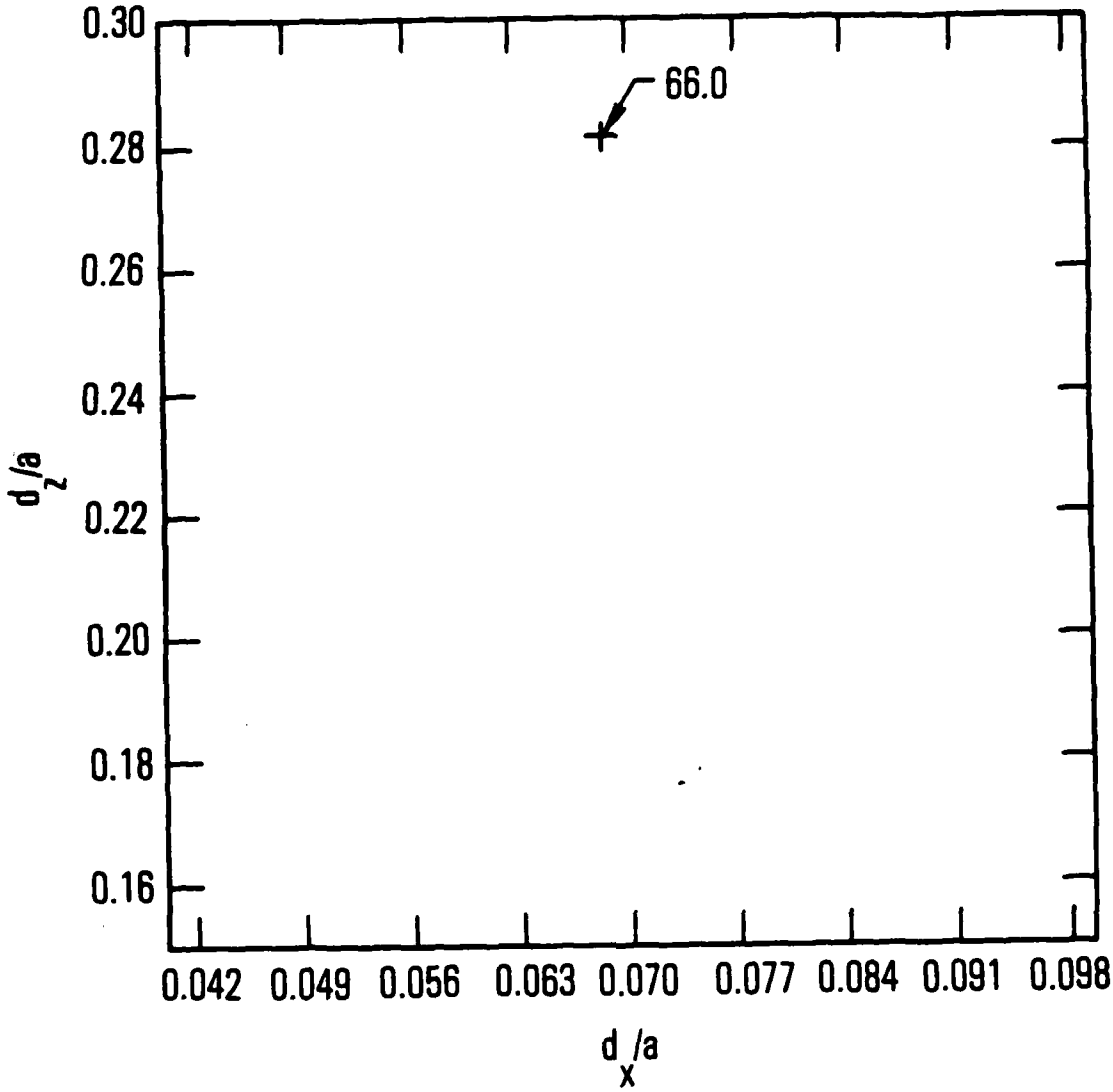

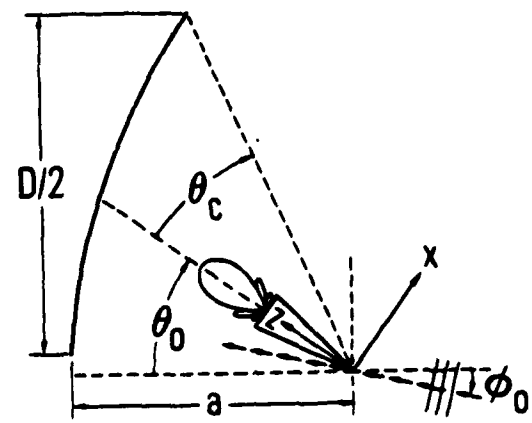

ka = 100
ϕ_0 = 5°
a/D = 0.8
θ_0 = 20.2
θ_c = 17.197

Figure 47. Contour Plot of Total Field in Focal Region of Offset Paraboloid ka = 100, ϕ_0 = 5°, a/D = 0.8, θ_0 = 20.2, θ_c = 17.197°

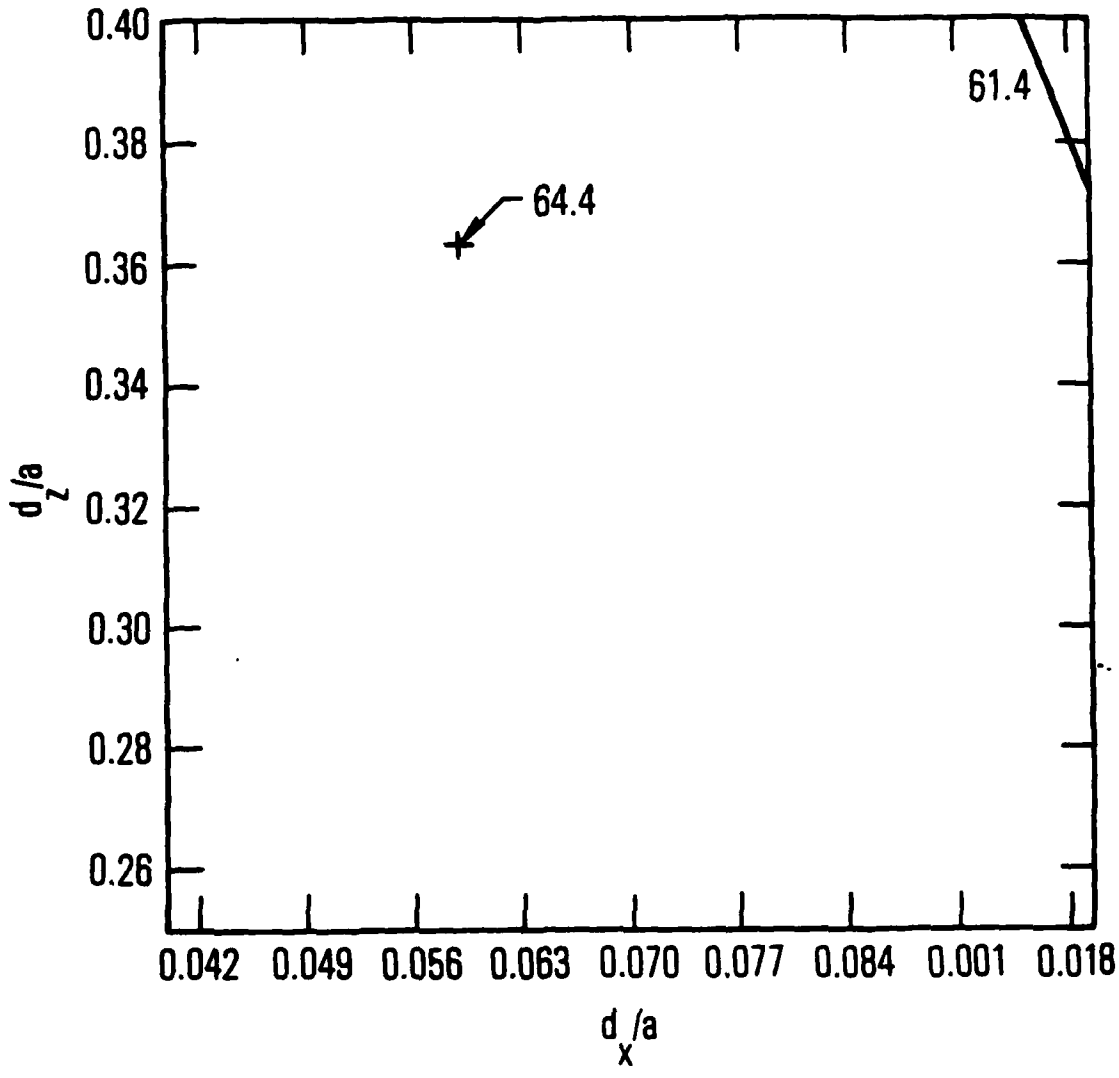

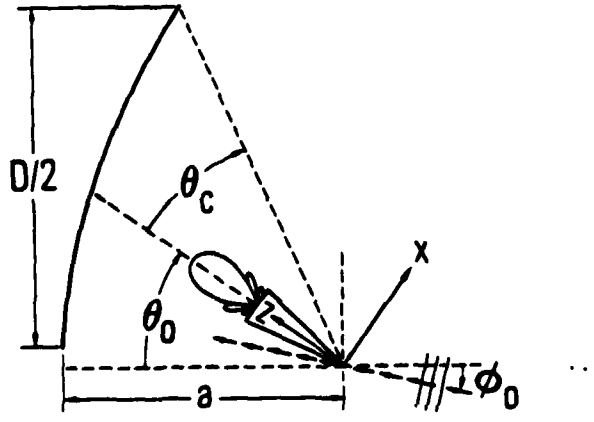

ka = 100
ϕ_0 = 5°
a/D = 0.9
θ_0 = 18.5
θ_c = 15.389°

Figure 48. Contour Plot of Total Field in Focal Region of Offset Paraboloid ka = 100, ϕ_o = 5°, a/D = 0.9, θ_o = 18.5°, θ_c = 15.389°

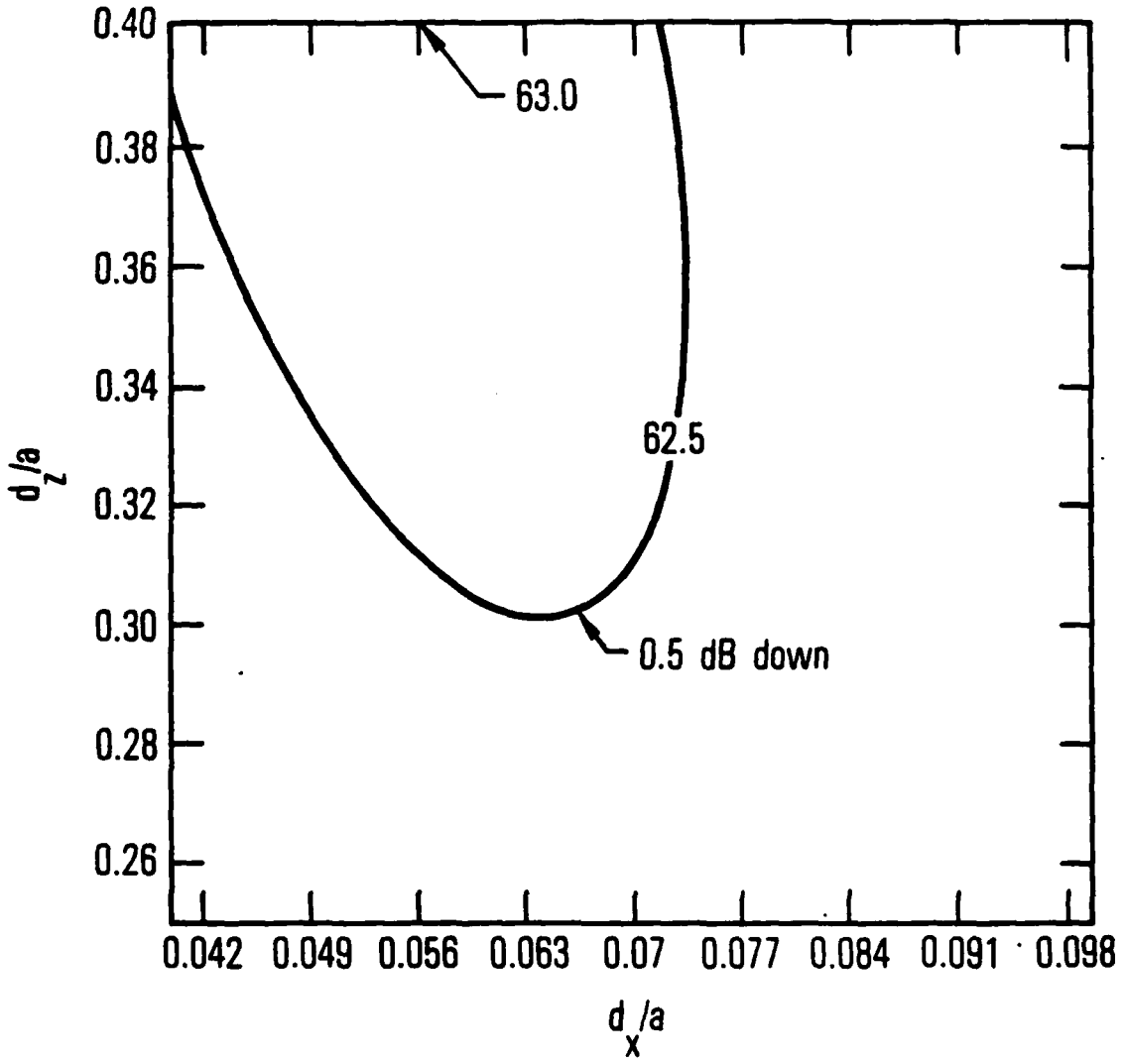

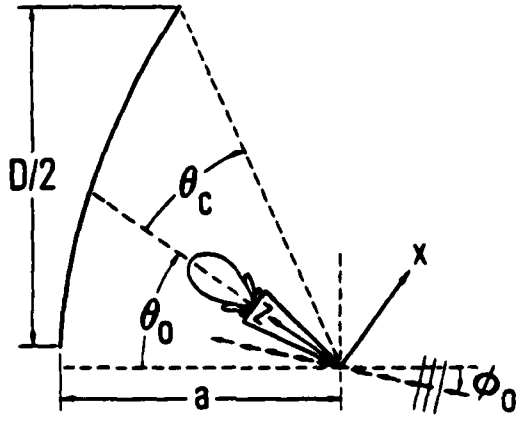

ka = 100
ϕ_0 = 5°
a/D = 1.0
θ_0 = 17°
θ_c = 13.924

Figure 49. Contour Plot of Total Field in Focal Region of Offset Paraboloid ka = 100, ϕ_o = 5°, a/D = 1.0, θ_o = 17°, θ_c = 13.924°

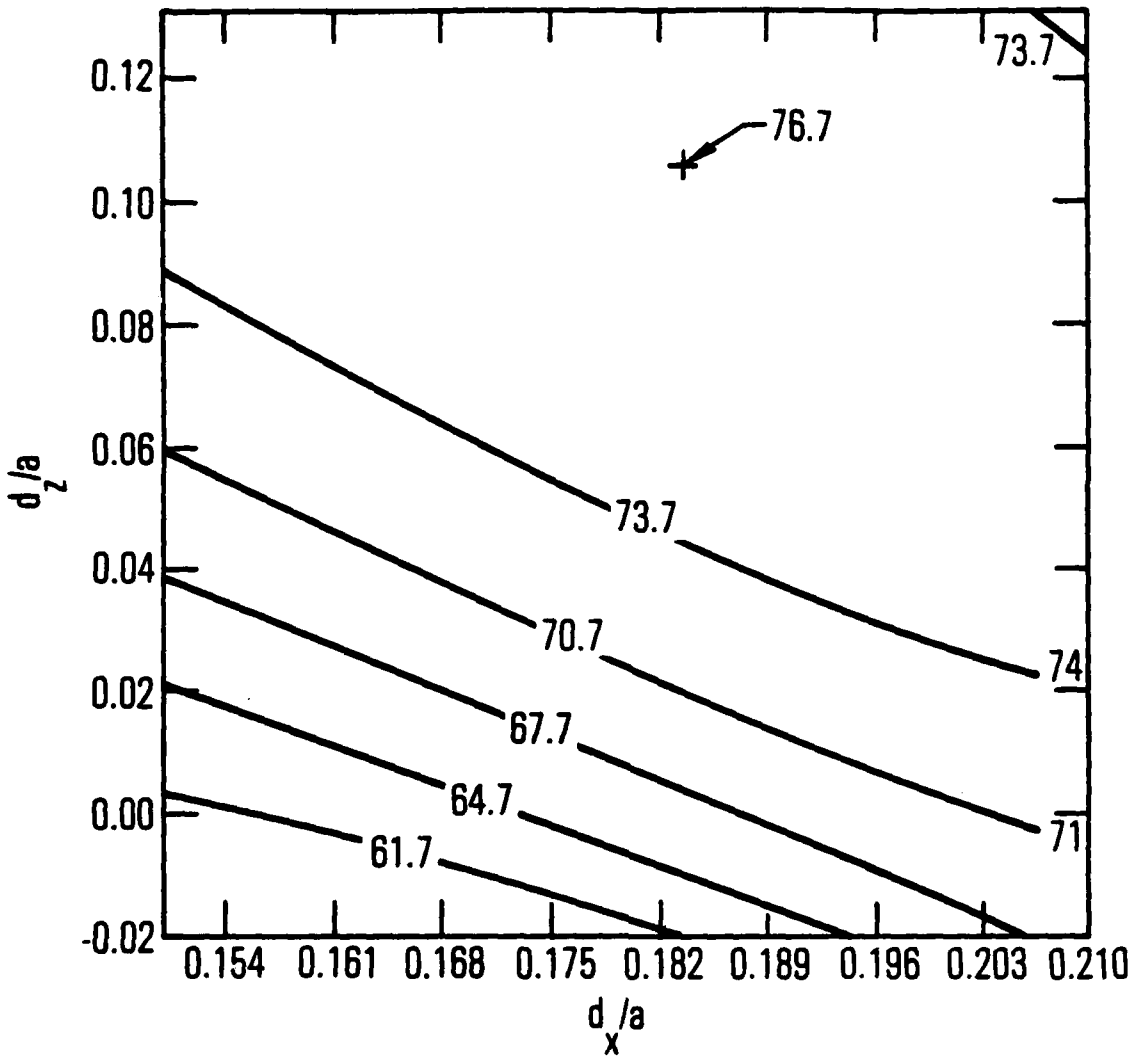

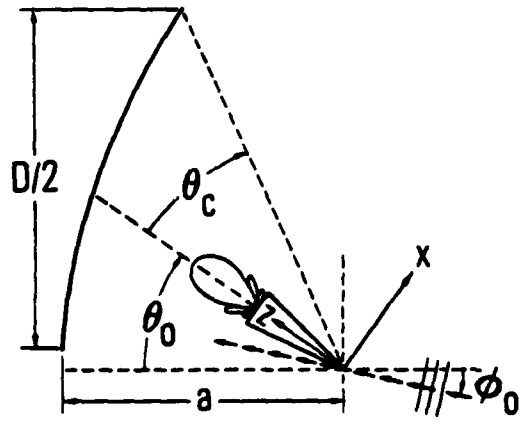

ka = 100

ϕ_0 = 10°

a/D = 0.2

θ_0 = 53°

θ_c = 50.587

Figure 50. Contour Plot of Total Field in Focal Region of Offset Paraboloid ka = 100, ϕ_o = 10°, a/D = 0.2, θ_o = 53°, θ_c = 50.587°

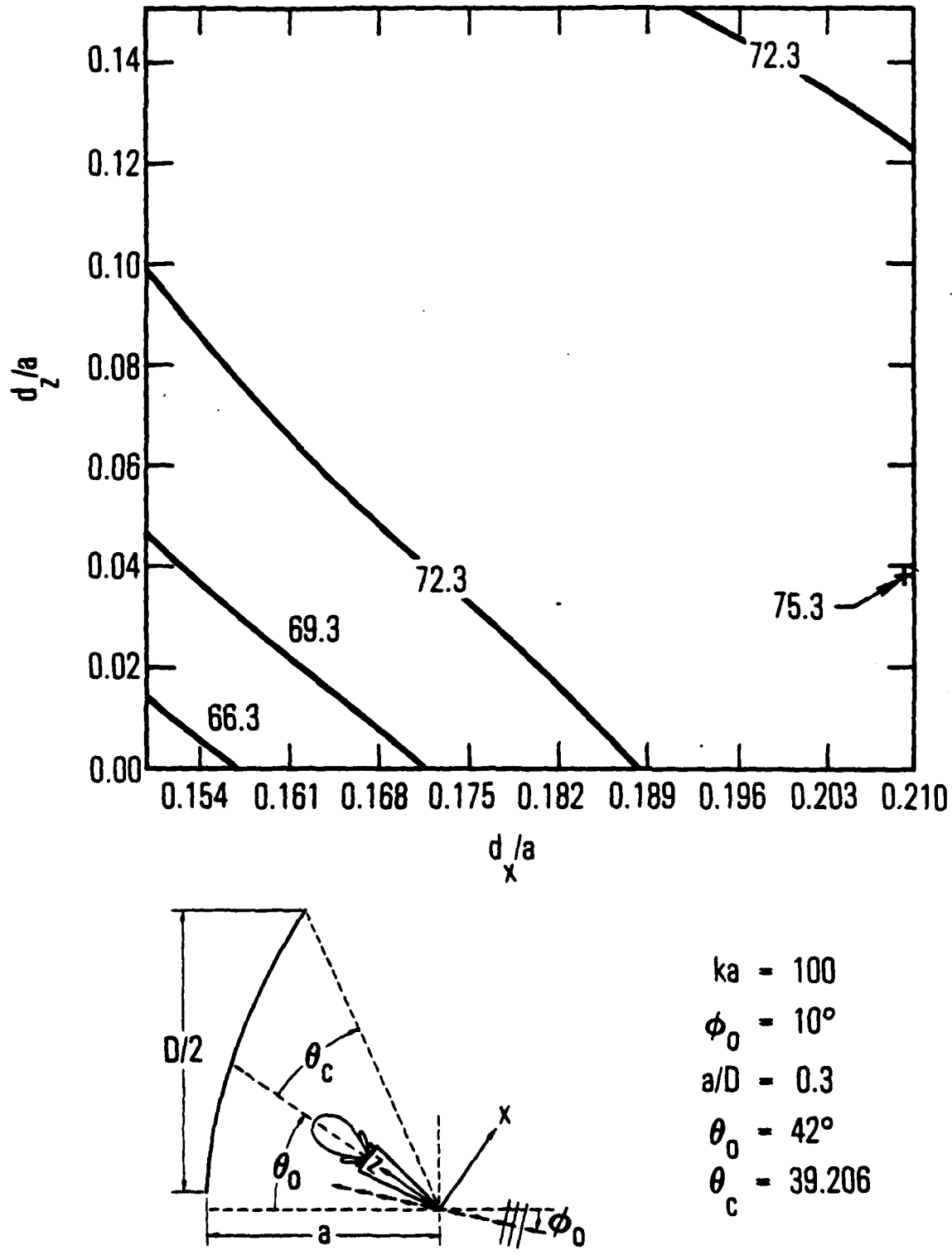

Figure 51. Contour Plot of Total Field in Focal Region of Offset Paraboloid ka = 100, ϕ_o = 10°, a/D = 0.3, θ_o = 42°, θ_c = 39.206°

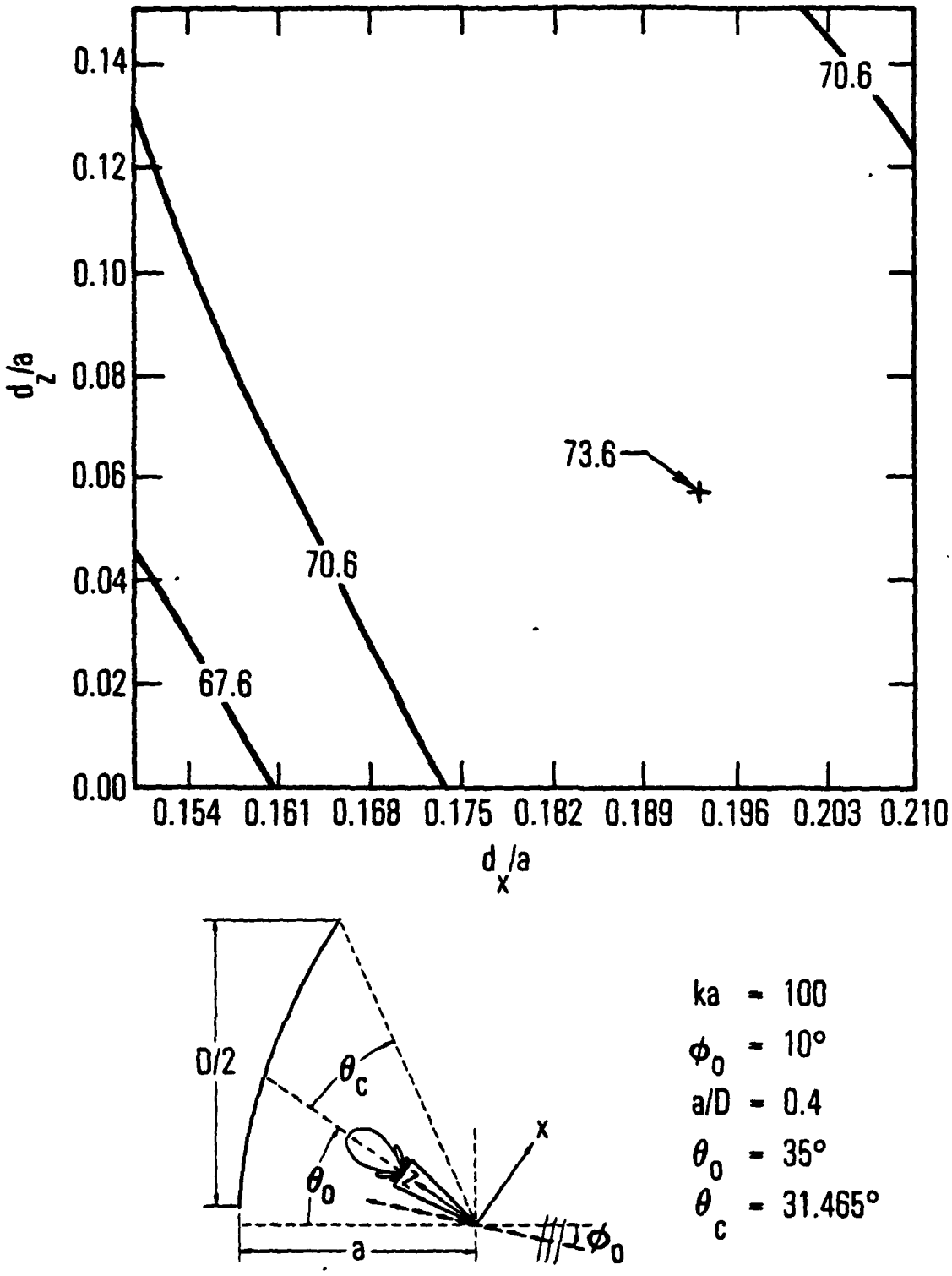

Figure 52. Contour Plot of Total Field in Focal Region of Offset Paraboloid ka = 100, ϕ_o = 10°, a/D = 0.4, θ_o = 35°, θ_c = 31.465°

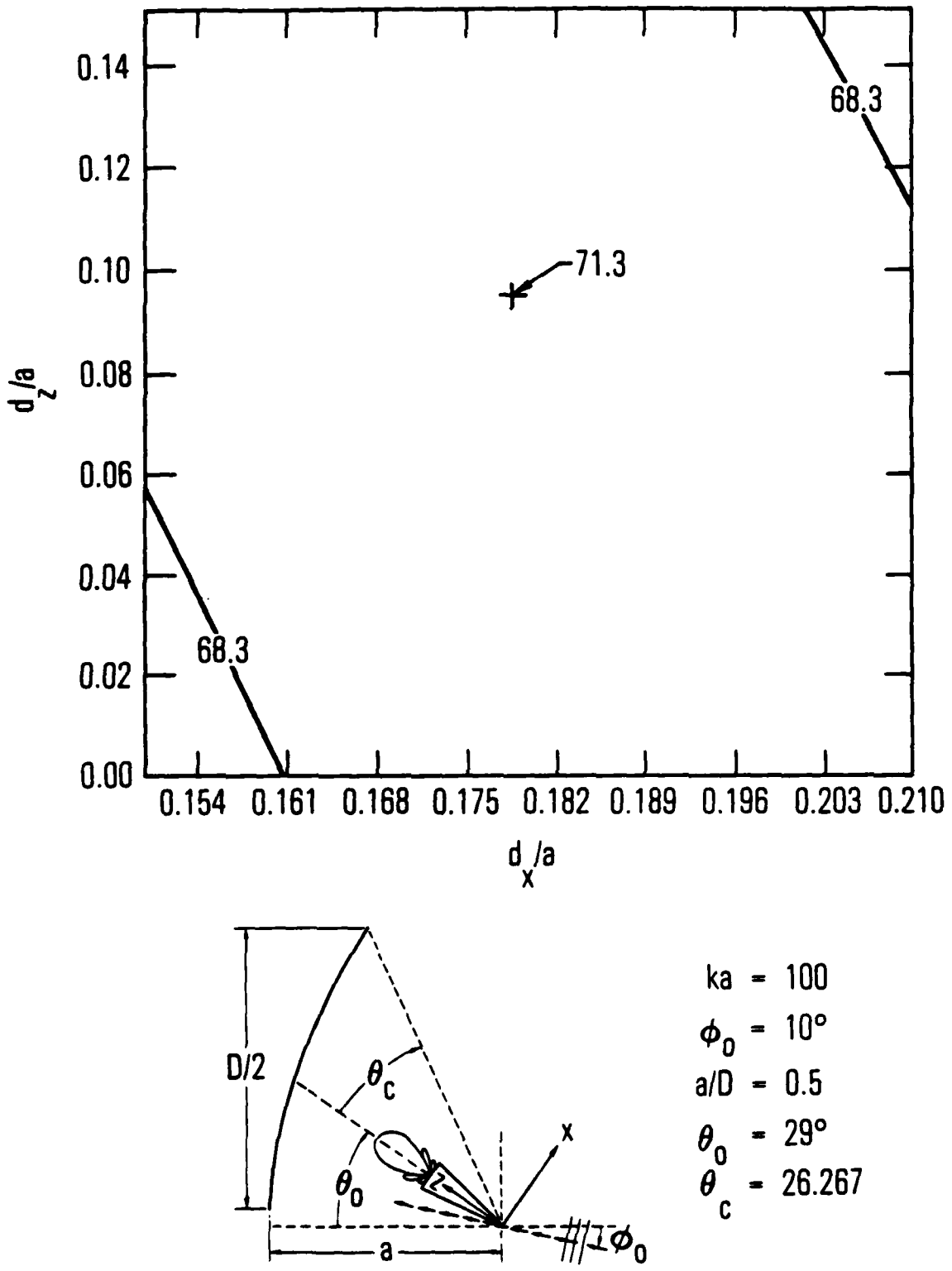

Figure 53. Contour Plot of Total Field in Focal Region of Offset Paraboloid ka = 100, ϕ_o = 10°, a/D = 0.5, θ_o = 29°, θ_c = 26.267°

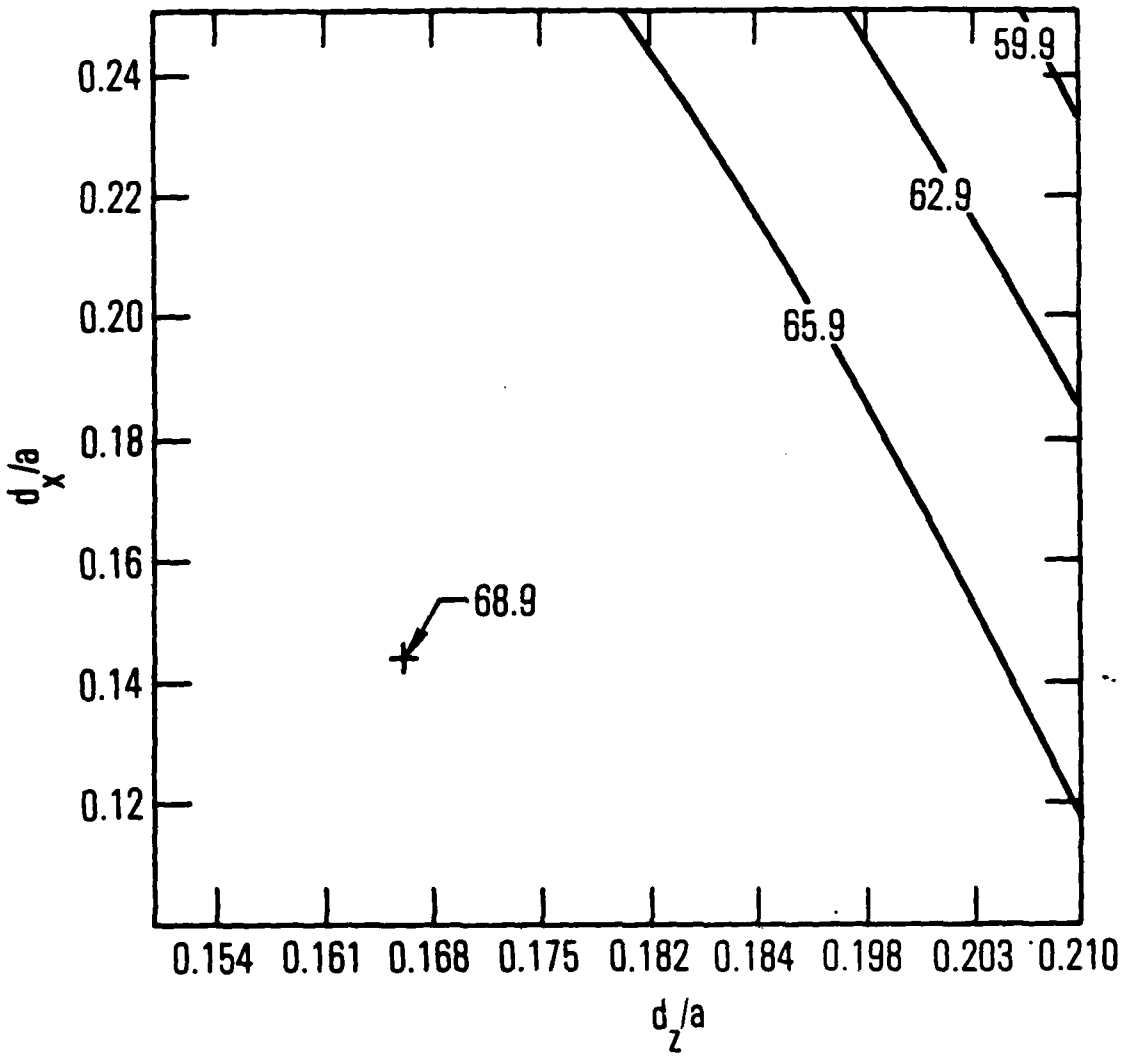

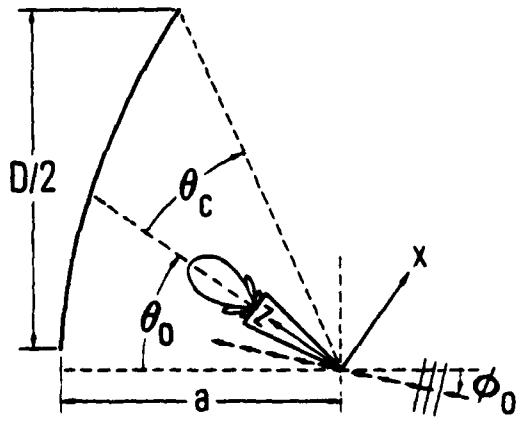

ka = 100
ϕ_0 = 10°
a/D = 0.6
θ_0 = 25.5
θ_c = 22.357°

Figure 54. Contour Plot of Total Field in Focal Region of Offset Paraboloid ka = 100, ϕ_o = 10°, a/D = 0.6, θ_o = 25.5°, θ_c = 22.357°

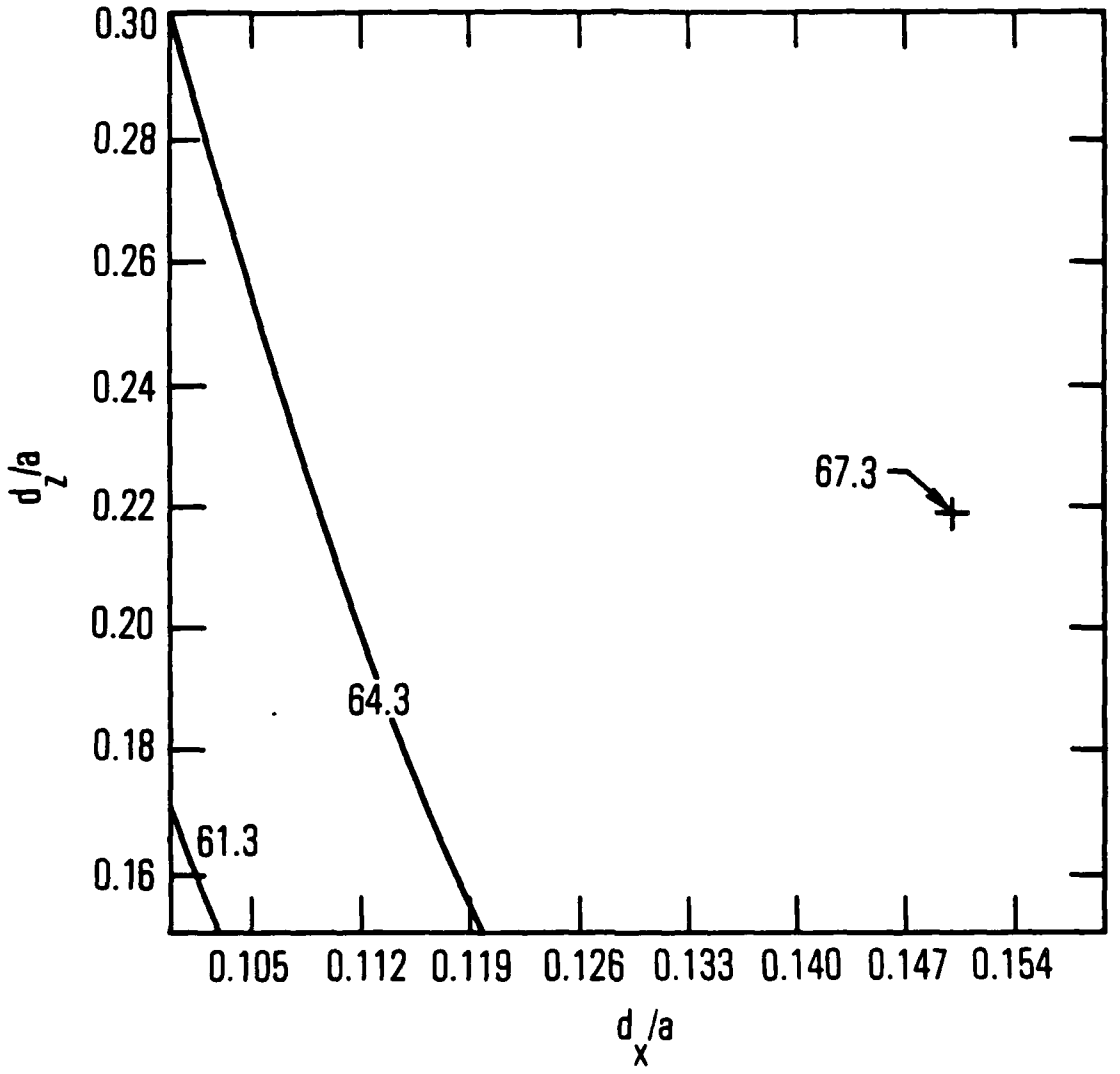

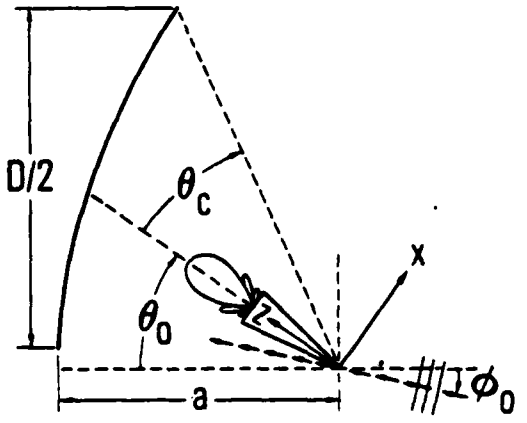

ka = 100
ϕ_0 = 10°
a/D = 0.7
θ_0 = 22.5
θ_c = 19.455

Figure 55. Contour Plot of Total Field in Focal Region of Offset Paraboloid ka = 100, ϕ_o = 10°, a/D = 0.7, θ_o = 22.5°, θ_c = 19.455°

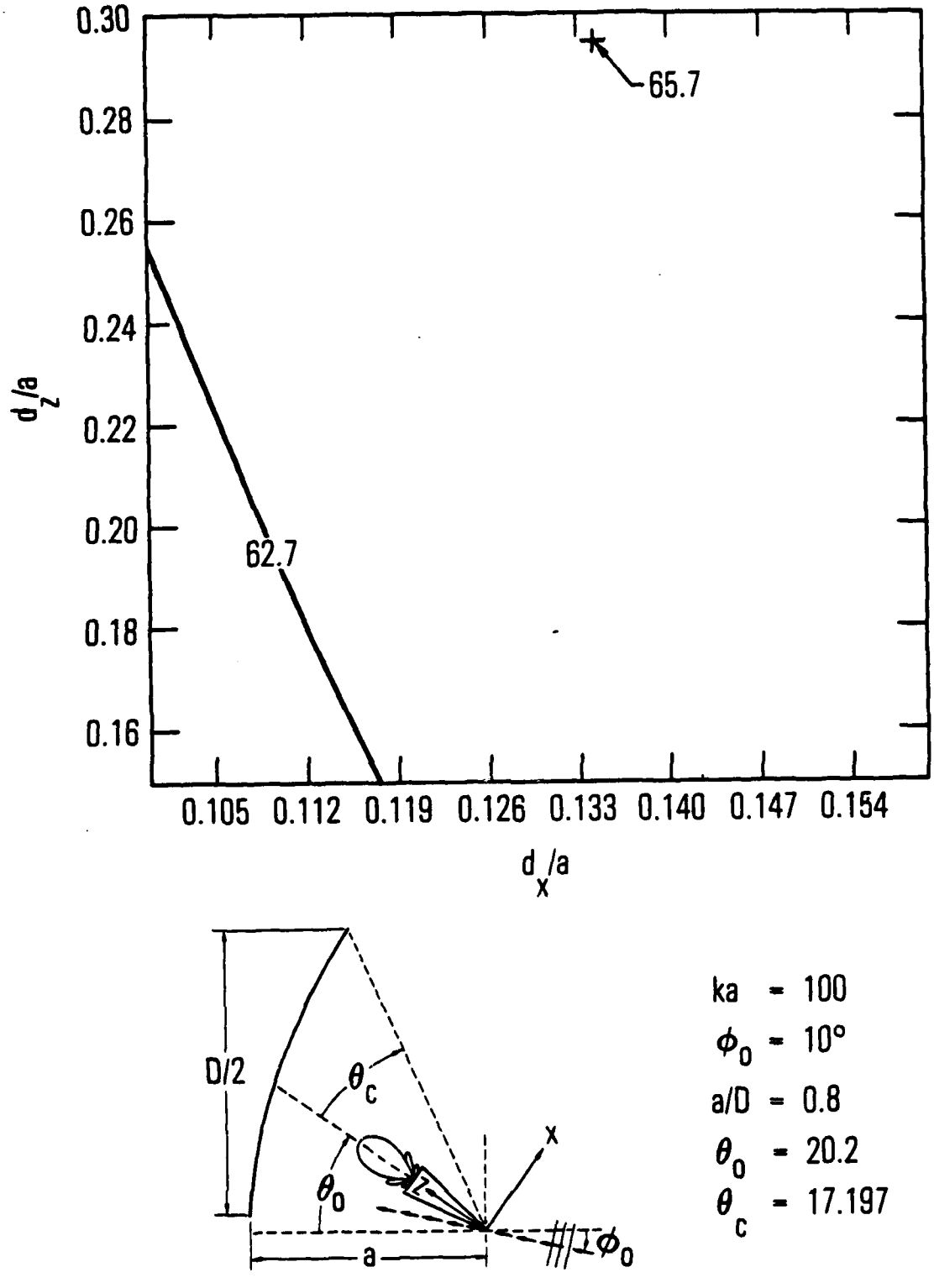

Figure 56. Contour Plot of Total Field in Focal Region of Offset Paraboloid ka = 100, ϕ_o = 10°, a/D = 0.8, θ_o = 20.2°, θ_c = 17.197°

IV. SUMMARY

A study of the focal region field structures of circular and offset reflectors has been made. These results are based on a surface current formulation, and the analysis was derived in exact form to the order of physical optics. Numerical results were obtained for a wide range of a/D values for on-axis and off-axis illumination; the values selected span the conditions for both significant and minimal scan degradation. The results are presented in terms of field contours in the focal region, and the sensitivity of focusing can be judged through the variations in contours. The results of these analyses are compared with previously published results where possible; the agreement with other work is very good. The end result of this effort is an analysis code which can be used for a variety of applications.

V. REFERENCES

1. P. G. Ingerson and W. V. T. Rusch, "Radiation from a Paraboloid with an Axially Defocused Feed," IEEE Trans. Ant. and Prop., Vol. AP-21, pp. 104-106, January 1973, Fig. 4.

2. J. R. Cogdell and J. H. Davis, "Astigmatism in Reflector Antennas," IEEE Trans. on Ant. and Prop., Vol. AP-21, pp. 564-567, July 1973.

3. J. Ruze, "Lateral Feed Displacement in a Parabola," IEEE Trans. on Ant. and Prop., Vol. AP-13, pp. 660-665, Sept. 1965.

4. T. S. Chu, "A Note on Simulating Fraunhofer Radiation Patterns in the Fresnel Region," IEEE Trans. on Ant. and Prop., Vol. AP-19, pp. 691-692, September 1961.

5. D. K. Chang, "On the Simulation of Fraunhofer Radiation Patterns in the Fresnel Region," IRE Trans. on Ant. and Prop., Vol. AP-5, pp. 394-402, October 1957.

6. W. A. Imbriale, P. G. Ingerson, and W. C. Wong, "Large Lateral Displacements in a Paraboloid Reflector," IEEE Trans. on Ant. and Prop., Vol. AP-22, pp. 642-745, November 1974.

7. W. V. T. Rusch and A. C. Ludwig, "Determination of the Maximum Scan-Gain Contours of a Beam-Scanning Paraboloid and their Relation to the Petzval Surface," IEEE Trans. on Ant. and Prop., Vol. AP-21, pp. 141-147, March 1973.

8. E. M. Kennaugh and R. H. Ott, "Fields in the Focal Region of a Parabolic Receiving Antenna," IEEE Trans. on Ant. and Prop., Vol. AP-12, No. 3, pp. 376-377, May 1964.

9. Y. T. Lo, "On the Beam Deviation Factor of a Parabolic Reflector," IRE Trans. on Ant. and Prop., Vol. AP-8, pp. 347-349, May 1960.

10. T. S. Chu and R. H. Turin, "Depolarization Properties of Offset Reflector Antennas," IEEE Trans. on Ant. and Prop., Vol. AP-21, pp. 339-345, May 1973.

LABORATORY OPERATIONS

The Aerospace Corporation functions as an "architect-engineer" for national security projects, specializing in advanced military space systems. Providing research support, the corporation's Laboratory Operations conducts experimental and theoretical investigations that focus on the application of scientific and technical advances to such systems. Vital to the success of these investigations is the technical staff's wide-ranging expertise and its ability to stay current with new developments. This expertise is enhanced by a research program aimed at dealing with the many problems associated with rapidly evolving space systems. Contributing their capabilities to the research effort are these individual laboratories:

Aerophysics Laboratory: Launch vehicle and reentry fluid mechanics, heat transfer and flight dynamics; chemical and electric propulsion, propellant chemistry, chemical dynamics, environmental chemistry, trace detection; spacecraft structural mechanics, contamination, thermal and structural control; high temperature thermomechanics, gas kinetics and radiation; cw and pulsed chemical and excimer laser development including chemical kinetics, spectroscopy, optical resonators, beam control, atmospheric propagation, laser effects and countermeasures.

Chemistry and Physics Laboratory: Atmospheric chemical reactions, atmospheric optics, light scattering, state-specific chemical reactions and radiative signatures of missile plumes, sensor out-of-field-of-view rejection, applied laser spectroscopy, laser chemistry, laser optoelectronics, solar cell physics, battery electrochemistry, space vacuum and radiation effects on materials, lubrication and surface phenomena, thermionic emission, photosensitive materials and detectors, atomic frequency standards, and environmental chemistry.

Computer Science Laboratory: Program verification, program translation, performance-sensitive system design, distributed architectures for spaceborne computers, fault-tolerant computer systems, artificial intelligence, microelectronics applications, communication protocols, and computer security.

Electronics Research Laboratory: Microelectronics, solid-state device physics, compound semiconductors, radiation hardening; electro-optics, quantum electronics, solid-state lasers, optical propagation and communications; microwave semiconductor devices, microwave/millimeter wave measurements, diagnostics and radiometry, microwave/millimeter wave thermionic devices; atomic time and frequency standards; antennas, rf systems, electromagnetic propagation phenomena, space communication systems.

Materials Sciences Laboratory: Development of new materials: metals, alloys, ceramics, polymers and their composites, and new forms of carbon; nondestructive evaluation, component failure analysis and reliability; fracture mechanics and stress corrosion; analysis and evaluation of materials at cryogenic and elevated temperatures as well as in space and enemy-induced environments.

Space Sciences Laboratory: Magnetospheric, auroral and cosmic ray physics, wave-particle interactions, magnetospheric plasma waves; atmospheric and ionospheric physics, density and composition of the upper atmosphere, remote sensing using atmospheric radiation; solar physics, infrared astronomy, infrared signature analysis; effects of solar activity, magnetic storms and nuclear explosions on the earth's atmosphere, ionosphere and magnetosphere; effects of electromagnetic and particulate radiations on space systems; space instrumentation.

...

END

DTIC

6-86